DEVELOPMENT OF NOVEL DEVICE TECHNOLOGIES FOR SAFER MRI GUIDED BIOPSY PROCEDURES

by

Doğangün Uzun

B.S., in Electrical and Electronics Engineering, Boğaziçi University, 2016

Submitted to the Institute of Biomedical Engineering
in partial fulfillment of the requirements
for the degree of
Doctor
of
Philosophy

Boğaziçi University
2023

ACKNOWLEDGMENTS

As I come to the completion of this significant milestone in my academic journey I am filled with profound gratitude. This thesis would be impossible to complete without the unwavering encouragement of my family and friends who stood by my side through every challenge and celebrated every achievement with me.

I must express my thanks to my outstanding thesis advisor, Assoc. Prof. Dr. Özgür Kocatürk, for his invaluable instructions and teachings. His expertise, patience, and willingness to invest time and effort in shaping my research have been instrumental in making this thesis a comprehensive and insightful work. His constant encouragement and constructive feedback have been crucial in refining my ideas and turning them into reality.

In addition to my advisor, I would also like to thank to my fellow Ph.D. students. I am thankful for the exchange of ideas, intellectual discussions, and collaborations that have enriched my research journey. Special thanks go to N. Okan Ülgen and D. Korel Yıldırım, whose collaboration and insights significantly contributed to the depth and quality of this thesis.

Lastly, I want to acknowledge the support of the Boğaziçi University, Institute of Biomedical Engineering, its faculty members, and the staff for providing a conducive research environment. Their dedication to nurturing scholarly pursuits has been instrumental in shaping my academic growth.

ACADEMIC ETHICS AND INTEGRITY STATEMENT

I, Doğangün Uzun, hereby certify that I am aware of the Academic Ethics and Integrity Policy issued by the Council of Higher Education (YÖK) and I fully acknowledge all the consequences due to its violation by plagiarism or any other way.

Name :

Signature:

Date:

ABSTRACT

DEVELOPMENT OF NOVEL DEVICE TECHNOLOGIES FOR SAFER MRI GUIDED BIOPSY PROCEDURES

Interventional magnetic resonance imaging (iMRI) is a potent method that combines the benefits of minimally invasive procedures and the exquisite imaging capabilities of MRI. Therefore, performing biopsy operations under the guidance of real-time MR imaging can increase success and safety of operations by promising precise, accurate, and safe MR-guided biopsy operations. Designing visible and safe interventional equipment continues to be a major challenge in this field as MRI develops into a more accessible and suitable imaging modality for interventional procedures. In this thesis study novel device technologies that could improve the success of MR-guided biopsy procedures are introduced and tested. First, a novel optical fiber force sensor was designed and implemented into a needle to provide feedback on the axial force applied to the needle tip during MR-guided biopsy operations. Accurate force measurement, differentiation of different tissue types via stiffness detection capabilities, and the performance of the sensor under MRI were successfully tested through in-vitro experiments. Next, a novel method for increasing the visibility of MR-compatible interventional devices was introduced by using alternating current (AC) controlled conductive ink printed tracking markers. An elaborate analysis was performed to obtain the highest tracking marker conspicuity using the AC-controlled markers and three commonly used MRI pulse sequences. A Custom 20-gauge needle prototype and an MR-compatible current supply circuit were designed. MR-visibility and safety of the prototypes were tested through in-vitro experiments according to the international medical device test standards. Finally, the performance of the needle prototype and the current supply circuit was tested in a post-mortem animal experiment.

Keywords: Interventional MRI, MR-guided biopsy, Fiber-optic force sensors, iMRI device tracking, AC-controlled markers.

ÖZET

MR REHBERLİĞİNDE GÜVENLİ BİYOPSİ İŞLEMLERİ İÇİN YENİ CİHAZ TEKNOLOJİLERİNİN GELİŞTİRİLMESİ

Girişimsel manyetik rezonans görüntüleme, minimal invaziv prosedürlerin faydalarını ve MRG'nin olağanüstü görüntüleme yeteneklerini birleştirebilen etkili bir tekniktir. Gerçek zamanlı MRG rehberliğinde biyopsi işlemlerinin gerçekleştirilmesi, kesin, doğru ve güvenli bir operasyon sağlayarak başarı oranını artırabilir. MRG, girişimsel prosedürler için daha erişilebilir ve uygun bir görüntüleme yöntemi olarak geliştikçe, MR altında görünür ve güvenli girişimsel ekipman eksikliği, bu alandaki gelişimi yavaşlatan önemli bir engel olmaya devam etmektedir. Bu tez çalışmasında, MR rehberliğindeki biyopsi prosedürlerinin başarısını artırabilecek yeni cihaz teknolojileri tanıtılmış ve test edilmiştir. ilk olarak, iğne ucuna etki eden aksiyal kuvveti ölçebilecek yeni bir fiber-optik tabanlı kuvvet sensöru tasarlanarak iğne ucuna yerleştirildi. dizaynlanan iğnenin gerçek zamanlı kuvvet ölçüm kabiliyeti, farklı doku tiplerini sertliklerinden tespit edebilme yeteneği ve sensörün MRG altında performansı, in-vitro deneyler aracılığıyla test edildi. Daha sonra, alternatif akım (AA) kontrollü cihaz takip işaretleri ve iletken mürekkep baskı tekniği kullanılarak MR uyumlu girişimsel cihazların görünürlüğünü artırmak için yeni bir yöntem tanıtıldı. AA kontrollü işaretler ve üç yaygın olarak kullanılan MRG sekansları kullanılarak MR altında cihaz görünürlülüğünü maksimuma çıkarabilmek için ayrıntılı bir analiz yapıldı. Yeni bir 20-Gauge iğne prototipi ve bir MR uyumlu akım kaynağı devresi tasarlandı. Prototiplerin MR görünürlülüğü ve güvenliği, uluslararası tıbbi cihaz test standartlarına göre in-vitro deneylerle test edildi. Son olarak, iğne prototipi ve akım kaynağı devresinin performansı bir ölü hayvan deneyinde başarılı bir şekilde test edildi.

Anahtar Sözcükler: Girişimsel MRG, MR kılavuzluğunda biyopsi, Fiber optik kuvvet sensörü, gMRG cihaz takibi, AA kontrollü cihaz takip işaretleri.

TABLE OF CONTENTS

LIST OF FIGURES

LIST OF TABLES

LIST OF SYMBOLS

B	Magnetic field
E	Electric field
B_0	Main magnetic field
B_1	RF magnetic field
T	Tesla
G	Magnetic field gradients
G_s	Slice select gradient
G_p	Phase gradient
G_f	Frequency gradient
T_1	Longitudinal relaxation time
T_2	Transverse relaxation time
T_2^*	Transverse relaxation time resulted from dephasing G_f
f_0	Larmor frequency
γ	Gyromagnetic ratio
MHz	Megahertz
Hz	Hertz
S	Siemens
Px	Pixel
m	Meter
cm	Centimeter
mm	Milimeter
nm	Nanometer
μm	Micrometer
N	Newton
W	Watt
kg	Kilogram
s	Second
$La_3Ga_5SiO_14$	Quarts langasite (Piezo langasite)

$BaTiO_3$	Barium titanate
CO_2	Carbon dioxide
SiO_2	Silicon dioxide
$CuSO_4$	Copper sulfate
PZT	Lead zirconate titanate
$PVDF$	Polyvinylidene flouride
Ti	Titanium
Al	Aluminum
Mg	Magnesium
n_1	Refractive index of medium 1
n_2	Refractive index of medium 2
λ	Wavelength
Fr	French
G	Gauge
C	Capacitance
L	Inductance
f_R	Resonant frequency
w_0	Angular frequency
mA	Milliampere
V	Volt
ΔL_c	Cavity length change
F	Force
μ	Poisson's ratio
F	Force
L_G	Gauge length
E	Elastic modulus
R_o	Outer diameter
R_i	Inner diameter
kPa	Kilopascal
^0C	Celcius degree

LIST OF ABBREVIATIONS

MRI	Magnetic resonance imaging
$iMRI$	Interventional magnetic resonance imaging
MR	Magnetic resonance
RF	Radio frequency
CT	Computed tomography
NIH	National Institutes of Health
$NHLBI$	National Heart Lung and Blood Institute
TR	Repetition time
TE	Echo time
BW	Bandwidth
FOV	Field of view
FA	Flip angle
SAR	Specific absorption rate
$DICOM$	Digital imaging and communications in medicine
GRE	Gradient echo
$b-SSFP$	balanced steady state free precession
SE	Spin echo
TSE	Turbo spin echo
$RARE$	Rapid acquisition with relaxation enhancement
FID	Free induction decay
$ASTM$	American Society for Testing and Materials
USA	United States of America
PSA	Prostate specific agent
BPH	Benign prostatic hyperplasia
$TRUS$	Transrectal ultrasound
LED	Light emitting diode
MZI	Mach-Zender interferometry
FPI	Fabry-Perot interferometry

FBG	Fiber Bragg gratings
UV	Ultraviolet
SNR	Signal-to-noise
$2D$	2 Dimensional
$3D$	3 Dimensional
DC	Direct current
AC	Alternating current
ADC	Analog-to-digital converter
bjt	Bipolar junction transistor
OD	Outer diameter
ID	Inner diameter
PC	Personal computer
NH	New Hampshire
MA	Massachusetts
NJ	New Jersey
UT	Utah
$p-p$	Peak-to-peak

1. INTRODUCTION

When accurate diagnosis cannot be achieved through tissue imaging alone, the utilization of biopsy procedures becomes essential. Image-guided percutaneous biopsies have gained prominence over conventional methods due to their ability to provide highly accurate results while minimizing invasiveness. Among the various imaging modalities, MRI-guided biopsies offer several advantages. These include superb soft tissue contrast, rapid imaging with multiple planes, superior spatial resolution, and an environment free from ionizing radiation. Such advantages can position MRI as the preferred modality for imaging during numerous biopsy procedures, ensuring operational success and ensuring the safety of both patients and physicians. However, MRI-guided biopsies present unique challenges that must be addressed to enable safe and effective procedures.

The existence of both a strong static magnetic field, and dynamic magnetic fields such as gradient fields and RF pulses used in magnetic resonance imaging (MRI), imposes significant limitations on the use of conventional electronic components and interventional devices within the MR environment. Metallic devices can experience magnetically induced force or torque, leading to safety concerns. Even if the device remains unaffected by these magnetic forces, RF-induced heating on metallic devices can reach hazardous levels. Furthermore, interventional devices or implant materials can produce substantial artifacts on MR images, obstructing the visualization of underlying anatomical structures. Interventional devices which are entirely safe to use under MRI or devoid of metallic components often suffer from low conspicuity and lack trackability during procedures.

Consequently, addressing these challenges necessitates the development of innovative approaches and custom devices that ensure safety within the MR environment while enabling real-time MR-guided localization and tracking of the interventional device.

2. BACKGROUND

2.1 Image-guded minimally invasive interventions

Advances in real-time medical imaging technologies like x-ray fluoroscopy, computed tomography (CT), ultrasound, and magnetic resonance imaging (MRI) made it possible to perform image-guided minimally invasive therapeutic or interventional diagnostic operations [1]-[3]. Instead of performing open surgery, image-guided minimally invasive procedures can reach the target area by entering through a small skin incision using interventional medical devices such as needles, catheters, guidewires, etc [4]-[6]. Minimally invasive procedures can be advantageous, especially for older and younger patients who can't withstand the conventional open surgery methods, and some of these advantages can be fewer complications, decreased trauma, postoperative pain, infection risks, discomfort, recovery time to the patient and overall medical cost [7]-[10]. These remarkable advantages of image-guided minimally invasive procedures are very desirable, but they come with the price of having a limited view of the target anatomy, and access to the body cavity [11],[12]. Therefore, choosing the correct imaging modality that would provide fast and high-quality images and designing interventional medical devices that can be both safe, accurate, and trackable under these imaging technologies are crucial for the success of these minimally invasive operations.

2.2 Physics of magnetic resonance imaging

Protons in Hydrogen atoms which can create a magnetic dipole with their spin angular momentum are most commonly used for generating images in magnetic resonance imaging. A strong static main magnetic field that exists in the scanner bore aligns the magnetic dipole of hydrogen atoms and protons and makes them start to precess in the same direction (static magnetic field direction). The frequency of the precession of these proton atoms is the Larmor frequency and it is calculated with Eq.

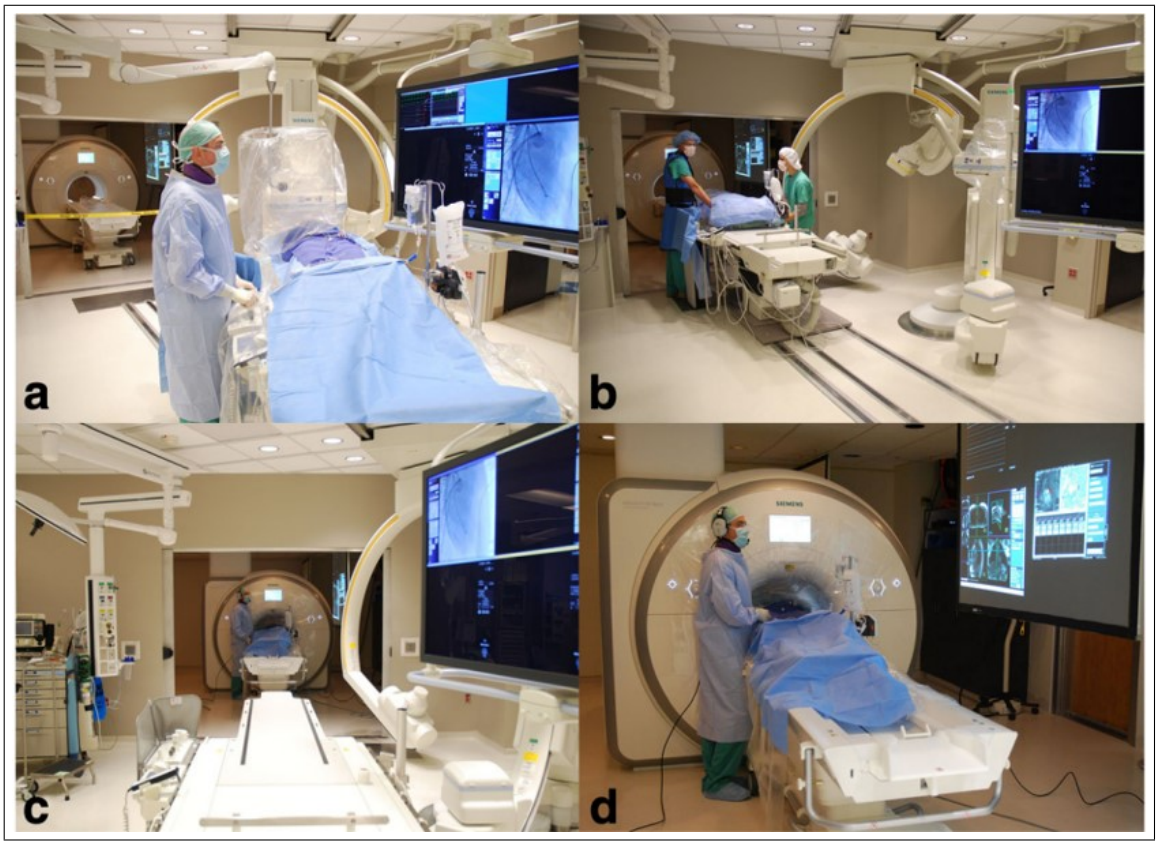

Figure 2.1 Figure Image-guided right heart catheterization procedure at Interventional CMR cardiac catheterization laboratory at National Heart Lung and Blood Institution (NHLBI) at National Institutes of Health (NIH) [13].

2.1 given below [14]. In the given equation f_0 is the Larmor frequency, γ is the gyromagnetic ratio, which is 42.58 MHz/T for hydrogen atoms, and B_0 is the externally applied main magnetic field of MRI. Using this equation, the resonance frequency of hydrogen atoms in a 1.5 T scanner would be 63.87 MHz and in a 3T scanner, it would be 127.74 MHz.

$$f_0 = \gamma \cdot B_0 \tag{2.1}$$

The magnetic dipole moments generated from these protons precessing with respect to the direction of the static high magnetic field are superimposed and form a net magnetization. An external radio frequency (RF) wave is exposed to the Hydrogen atoms next and flips the direction of the net magnetization at a specific degree which is

called the flip angle. Once the radio frequency signal is deactivated, proton's precessions returns to their original alignment, which corresponds to the magnetic field's direction. This phenomenon is called relaxation and time required for the relaxation is called the relaxation time. This net magnetization change during the RF pulse application in the transversal and longitudinal axes can be measured using Receiver RF coils. Since different tissue types contain different Hydrogen densities relaxation times after the RF pulse varies between different tissues such as fat or muscle. A contrast and hence, an image can be generated using this difference in the relaxation times and difference in the hydrogen densities in the anatomy [15],[16].

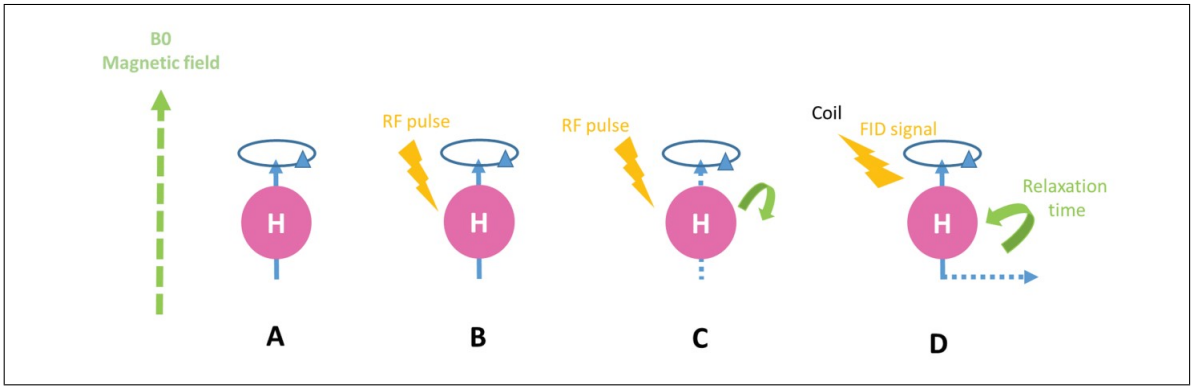

Figure 2.2 Figure Principles of magnetic resonance imaging **A.** Hydrogen atom under strong magnetic field **B.** RF pulse application **C.** Relaxation **D.** Protons emitting RF signal during relaxation [17].

Figure 2.2 shows how the protons act during the MRI scan before and after the RF pulse [17]. The signal intensity of the MRI and hence, MRI contrast and Signal-to-noise ratio of the image depends on the hydrogen density and transversal and longitudinal relaxation times of the target tissue. To be able to form an image using the obtained signal, The received MRI signal needs to be spatially encoded. Linear magnetic field gradients (G) can be used for spatial encoding for MRI images [18]. Applying external gradient fields on top of the main magnetic field and with an amplitude linearly changing with respect to the location inside the MRI bore makes the protons precess in different frequencies in different locations. Creating this difference in 3 axes by applying gradient fields makes it possible to select a slice to be imaged with the slice selection gradient (Gs). After that spatially encode the MRI signals

received by the RF coils into that slice with the phase encoding gradient (Gp) and the frequency encoding gradient (Gf) fields. As an example, a gradient echo (GRE) pulse sequence diagram with respect to time is given in Figure 2.3 [19].

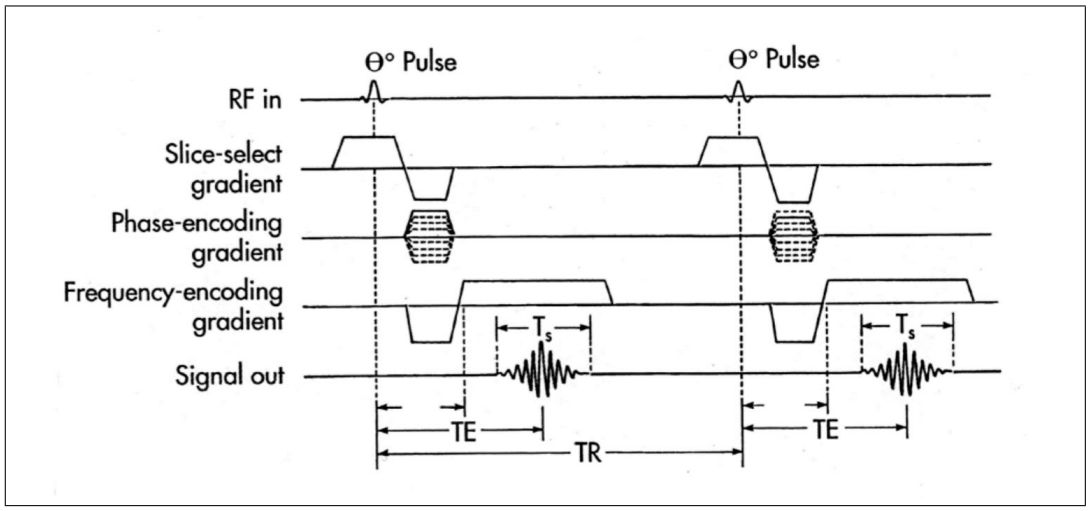

Figure 2.3 2D Gradient Echo (GRE) pulse sequence diagram [19].

In summary, the three primary components that make up the MRI's operating system are the main magnetic field that aligns the magnetic dipole moment of hydrogen atoms that results in a net magnetization, externally applied RF pulses for flipping the net magnetization and obtaining transversal and longitudinal signals and linear magnetic field gradients for spatial encoding for the image formation. Three fundamental parts of an MRI scanner hardware that are responsible for creating the main magnetic field (B0), creating the RF pulses and reading the resulting MRI signal, and finally creating the linear magnetic field gradients are main magnet, RF coils, and gradient coils respectively. Figure 2.4 shows the main elements of an MRI scanner[20].

2.3 MRI guided biopsy

In the early years of magnetic resonance imaging, it was not considered as a suitable technology for providing guidance during interventional operations. The strong magnetic field of MRI made it very difficult and unsafe to use conventional interventional devices, its closed bore geometry limited the physicians' or operators'

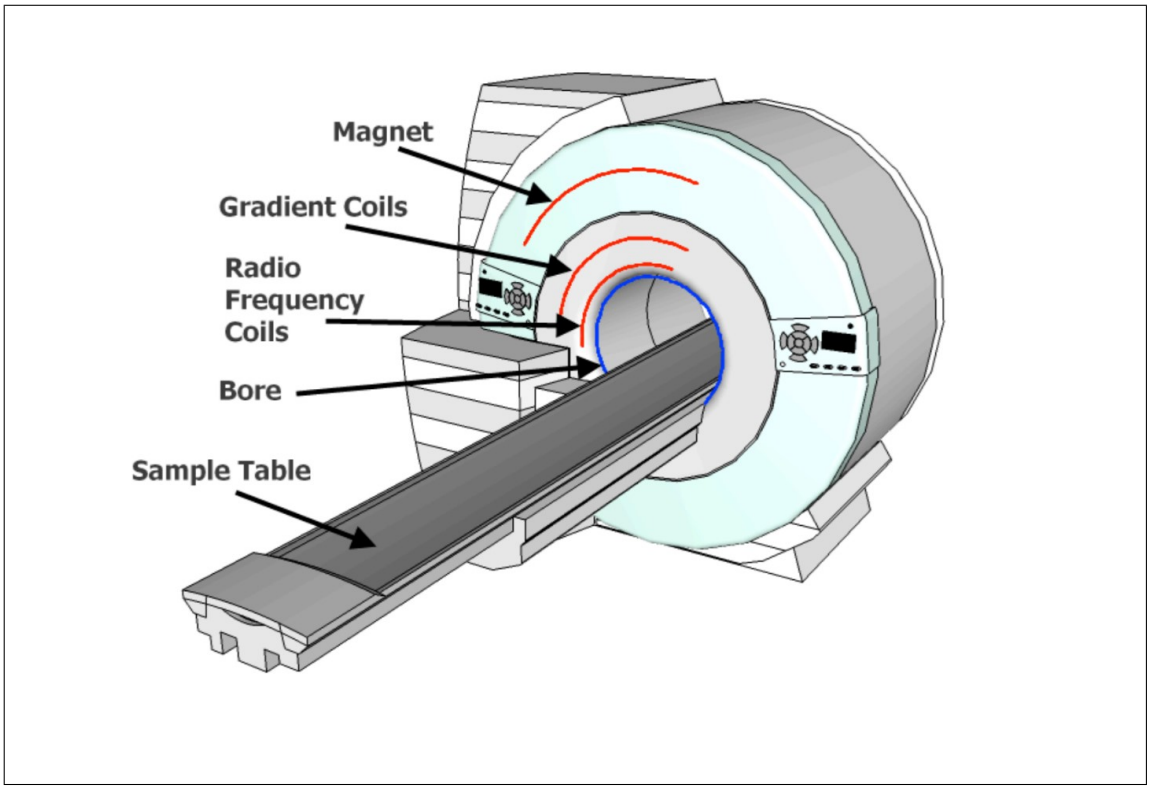

Figure 2.4 Components of an MRI scanner [20].

freedom during the operation and long scan times made it impossible to perform a real-time procedure under MRI [21]. Improvements in MRI technologies such as being able to obtain high-quality images using scanners with low field strength, new pulse sequences like GRE (gradient echo) or b-SSFP (balanced steady-state free precession) that can generate fast and good quality images, and custom-designed interventional devices that can be both safe and trackable under MRI made it possible to overcome the disadvantages and difficulties of MR-guided interventional procedures.

Despite having all these difficulties, using MRI as an interventional modality is still very desirable because of the advantages it can offer. Some of the advantages of MRI are listed below [22]-[27]:

1. Excellent soft tissue contrast

2. Fast imaging with multiple planes

3. Ability to distinguish various organs and blood vessels
4. High spatial resolution
5. Ionizing radiation-free nature

These significant advantages make MRI guidance a very desirable imaging modality for interventional minimally invasive procedures.

A biopsy operation is performed when imaging the tissue alone is not sufficient to accurately diagnose the patient and further tissue diagnosis through cytologic, microbiologic or histologic evaluations is needed [28]. The first needle biopsy operation was performed in 1883 without any image guidance and as physicians gained experience and improvements in histopathologic methods percutaneous biopsies became more popular even without the interventional imaging modalities [29]-[36]. With Roentgen's discovery of x-ray and discoveries and improvements of new imaging technologies like x-ray fluoroscopy, CT, ultrasound, and lastly magnetic resonance imaging, image-guided needle biopsy became a much safer and more precise method for the procedure [37]-[41].

All the imaging modalities mentioned before has their own advantages and disadvantages. Compared to CT and MRI, ultrasound seems like a convenient modality for guided biopsy procedure because it is a portable device that is simple to operate that can provide real-time control of images with different planes and trajectories during the procedure without ionizing radiation. However, its soft tissue contrast is not as good as CT or MRI and visualization is limited with the distance that soundwaves can travel in the tissue therefore deep and complex anatomical structures may not be visualized very well. CT provides a good soft tissue contrast but during a CT guided interventional operation high levels of harmful radiation are exposed on both the patient and the doctor.

MRI provides both exquisite soft tissue contrast so that lesions that cannot be seen under ultrasound and CT, can be detected under MRI and rapid multiplanar

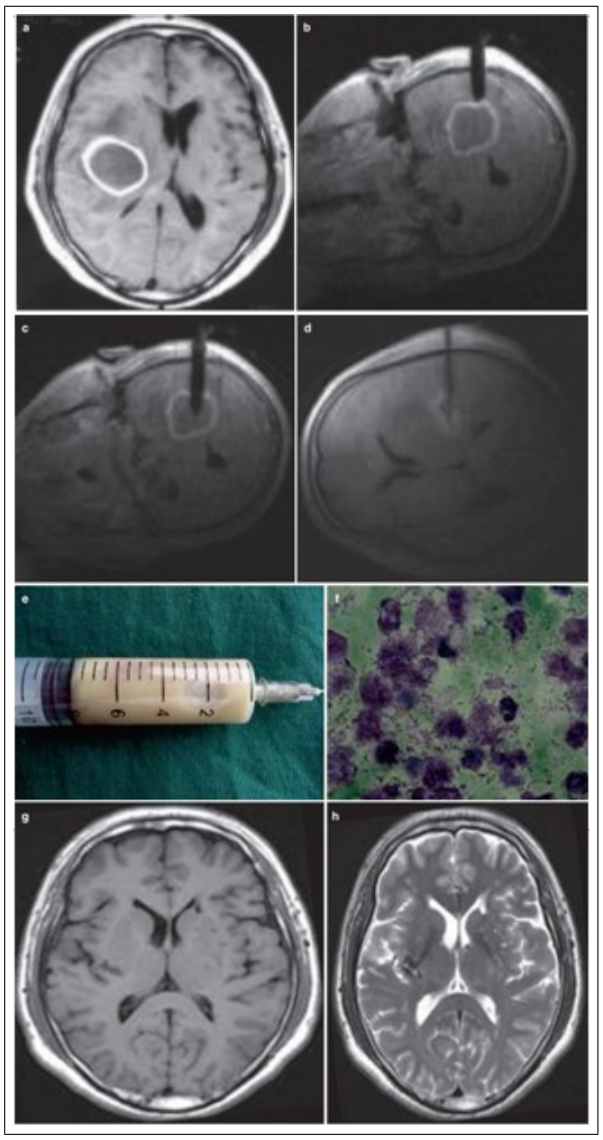

Figure 2.5 Brain aspiration under MRI [42].

imaging with the use of suitable pulse sequences without ionizing radiation. One important disadvantage of MRI concerning the biopsy procedure is its high magnetic field which makes it difficult to use conventional biopsy needles because of the safety problems that magnetic needles can cause and the low conspicuity of non-magnetic needles under MRI. Improvements in MRI technologies and MR-compatible medical devices make MRI-guided biopsies more promising and more popular every day. Percutaneous biopsy and aspiration procedures were performed successfully many times with MRI guidance in various areas of the body from various tissues. Some examples of MRI-guided biopsy and aspiration procedures from the literature are given in Figures 2.5,

2.6, and 2.7. In Figure 2.5 it can be seen step by step that an aspiration procedure was performed in the brain. An abscess and its location in the brain were detected under MRI, an aspiration needle was inserted and tracked until it reaches the target area and the abscess was drained until the area is cleared from it and finally, the fluid was sent for further inspection.

In their study, Moche et al performed 55 biopsies from liver in 52 patients under MRI [43]. Figure 2.6 shows the MR image (on the right) during the liver biopsy operation. The target area, the target lesion, and the biopsy needle can be seen clearly under MRI thanks to its exquisite soft tissue contrast. CT image of the same target area is shown on the left of Figure 2.6 and the target lesion that a biopsy sample was supposed to be taken is not visible at all.

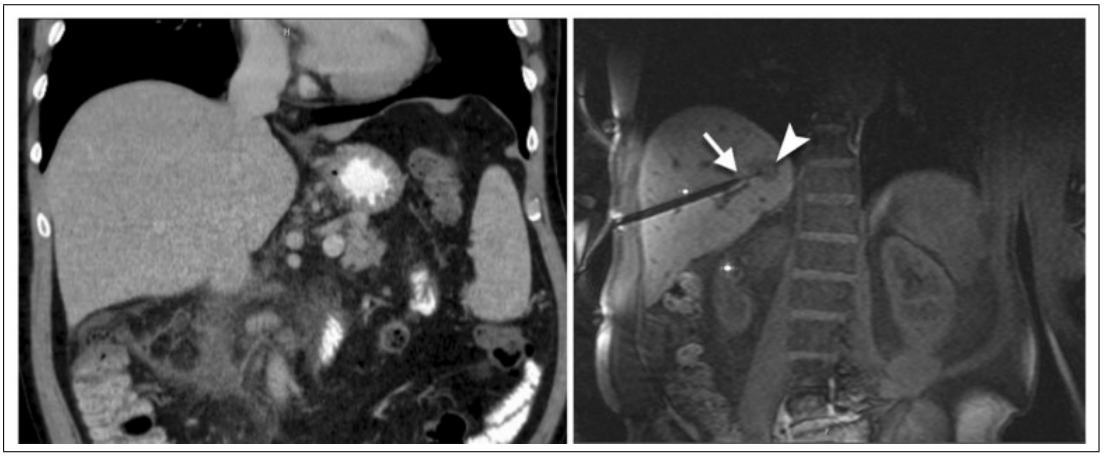

Figure 2.6 Liver biopsy operation under MRI (right) and CT image of the same area (left) [43].

Schneider et al. performed breast biopsies under MRI for 21 women with MRI-only visible lesions in their study [44]. Different imaging modalities such as mammography, and sonography can be used for tumour detection in breast tissue and cancer diagnosis along with physical examination and MRI has taken its place among these conventional imaging modalities as a very effective one [45]. MRI's excellent soft tissue contrast allows physicians to detect lesions in the breast that can only be seen under MRI [46]. Therefore, MRI-guided biopsy can be the best option for suspicious lesions that are only visible under MRI [47],[48]. In Figure 2.7 [44] an MRI image during the biopsy operation is given. The suspicious lesion in the breast tissue and the biopsy

needle are shown in the image.

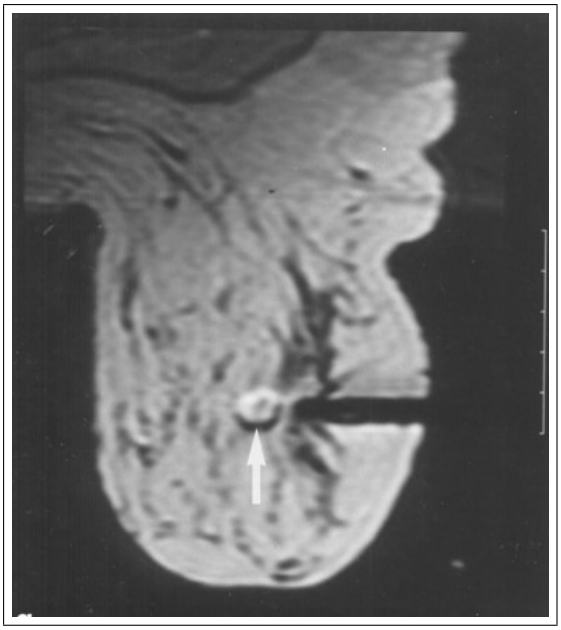

Figure 2.7 MRI guided breast biopsy [44].

2.3.1 MRI guided prostate biopsy

One of the most prevalent types of cancer among men in the United States of America is Prostate cancer [49]. Every year more than one million prostate biopsy operation is performed both in Europe and the USA [50]. For the year 2022, estimated 268,490 new cases and estimated 35,400 deaths for prostate cancer are given by Siegel et al. in their study [49].

PSA (prostate-specific antigen) levels in the blood and a digital rectal exam are the first steps in the diagnosis of prostate cancer. [51]. The level of PSA increases in the blood of people who has prostate cancer [52] as well as people who have prostatitis, benign prostatic hyperplasia (BPH), and people who undergo prostate biopsy [53]. Therefore, increased PSA levels in a blood test can result in a false positive result and can give rise to further diagnostic and therapeutic procedures that are not actually necessary [54]. In digital rectal examination physicians examine the prostate with their fingers through the rectum and look for a stiffness change in the prostate tissue.

In this case, it may not be possible to examine every region of the prostate tissue. Although only a blood test to check PSA level and a digital rectal examination is not sufficient for a prostate cancer diagnosis, it can be crucial for early diagnosis and easier treatment. Prostate cancer is not the only cause of an increase in the Blood PSA level [52], and it is not possible to detect the cancer stage or if the tumor is malignant or benign with the blood PSA level or digital rectal examination. Therefore, generally, prostate biopsy is performed for a more accurate diagnosis.

One of the most popular techniques for prostate biopsy operation that is used in clinics today is transrectal ultrasound (TRUS) guided prostate biopsy (figure 2.8). TRUS-guidance employs an ultrasound probe to obtain a real-time image of the target organ and generally ten to twelve suspicious tissue samples are collected from various locations of the prostate tissue using biopsy needles. It is not easy to differentiate the healthy and the tumorous tissue under ultrasound therefore using an increased number of biopsy samples results in a better accuracy for the diagnosis. Besides the high patient discomfort during the biopsy operation, Increasing the number of biopsy samples can also cause bleeding, urinary retention, urinary obstruction, infection, vasovagal reaction, dysuria, and sepsis [55],[56].

Taking 10-12 samples from different regions of prostate tissue without knowing the precise position of the suspicious lesion in the target organ sometimes results in false negative outcomes or the need for another biopsy operation. In their study, Seferoglu et al. evaluated the false-negative risk of TRUS-guided prostate biopsy [56]. They performed ex-vivo 12-core prostate biopsies on 90 patients who were diagnosed with prostate cancer. Seferoglu et al. claimed that using repeated 12-core prostate biopsy, cancer detection was successful only at 67.8 % of 90. A high number of false negatives in this study, due to performing the biopsy operation with a random sampling because of the lack of soft tissue visualization capabilities of ultrasound probes can be avoided by performing the biopsy operation under MRI

The main purpose of performing the prostate biopsy operation under MRI is decreasing the false negative outcomes of conventional methods without the need for

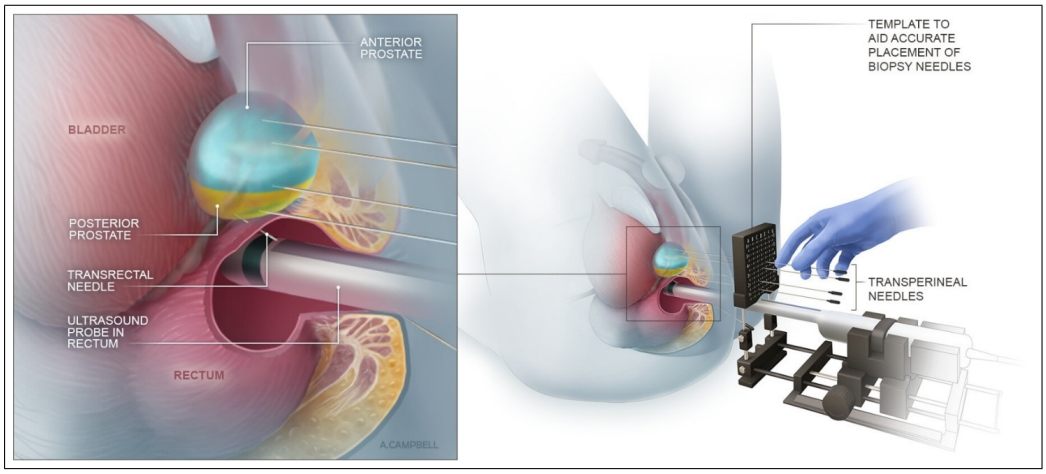

Figure 2.8 TRUS Guided Prostate Biopsy [57].

high number of tissue samples. There are 3 main methods that MRI is used for prostate biopsy operation namely: Software assisted ultrasound MRI fusion targeted biopsy, visual directed MRI targeted biopsy, and finally in-bore direct MRI targeted biopsy [58]. In visual directed MRI targeted biopsy, the patient is scanned under MRI and the target tumorous tissue is detected using MRI before the biopsy operation. After detecting the tumorous lesion, TRUS guidance is used for the biopsy operation [59],[60].

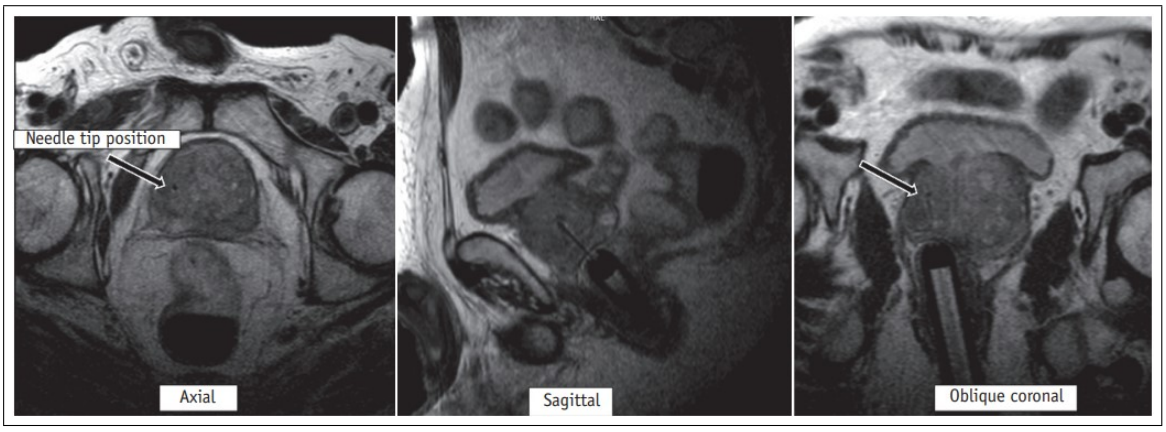

Figure 2.9 MRI-guided prostate biopsy operation [64].

In software-assisted ultrasound-MRI fusion targeted biopsy, a patient is scanned under MRI, and the target tumorous tissue is detected before the operation. Using a software MR image of the prostate and the lesion is registered/superimposed to the real-time ultrasound image during the operation [61],[62]. In-bore direct MRI

targeted biopsy is performed using only MRI for imaging during the biopsy operation [63]. Both visually directed biopsy and software-assisted fusion biopsy increases the success of the operation but doesn't provide real-time MRI guidance during the biopsy operation. Therefore, misregistration between the MRI image and the ultrasound image can cause problems or patients' prostate might move inside their body during biopsy needle insertion which could cause to further difficulties and false negative results. Although in-bore direct MRI-guided biopsy increases the accuracy of the operation by using rapid MRI images (close to real-time) for needle guidance, this method requires MRI-compatible and visible interventional devices so that a safe and successful biopsy operation can be performed. Figure 2.9 shows axial, sagittal, and coronal MRI images of an in-bore direct MRI-targeted prostate biopsy operation [64]. The prostate tissue and the needle tip position are visible in the axial image. The sagittal and coronal images show the needle tip and shaft inserted into the prostate.

2.4 Needle tip force sensing

2.4.1 Needle tip force feedback

The use of needle-like equipment in medicine goes all the way back in history to ancient Egyptians [65]. The history of modern needles and syringes in medicine on the other hand is more recent than that. Blood circulation in the anatomy is first described by William Harvey [66] and the idea of injecting liquids directly into the blood came up with that discovery. Christopher Wren injected wine and ale into dogs to experiment the intravenous injections using a needle [66]. Daniel Ferguson and Alexander Wood invented the medical needle with a sharp tip that could inject liquids into the body and Charles Pravaz invented a needle with a detachable syringe [65].

In the light of these inventions the ability of intravenous injections and to be able to reach spots that are deep in tissue lead to different needle designs for various purposes. Apart from intravenous injections needles are used in many therapeutic and diagnostic procedures in modern medicine today such as: introducing invasive access to

the target tissue, regional anesthesia, ablation, catheterization, deep brain stimulation, brachytherapy, neurosurgery, and biopsy [67],[68]. Force measurement at the needle tip can be crucial for operations that need high precision such as epidural needle injections.

Tactile feedback from the needle during an operation is a very important factor for physicians. Being able to feel the mechanical characteristics of tissues especially the different stiffness levels of different tissue types and needle membrane interactions through the course of the needle presents essential information about the location of the needle inside the patient's body and can be crucial for a successful operation. As an example, physicians use haptic feedback during conventional open surgeries to differentiate and detect tumorous tissues by palpating the target tissue [69]. During minimally invasive operations, on the other hand, it can be impossible to examine the target tissue with palpation.

Percutaneous tissue biopsy, also called needle biopsy is the procedure that is performed by collecting tissue or cell samples from the suspicious tissue when there is a cancer suspicion. The two most usual types of needle biopsy are needle aspiration and core needle biopsy. In needle aspiration, liquid cell samples are collected from the target area using a thin needle in a syringe. In core needle biopsy a piece of tissue sample is cut and collected using a cutting needle. For a core needle biopsy, a larger diameter needle is used compared to the aspiration needle. Image guidance can be very helpful for a safer and more accurate biopsy operation by performing the procedure under CT, ultrasound, or MRI. Even with image guidance, using minimally invasive medical tools such as biopsy needles requires years of experience and advanced skills to operate safely and accurately.

Placing a force sensor at the distal tip of the biopsy needles can provide tactile feedback in real-time to the physician during the operation. Robotically assisted biopsy procedures especially benefit from real-time needle tip force measurements since the physician-needle contact is lost and the tactile feedback that comes from the needle is lost without a force sensor. Different stiffness levels of different tissue membranes such as the skin or prostate tissue, breast tissue, muscle or fat tissue, or even different

stiffness levels of benign and malignant tissues can be detected using a needle tip force sensor during needle insertion. Needle tip force measurements could increase the procedure's safety as well. Using excessive force on the biopsy needle may result in scarring, infections, tissue death, and compromised surgical procedures [70].

2.4.2 Conventional force sensors

2.4.2.1 Capacitive force sensors. Capacitive force sensors take advantage of parallel plate capacitors for force and pressure measurements. The capacitance is inversely related to the gap separating the parallel plates of the capacitor. Therefore, Applying force or pressure to one of the parallel plates can decrease the gap between the plates and hence the capacitance of the capacitor. Therefore, the force measurement can be achieved by measuring the capacitance of the parallel plate capacitor. A simple diagram of the working principle of a capacitive force sensor is given in Figure 2.10. Capacitive force sensors have advantages such as high sensitivity, high resolution, stability, durability, and large bandwidth [71].

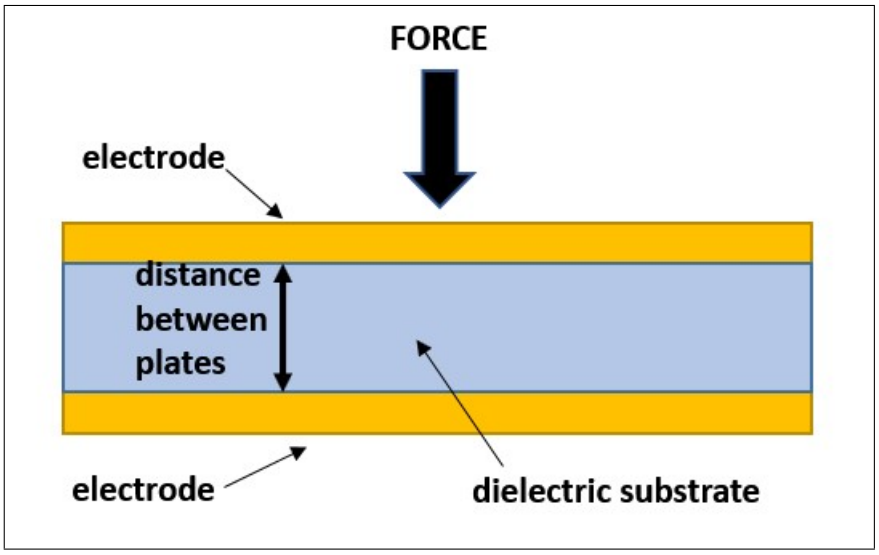

Figure 2.10 Capacitive force sensor.

2.4.2.2 Inductive force sensors. Inductive sensors are widely used for measuring proximity (distance) by taking advantage of the change in the electromagnetic fields

around the sensor. A varying current flowing on an inductive coil creates electromagnetic fields around the coil and a changing electromagnetic field can create current on the inductive coil. Therefore, when the electromagnetic field around the coil is disrupted or changed by nearby materials such as metallic objects or other coils the inductance of the coil or the current value flowing along the coil changes accordingly. This change depends on the distance between the inductive coil and the field-disrupting material. Using the same principle inductive sensors can be used for measuring proximity, pressure, flow force, etc. The three main types of inductive sensors are namely, self-inductive sensors, mutually inductive sensors, and eddy current sensors. As an example, Du et al. designed an inductive force sensor that can measure real-time force distributions that are applied on a foot for patients with diabetes. Figure 2.11 shows the schematic of the inductive force sensor given in the study [72].

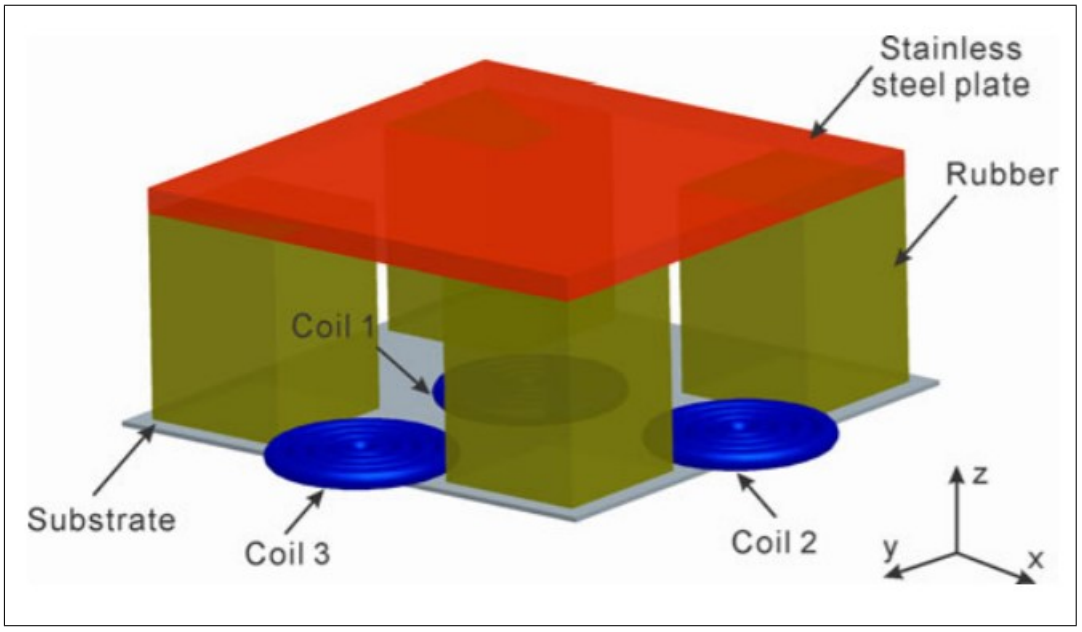

Figure 2.11 Inductive force sensor [72].

2.4.2.3 Piezoelectric force sensors. Piezoelectric sensors take advantage of piezoelectric materials to convert parameters like force, strain, or pressure to electrical signals. Piezoelectric materials generate an electric polarization when they are exposed to a mechanical change such as strain or pressure and vice versa, when an electrical signal is applied to piezoelectric materials they can generate a movement, vibration, or

force. The operating principle of piezoelectric transducers is presented in Figure 2.12. Some examples of piezoelectric materials can be piezoelectric crystals such as Quartz, Langasite (La3Ga5SiO14) [73], piezoelectric ceramics such as Lead zirconate titanate (PZT), barium titanate (BaTiO3) [74], Piezoelectric polymers such as Polyvinylidene fluoride (PVDF) [75], and biological piezoelectric materials such as tendon and enamel [76].

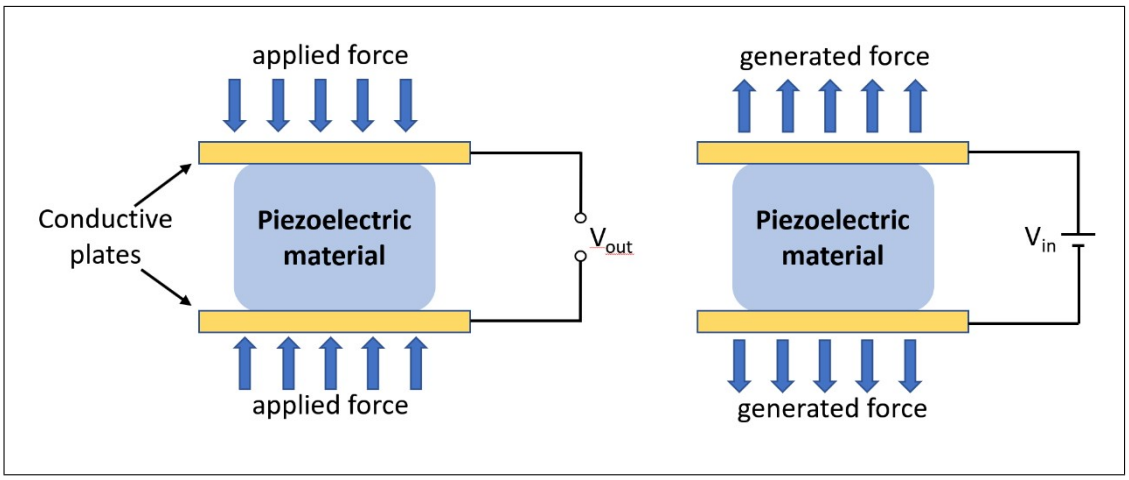

Figure 2.12 Piezoelectric force sensor schematics [72].

Piezoelectric materials are widely used for designing sensors in various areas. Gil et al. show their design of a catheter tip miniature force sensor using PVDF piezoelectric material that could help increase the success of surgical interventions [77]. One of the advantages of piezoelectric force sensors is that they can be fabricated very small which makes them desirable for medical applications. Their high-frequency range is another advantage of piezoelectric sensors. They can be used for both generating and sensing sound waves as an example and can be used in different medical imaging modalities such as ultrasound imaging [78].

2.4.2.4 Piezoresistive force sensors. Piezoresistive force sensors are simple to design, affordable, have high endurance, and provide high resolution and wide-range measurements. These advantages make piezoresistive sensors widely used in many areas. In Piezoresistive sensors, the applied external force or pressure creates a strain on the sensing element of the sensor. This applied pressure or force changes the sensing

element's resistance. The change in the resistance and the strain are directly proportional to each other. As a result, the change in the electrical properties of the piezoresistive sensing element can be used to measure the applied force or pressure. The most popular method of measuring this change in resistance as voltage is to create a Wheatstone bridge circuit employing the sensor's piezoresistive sensing device, as presented in Figure 2.13.

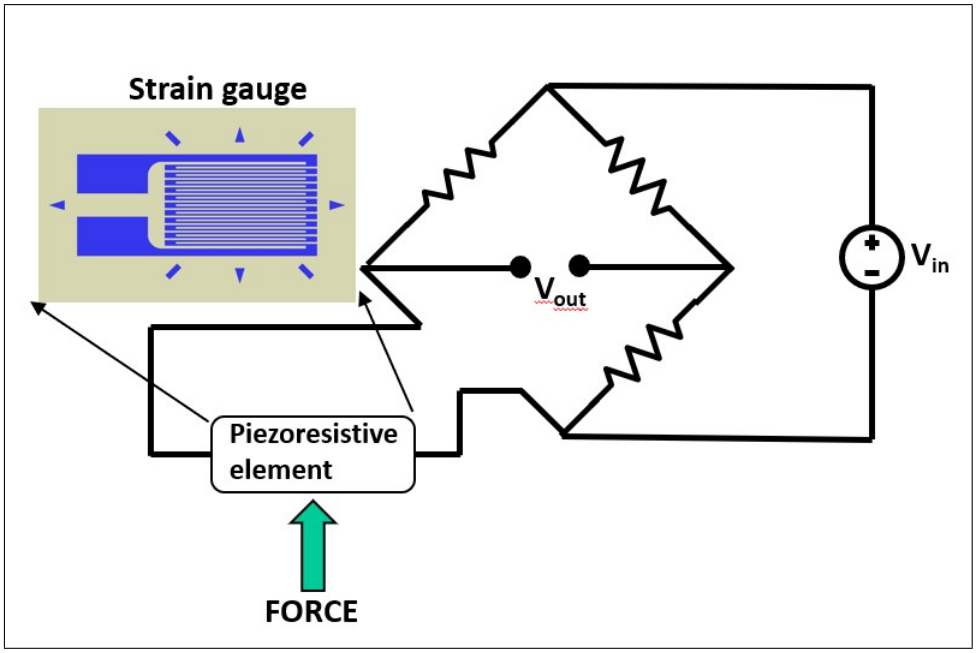

Figure 2.13 Piezoresistive force sensor schematics using a strain gauge and a Wheatstone bridge [72].

Wheatstone bridge design makes it possible to translate slight variations in the sensor's resistance into an output voltage. When an input voltage is applied to the Wheatstone bridge circuit, The output voltage will not change and remain zero if there is no change in the resistors. A change in applied force on the piezoresistive element will break the balance of the bridge circuit and it will affect the output voltage in a comparable way. The strain gauge is one of the most common examples of resistive strain sensors. It was invented by Arthur C. Ruge and Edward E. Simmons [79]. Strain gauges are designed with a conductive path with a zig-zag pattern placed on an insulator thin film. Applied force changes the shape of the conductive pattern and the resistance of the strain gauge changes with it.

2.4.3 Optical fiber force sensors

2.4.3.1 Optical fibers. Optical fibers are transparent dielectric materials that light can propagate inside with the total internal reflection principle. Transferring photons this way from one point to another provides a way of data transmission. Optical fibers are commonly composed of 3 fundamental layers named core, cladding, and jacket (figure 2.14). Core is the inner layer of the optical fiber, which has a uniform and high refractive index and, it is the layer the light travels. Cladding is the middle layer of the optical fiber, and it makes sure that the light stays inside the core according to the total internal reflection principle by having a refractive index lower than the core. Lastly the jacket (buffer) is the outer layer of the optical fiber, and it provides protection for the internal layers.

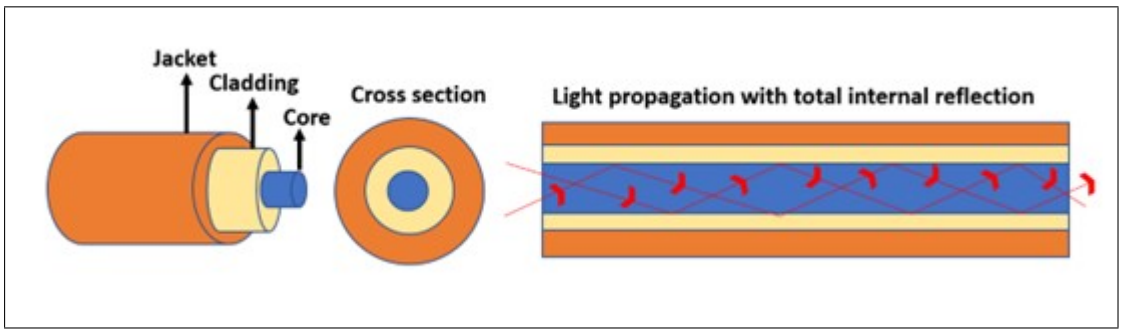

Figure 2.14 Optical fiber elements.

Light interacts with the medium that it travels inside therefore the speed of light differs in different media such as air, water, or glass. The speed of light changes when it passes from one medium to another and this change in speed causes a bending in the direction that light travels. This phenomenon that causes bending in the direction of a wave is called refraction. The refractive index for specific materials is defined using this phenomenon by dividing the speed of light in a vacuum by the speed of light in that specific material.

$$n_1 \cdot \sin\theta_1 = n_2 \cdot \sin\theta_2 \tag{2.2}$$

Snell's law describes the relationship between the refractive indexes of media and the bending of light's direction when the light transfers between the two media. Snell's law is given in Figure 2.15 and Eq. 2.2. Here The refractive indexes of media 1 and 2 are denoted by n1 and n2, respectively. and, θ_1 and θ_2 are the angles that the light makes with the normal vector of the interface surface between the two media. θ_1 is called the incidence angle and θ_2 is called the refraction angle. Going from a higher to lower refractive index medium after a certain incidence angle the light starts to reflect completely from the incidence surface instead of refracting. This angle is called the critical angle. Optical fibers keep the light inside the fiber core with a total internal reflection based on this phenomenon.

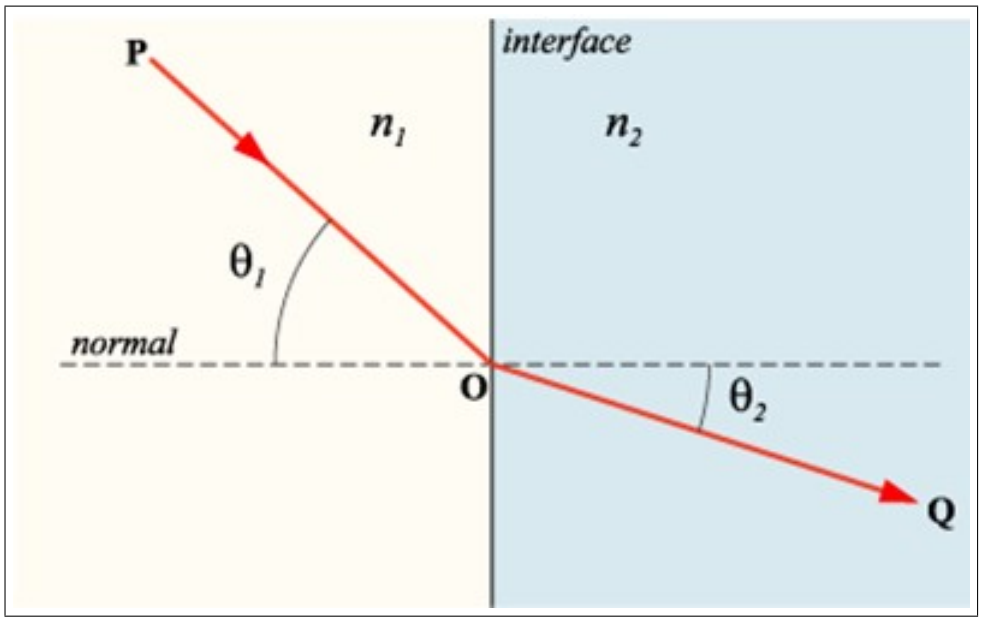

Figure 2.15 Snell's law.

Using optical fibers for data transfer and communication has advantages and disadvantages but the most important advantage of optical fibers in the field of interventional MRI is its raw material. Optical fibers are, most commonly, composed of silicon dioxide (SiO_2) which is non-metallic, non-magnetic, and electrically non-conductive which makes them intrinsically safe to use in high magnetic field environments [80]. Some of the other advantages of optical fibers are given below [81]:

1. High speed

2. High bandwidth
3. Low cost
4. Minimal power loss which results in data transfer to longer distances
5. Immune to electromagnetic interferences
6. Ability to withstand harsh environments
7. small and compact

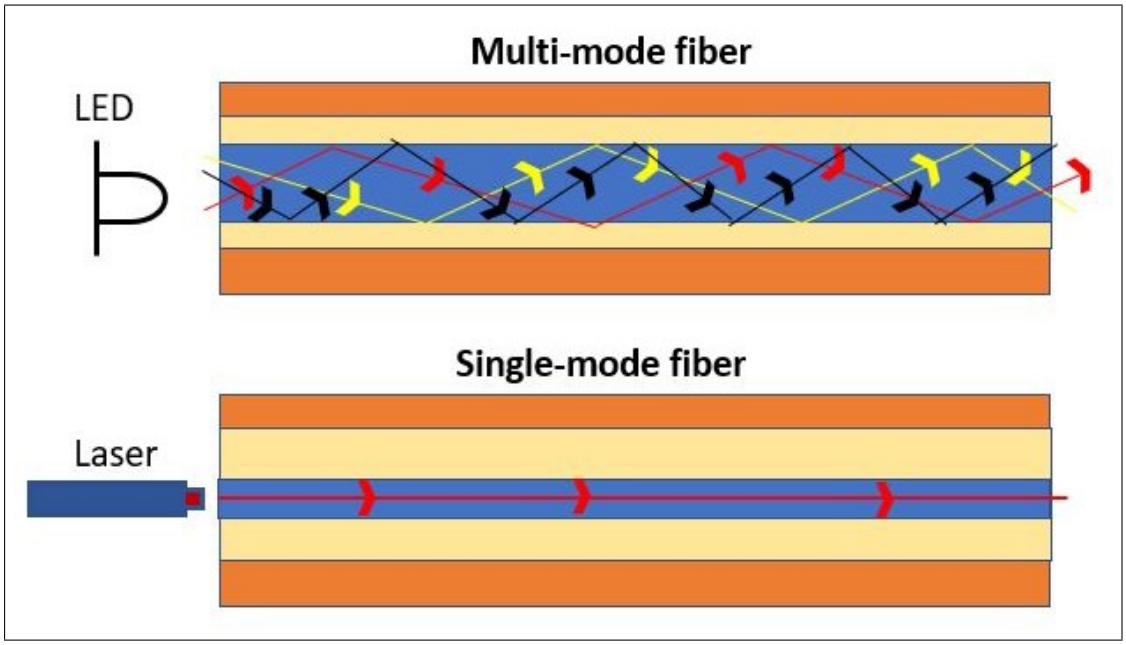

Figure 2.16 Optical fiber types.

There are two primary categories of optical fiber: single-mode fiber and multi-mode fiber. The main difference between the two types of optical fibers is the core diameter. Compared to multi-mode fibers, single-mode fibers have a substantially smaller core diameter which results in differences in the propagation of the light inside the optical fibers. While the single-mode fibers can only carry single light mode (single ray of light) multi-mode fibers can carry multiple modes at the same time. Single-mode fibers' narrow core diameter minimizes the power loss of the signal because it decreases the number of reflections through the optical fiber cable. On the other hand, small core diameter makes it more difficult to couple the light into the optical fiber cable,

and therefore single mode fibers are generally used with laser diodes while multimode fibers are compatible with cheaper light sources such as LEDs.

2.4.3.2 Fiber optic interferometry based sensors. Optical fibers are used in numerous studies in the literature for designing sensors to measure various physical inputs such as force, pressure, temperature, displacement, ultrasound, refractive index, and more [82]-[86]. A very important characteristic of waves is the ability to interfere with each other. Fiber optic sensor technology often takes advantage of light interferometry to design interferometric fiber optic sensors. Two or more light waves can create an interference pattern, in other words, they can be at the same place at the same time and superimposed on each other. When the waves are in phase, they form a constructive interference and when they are out of phase, they form a destructive interference. Therefore, the light intensity of a certain point on the interference pattern can be related to the path difference (the difference in phase) between two known light waves. This idea forms the basis for interferometric fiber optic sensors. The four types of interferometric fiber optics sensors are namely, Mach-Zender interferometer (MZI), Michelson interferometer, Sagnac interferometer, and Fabry-Perot interferometer (FPI).

Figure 2.17 shows a simple setup of an MZI. The setup composed of a light source, 2 full mirrors, 2 beam splitters, and 2 photodetectors. The first beam splitter is placed in front of the laser light source making a 45^0 angle to the direction of the light and splits the light beam into two with two different paths. The light that reflects from the first beam splitter (sample light beam) follows the upper path and gets reflected from the mirror and reaches the second beam splitter. Half of the first light beam passes through the second beam splitter and reaches photodetector A, and the other half of the first beam gets reflected from the beam splitter and arrives photodetector B. The light that passes through the first beam splitter (reference light beam) follows the lower path and gets reflected from the second mirror and reaches the second beam splitter. Half of the second light beam transmits through the second beam splitter and reaches the photodetector B, and the other half of the second light beam gets reflected

from the beam splitter and reaches photodetector A. When there is no sample that is placed on one of the two different paths that the light follows, both first and second light beams travel exactly the same distance therefore no phase difference is formed or observed when they interfere with each other after the second beam splitter. When we place a sample on the upper path, for example, the speed of the light beam that must travel through the sample changes, and The two light beams are separated by a phase difference. The light intensity of the interference measured by the two photodetectors fluctuates according to the phase difference..

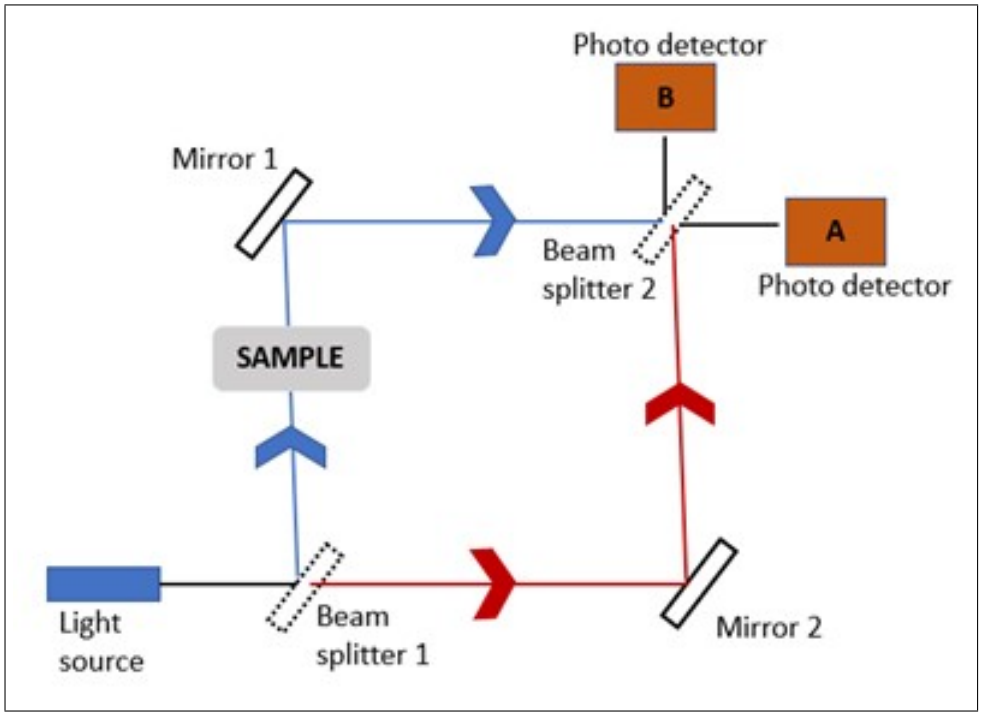

Figure 2.17 A basic setup of a Mach-Zender Interferometer.

Optical fiber sensors that use the MZI method work with the same principle. One reference path and one sensing path are formed using optical fibers and the path difference creates an intensity change in the light interference pattern. The ray of light in a fiber optic cable can be divided into two separate rays that travel through two separate optical fibers before being recombined into a single fiber at the end through fiber couplers. One fiber serves as the reference fiber and the other one is employed as the sensing fiber [81]. The change in the sensing fiber that is caused by the physical phenomenon (temperature, strain, humidity, etc.) that needs to be measured can be measured by the change in the interference pattern.

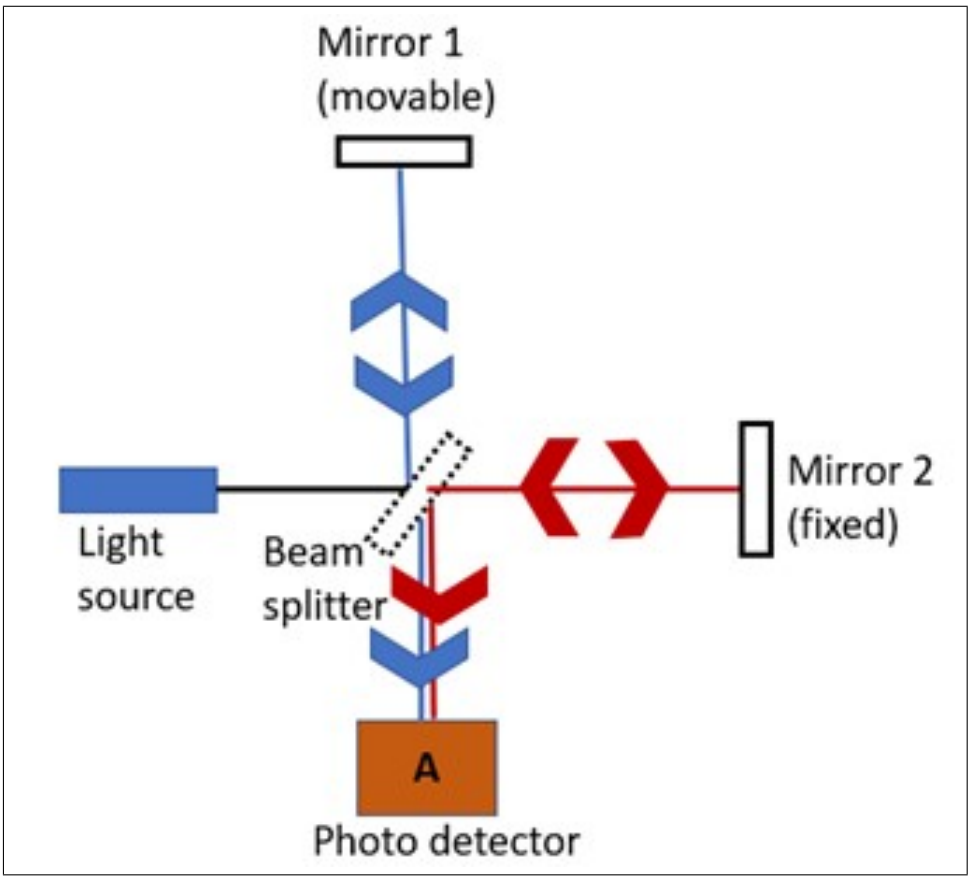

Figure 2.18 A basic setup of a Michelson Interferometer.

MZI and Michelson interferometers operate in very similar ways. A very basic setup for Michelson interferometer is given in figure 2.18. The setup consists of a light source, a beam splitter, 2 full mirrors (one of them is fixed and the other is movable), and finally a photodetector. The beam splitter is placed in front of the laser light source making a 45^0 angle to the direction of the light and splits the light beam into two with two different paths. The light that is reflected by the beam splitter arrives to mirror 1 and reflects to the beam splitter. after light goes through through the beam splitter, it travels to mirror 2 where it is reflected back into the beam splitter. Both light beams start from the same point, travel different paths, and meet again before reaching to the photodetector. The difference between the paths of two light beams determines the phase lag between them and hence determines the light intensity that is measured by the photodetector. Therefore, the distance that mirror 1 moves can be measured precisely with this setup. Michelson interferometer based optical fiber sensors works with the same principle. The light that travels in the optical fiber is

split into two using a fiber coupler and mirror surfaces are formed at the end of both fibers so that light beams are reflected and create an interference pattern [81].

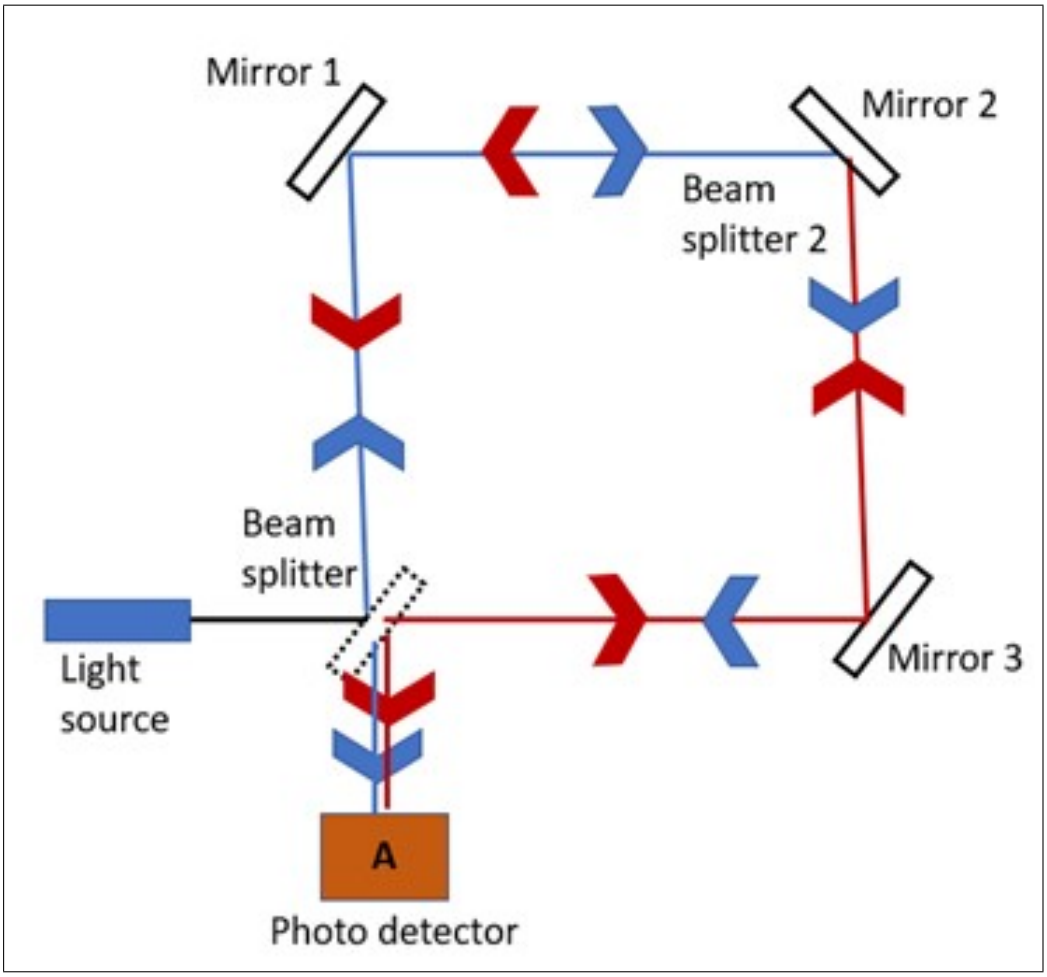

Figure 2.19 A basic setup of a Sagnac Interferometer.

The third type of interferometer is the Sagnac interferometer. A basic Sagnac interferometer setup is given in Figure 2.19. The setup consists of A light source, a beam splitter, three full mirrors, and a photodetector. The beam splitter is placed in front of the laser light source making a 45^0 angle to the direction of the light and splits the light beam into two. The separated light beams travel in the opposite direction to each other and they both rotate back to the beam splitter after getting reflected by 3 mirrors and they reach to the photodetector. When the interferometer is stationary both beams travel the same distance but if the interferometer starts to rotate with an angular frequency a phase difference is introduced between the two light beams. Using this phase difference and its effect on the interference of two beams fiber optic

gyroscopes that can be used for orientation detection can be designed using Sagnac interferometry [87].

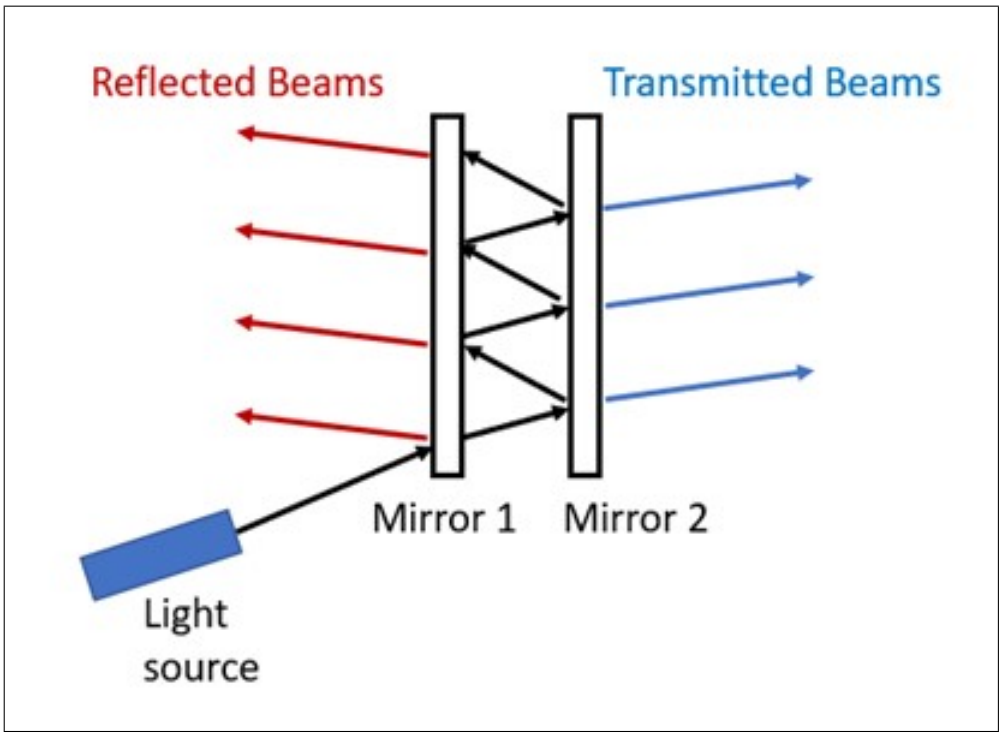

Figure 2.20 A basic setup of a Fabry-Perot Interferometer.

The fourth type of interferometer is called the Fabry-Perot interferometer. A basic setup for FPI is given in Figure 2.20. A basic FPI setup consists of a light source, two partially reflective mirror surfaces, and a photodetector. Two partially reflective mirror surfaces are placed parallel to each other. The light beam that reaches the mirror surfaces partially gets reflected and partially gets transmitted from both mirror surfaces. Therefore, Multiple light beams that travel different paths and hence with different phase values are formed at both sides of the mirror surfaces. both transmitted beams and reflected beams can form an interference and the path difference between different light beams is dependent on the distance between two mirror surfaces. Two partially reflective mirror surfaces turn a single beam into multiple beams that can form an interference pattern and this multiple-beam interference results in a high-resolution interference pattern.

2.4.3.3 Fabry-Perot interferometry based fiber optic sensors. Fabry-Perot interferometry-based fiber optic sensors are studied extensively in the literature because of; the simplicity of design and fabrication process of FPI sensors compared to other types of interferometric sensors, the capability of measuring different types of physical parameters (temperature, strain, pressure, humidity, acoustic and more) using and modifying only optical fibers, immunity to electromagnetic fields and other external noises and, capability to design high precision, high accuracy, and high-resolution sensors [88].

Two partially reflective mirror surfaces with a cavity between them is necessary to build a Fabry-Perot interferometer. The light intensity of interference of the reflected or transmitted light beams is dependent to the cavity length between the mirror surfaces. Therefore, if an external applied force can change the distance between two mirror surfaces it can also change the measured light intensity at a specific point on the interference pattern. The two types of FPI sensors with respect to the method of forming two mirror surfaces are namely, intrinsic FPI sensors and extrinsic FPI sensors [89],[90].

Extrinsic FPI force sensors commonly form the first partially reflective mirror surface using the end surface of the transmitting optical fiber (primary optical fiber) and the second mirror surface is placed outside of the primary fiber parallel to the first mirror surface forming a small cavity (commonly an air cavity) between them. The second mirror surface can be formed by the end surface of another optical fiber (secondary optical fiber), or a reflective thin film membrane. Two different simple design examples of an extrinsic FPI force sensors are given in figure 2.21. A primary fiber that transfers the light beam is placed and fixed inside of a capillary tube and the polished end face of the primary fiber can be used as the first mirror surface. A second optical fiber or a reflective thin membrane can be placed as the second mirror surface forming an air cavity which will act as a path difference between two reflected light beams. The reflected light beams form an interference pattern and when an external force is applied it changes the path that the secondary reflected light travels by moving the second mirror surface.

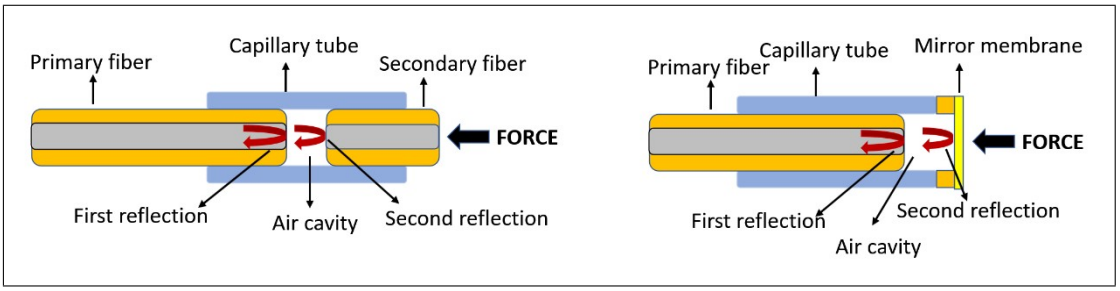

Figure 2.21 Extrinsic FPI force sensor design.

Bremer et. al. introduces a fiber optic temperature and pressure sensor design based on extrinsic FPI interferometry in their work [91]. They use a single mode optical fiber as their primary fiber and first partially reflective mirror surface and a silica glass fiber as their secondary mirror surface. They placed the two optical fibers into a glass capillary by fusion splicing leaving a cavity between them. Another design example of an extrinsic FPI sensor from the literature can be found in the study published by Liu et al [92]. In their work, Liu et al explains the design and fabrication steps of their low-frequency acoustic FPI sensor. They use a single-mode fiber as their primary fiber and first mirror surface and an Ultraviolet (UV) curable adhesive diaphragm as their secondary mirror surface. They form the UV adhesive diaphragm at the tip of a stainless-steel tube and place and fix the single-mode fiber inside the same tube leaving a cavity between the two mirror surfaces.

Intrinsic FPI sensors are designed by forming an internal Fabry-Perot cavity (the cavity that creates the path difference between the reflected light beams) unlike the extrinsic FPI sensors. That means the light beam doesn't travel outside the optical fiber to reach the secondary mirror surface. There are several methods to fabricate an intrinsic FPI sensor such as vacuum deposition, electron beam evaporation, sputtering, splicing different types of optical fibers, femtosecond laser machining, etc. [93]-[97]. Intrinsic FPI sensors are generally smaller and more sensitive compared to extrinsic ones, but extrinsic FPI sensors are less sensitive to temperature changes and have a higher signal-to-noise ratio. Zhang et al. use a femtosecond laser to form two internal partially reflective mirrors inside of a single-mode fiber and cascades this intrinsic FPI sensor with an additional extrinsic FPI sensor to measure temperature and pressure in

their study [97]. Another example of an intrinsic FPI sensor is described in the study published by Tsai et al. [89]. Tsai et al. use 2 different optical fibers with different core diameters and fuse them together by splicing. Therefore, they create 2 partially mirror surfaces that can reflect two different light beams to form an interference pattern.

Another type of fiber optic sensor that can be put into the intrinsic FPI sensor category with respect to its fabrication method is Fiber Brag Gratings (FBG) based fiber optic sensors. However, considering their working principle and popularity, FBG-type fiber optic sensors should be explained in their own section below.

2.4.3.4 Fiber Bragg gratings based fiber optic sensors. FBG-based sensors are commonly used and studied in several engineering areas such as civil engineering, mechanical engineering, medical engineering, and aerospace engineering to measure various physical properties like strain, pressure, temperature, humidity, refractive index, and so forth [98]. Fabrication of an FBG sensor takes advantage of a phenomenon called photosensitivity [99]. This phenomenon explains that exposure to ultraviolet (UV) radiation can change the fiber core's refractive index.

To form Bragg gratings in an optical fiber, UV light is shined onto a short part of an optical fiber passing through a phase mask. The UV light that passes through the phase mask forms an intense interference pattern on the optical fiber and the bright sections of this interference pattern forms mirror surfaces inside the fiber core by changing the refractive index of that specific area. This small section of optical fiber that contains a periodic modulation of refractive index and hence partially reflective mirror surfaces are called Bragg gratings [98].

When the change in the refractive index of Bragg gratings is periodic and constant the small section of the optical fiber that contains Bragg gratings reflects a specific wavelength back. This wavelength is called Bragg wavelength [100]. A change in physical parameters such as pressure change or temperature change around the Bragg gratings causes a shift in the Bragg wavelength. Therefore, a correlation can be formed

between the physical parameters and the shift in the Bragg wavelength.

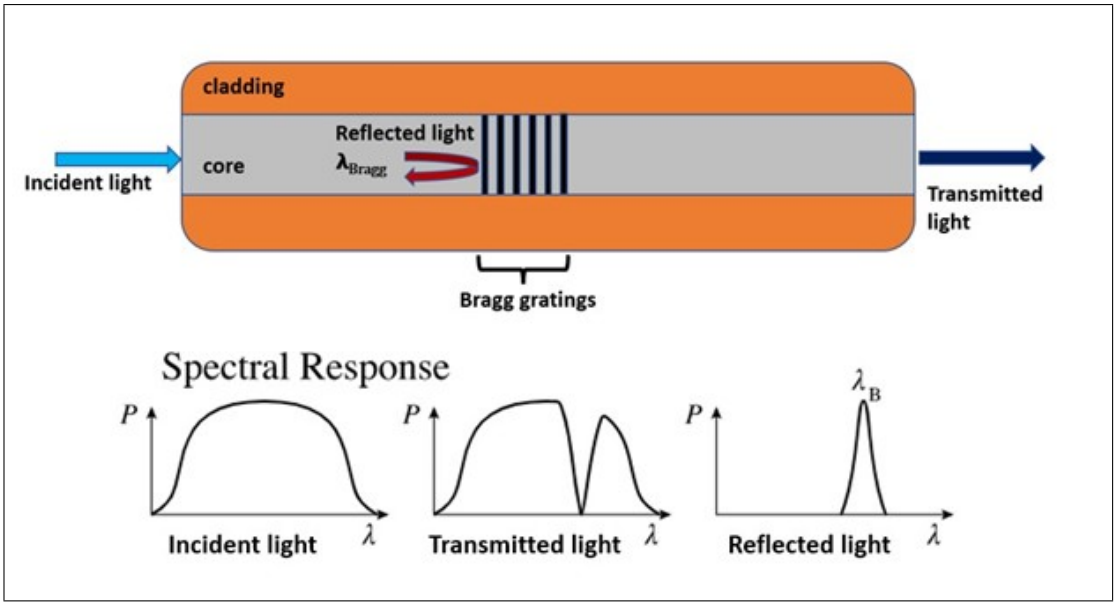

Figure 2.22 FBG-based sensor working principle.

Figure 2.22 shows the working principle of FBG-based sensors. Being biocompatible, chemically inert, immune to electromagnetic exposure, and having high sensitivity makes FBG sensors suitable for medical applications [101]. Mohanty et al. Used an FBG sensor concept for pressure measurements at the prosthetic knee joint in their study [102]. FBG sensors are used for physiological monitoring such as blood pressure [103], body temperature [104], heart rate [105], etc. Zhang et al. used FBG-based sensors to be used for measuring force and providing tissue characterization and tactile feedback during retinal microsurgery [106].

2.5 Interventional device tracking under MRI

The unmatched advantages of MRI as an imaging technique for interventional operations are given in section 1.3. MRI's ionizing radiation-free nature provides a safe environment for both patients and physicians. Its excellent soft tissue contrast can distinguish different tissue types like fat, muscle, tumorous, and healthy tissues. Multiplanar imaging capability can provide both 2D and 3D images of the target anatomy.

Sequences such as Gradient-echo (GRE) and balanced steady-state free precession (b-ssfp) can provide fast (real-time) imaging. Even with these important advantages MRI provides, for therapeutic or interventional diagnostic procedures, MRI still needs a lot of work to become the commonly used imaging modality..

One of the main disadvantages of MRI is that it's not safe to use conventional tools and technologies because of its high magnetic field environment. Even non-magnetic metallic interventional tools such as catheters or guidewires can cause safety hazards and tissue damage because of radio frequency (RF) induced heating. Another big disadvantage of MRI is the low conspicuity of non-magnetic, MR-compatible interventional tools under MRI. Therefore, using commercial interventional tools under MRI is not an option most of the time. There are different methods to increase the visibility of MR-safe interventional tools in the literature. One way to make device tracking possible under MRI is placing fiducial markers on interventional tools. The three most common types of fiducial markers namely active, passive and semi-active (resonant) markers and as a fourth method DC (direct current) controlled markers are explained with more detail in the following sections.

2.5.1 Passive markers

Passive markers take advantage of the intrinsic properties of the marker material to increase the device visibility by forming negative or positive contrast artifacts on the MR image. Because the magnetic properties of the marker material are different from the surrounding tissue a distinguishable contrast can be generated. Some advantages of passive markers can be given as they are easy and simple to design and implement on interventional devices, They don't require any external hardware or software to work under MRI, and RF-induced heating on passive markers is not a big safety problem as it is for active markers. Compared to other marker methodologies passive markers have some disadvantages too such as the marker artifacts are not as conspicuous as active markers, The marker artifact size can't be controlled or turned on and off when needed, marker performance is significantly affected by the orientation of the device

with respect to the main magnetic field (B_0) of the scanner.

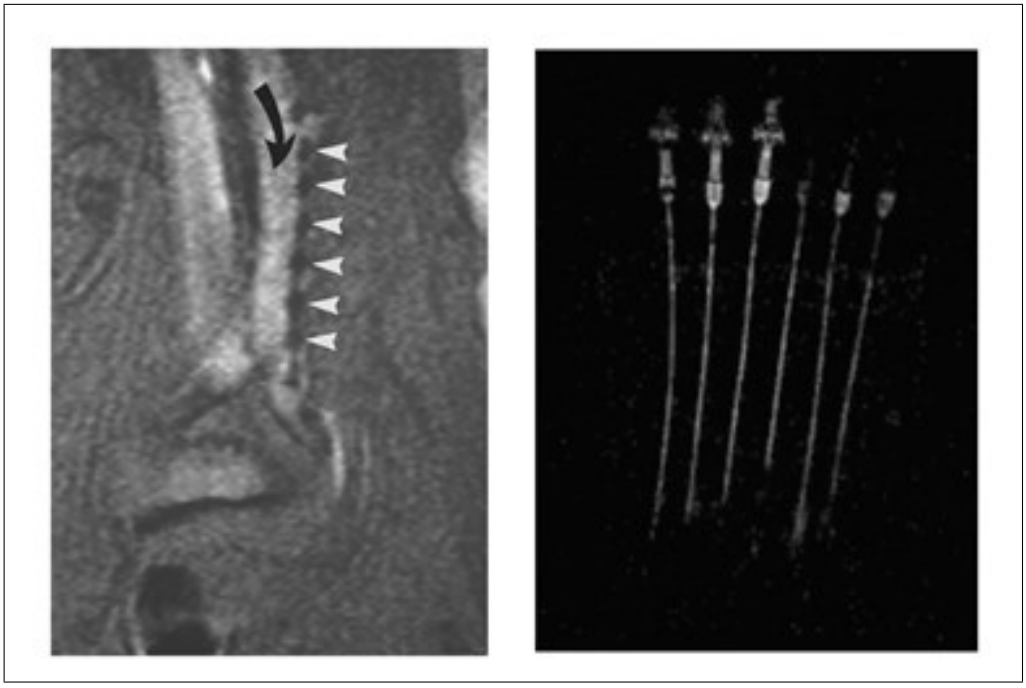

Figure 2.23 a. Negative contrast artifacts formed by platinum markers around a 5 Fr. catheter. b. Positive contrast artifacts formed by Gadolinium-filled catheters [110].

Negative contrast is generated by local inhomogeneities on the magnetic field resulting from ferromagnetic, ferrimagnetic, or paramagnetic marker materials that form a signal void or susceptibility artifacts on the image [107]. As an example, Manke et al. use platinum markers to create small signal voids (negative contrast) around a 5 Fr. catheter and increases the device visibility under MRI in their study as shown in Figure 2.23-a [108]. Basar et al. use nitinol and stainless-steel markers to show the susceptibility-based negative contrast artifacts' dependency on magnetic field strength and device orientation in their work as another example from the literature [109]. Passive markers can generate positive contrast using the T_1 shortening effect of certain paramagnetic materials. A common T_1 shortening agent that is used for device tracking under MRI is gadolinium. In their study, Omary et al. test the feasibility of real-time MR-guided catheter tracking using gadolinium-filled catheters as shown in Figure 2.23-b [110].

2.5.2 Active markers

Active markers that are placed on interventional devices act as small receive coils or receive antennas that collect the MR signal from a small area around the marker coil when the markers are tuned to the Larmor frequency of the scanner. This signal carries the spatial location information of the active marker along the 3 axes with respect to the gradient fields of the scanner, and it is transferred to the scanner from the scanner's one of the separate receive channels. MRI signal that is collected by the active marker's receive coils can be used for fast and accurate device tracking. The image of the active markers can be overlayed onto anatomical images using an external software and marker images can be controlled, colorized, and turned on and off if desired. Although active markers are more difficult to design compared to passive ones, they provide higher conspicuity. The biggest advantage of active device tracking is that it can provide colored and controllable high conspicuity both for certain spots (like the tip of the device) on the interventional device or for the whole device shaft with high accuracy. Some disadvantages of active device tracking are: It needs device-specific hardware to tune the coil markers to the Larmor frequency; the interventional device needs to be connected to the scanner which can limit the physician's movements; it requires external software to overlay device signal onto MRI image and finally extra steps need to be taken to decrease the RF-induced heating on the interventional device which can reach to dangerous levels for the patients.

Yildirim et al. designed a custom 20-Gauge needle prototype that contains active receive coil markers that increase the conspicuity of the invisible nitinol needle under MRI [111]. The same group designed a custom guidewire as a receive antenna so that it can be visualized as an active device under MRI [112]. Figure 2.24-a shows the image that was formed using the MR signal received by only the 3 active coil markers on the needle prototype and figure 2.24-b shows the colorized marker signal overlayed on the MR image of the anatomy during an in-vivo animal experiment.

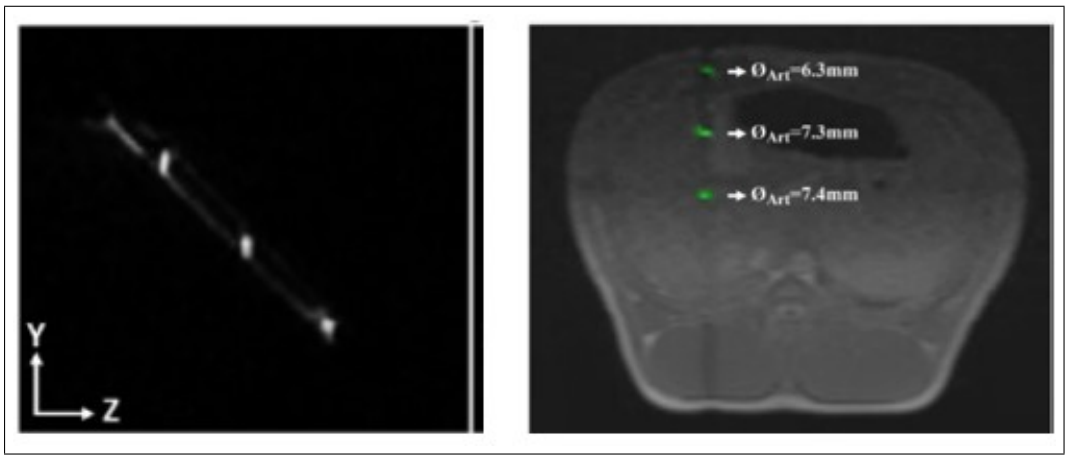

Figure 2.24 a. Needle prototype image with 3 active coil markers received from a separate receive channel b. Active needle image is colored and overlaid on the anatomical image during an animal experiment [111].

2.5.3 Semi-active (resonant) markers

Semi-active markers that are placed on interventional devices take advantage of the induced electromagnetic fields on them caused by the RF coils of the scanner. Resonant markers are composed of capacitive (C) and inductive (L) components and using these components they can resonate with the Larmor frequency of the scanner which is determined by the magnetic strength of the scanner. When the semi-active markers are designed so that they resonate with the transmit RF coils, the induced current on the markers form a local external magnetic field that can excite the proton spins further in its immediate vicinity. This further excitement causes flip angle amplifications around the marker, and it results in a higher signal intensity or a positive contrast.

To be able to create a sufficiently high contrast so that it can be tracked during a procedure, the LC circuit that composes the semi-active marker needs to be tuned to the Larmor frequency of the scanner. Therefore, when designing a semi-active marker capacitor and inductor values should be chosen accordingly. The relationship between the resonant frequency, inductance and capacitance of a circuit is given in Eq. 2.3. f_R is the resonant frequency, w_0 is the angular frequency, L is the inductance of the circuit and C is the capacitance of the circuit.

$$f_R = w_0/2\pi = 1/(2\pi \cdot \sqrt{LC}) \tag{2.3}$$

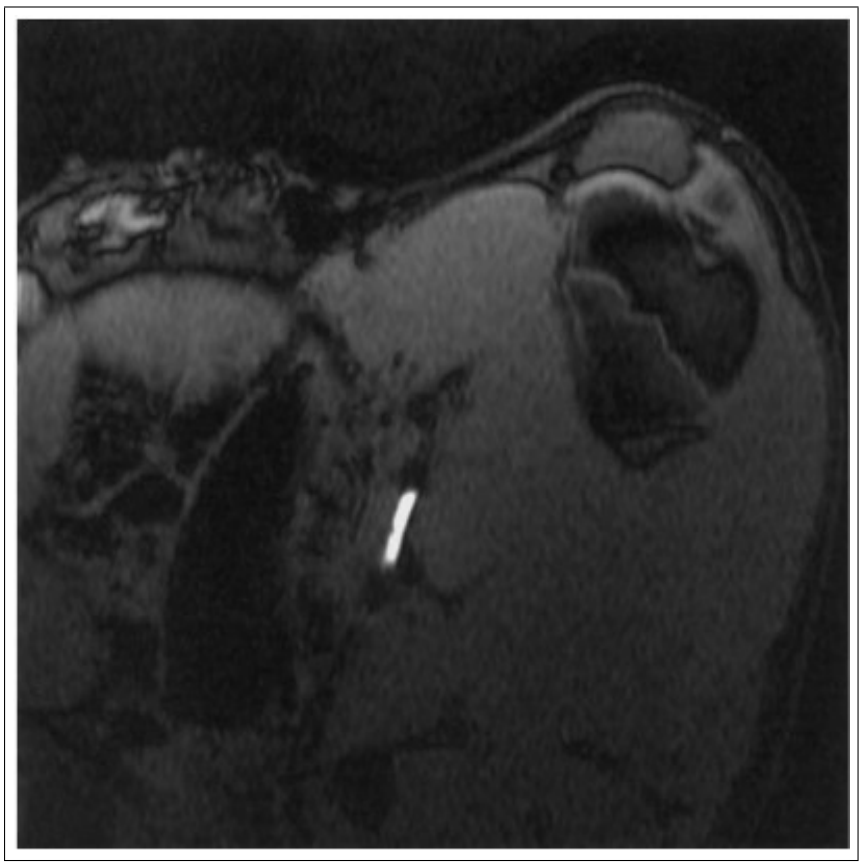

Figure 2.25 in-vivo MRI image of a resonant marker solenoidal stent.

Resonant markers are easier to design when compared to active markers and they provide a wireless accurate device location under MRI. On the other hand, the conspicuity of resonant markers depends on the contrast difference that is created by the flip angle amplification caused by the markers. Therefore, the positive contrast created by the markers will work better when a low flip angle sequence is used [113]. The RF-induced current on the markers depends on the orientation of the marker with respect to the B_1 field and hence the conspicuity of the markers also depends on the device orientation under MRI [114]. Because they need to be tuned to the Larmor frequency to work the same marker can't be used under scanners with different magnetic strengths [115]. In Figure 2.25, a solenoidal stent that is designed to act as a resonant marker is placed into the right iliac artery of a pig in an in-vivo experiment

performed by Quick et. al. [116].

2.5.4 Direct current (DC) controlled markers

The most common 3 device tracking methods for interventional MRI are explained in the previous sections. Apart from active, passive, and resonant markers, another method is introduced by Glowinski et al. [117]. In their work an electrically conductive wire is wounded around a catheter and by applying a constant direct current to the wire a negative contrast is formed around the catheter when they used a GRE sequence to image the catheter under MRI as shown in figure 2.26. When a current is applied to a conductive wire, a resulting electromagnetic field is generated around it that depends on the amplitude of the applied current and distance from the wire. The additional magnetic field created by the applied direct current to the wire disrupts the homogeneity of the main magnetic field B_0 and hence, it results in low signal, and negative contrast artifacts around the interventional device.

This device tracking method for interventional MRI showed promise with the advantages given below [117]-[119]:

1. Easy design and implementation
2. Ability to control the marker artifact sizes by controlling the applied current amplitude.
3. Ability to turn the artifacts on and off when desired.
4. Independent from the magnetic field strength of the scanner
5. Doesn't need to be tuned to the Larmor frequency.
6. Doesn't need a separate receive channel and external software.
7. Doesn't need device-specific hardware.

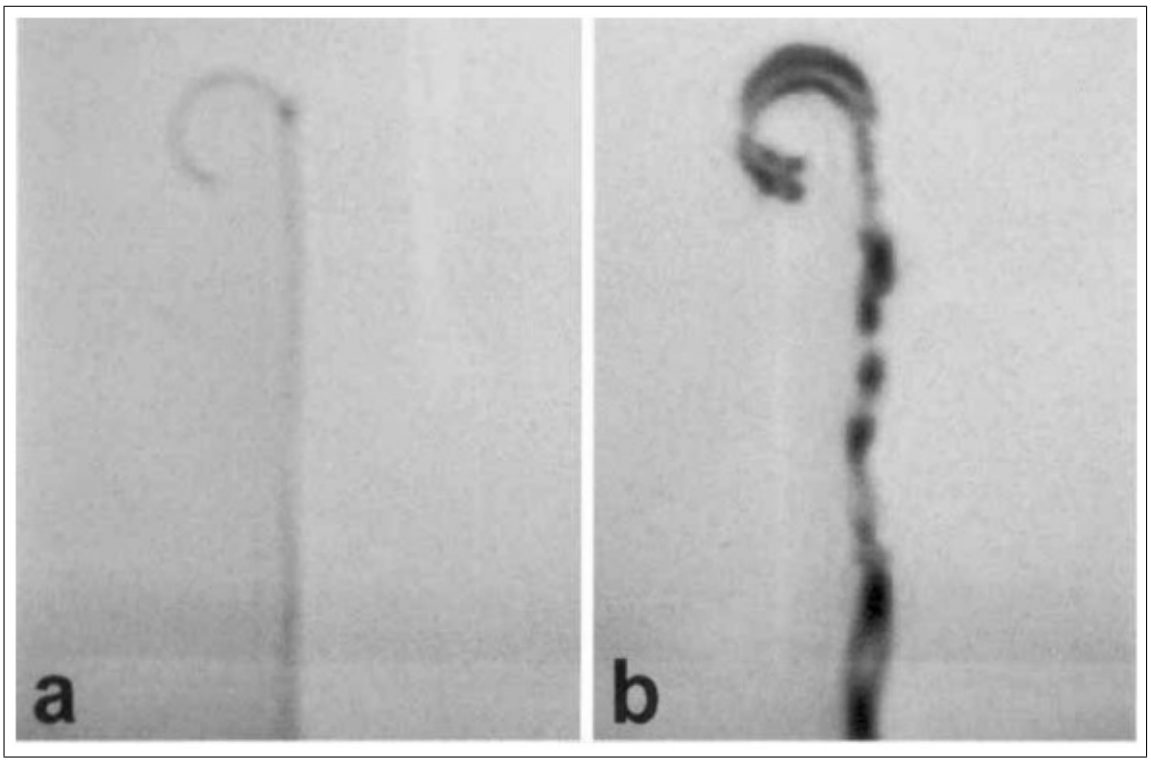

Figure 2.26 In-vitro images of conductive wire wounded catheter. **a.** no current is applied to the wire **b.** 150 mA Direct current is applied to the wire.

The advantages of DC-controlled markers could be very beneficial for the improvement of the interventional MRI field, but this method has still some place for improvement. With this method, the conspicuity of the devices can't be increased as much compared to active markers without image postprocessing. Although it doesn't need device-specific tuning hardware, the interventional device still needs to be connected to a current supplying hardware. Lastly, the DC-applied device tracking is pulse sequence dependent. Applying a continuous direct current to conductive markers can form artifacts with sufficient conspicuity when a GRE sequence is used but it doesn't work as well with sequences that have more immunity to constant inhomogeneities than GRE such as Spin-echo (SE) or b-SSFP [118],[119]. Instead of using a constant DC, Eibofner et al. used transient DC in SE and b-SSFP sequences to form more conspicuous artifacts in their studies by triggering the direct current supply with respect to the pulse sequence [118,119]. Therefore, although being dependent on the pulse sequence, this method still can be used with various sequences by adjusting the applied current with respect to the sequence.

2.6 Pulse sequences for interventional MRI

Requirements of diagnostic imaging by MRI and performing guided interventions using MRI are different. Providing near real-time rapid imaging is very important for interventional procedures when inserting the interventional device into the anatomy and advancing and guiding it toward the target area. A contrast difference with a sufficient SNR between the target tissue and the interventional device should be provided. Other than rapid imaging with sufficient SNR in some procedures such as MR-guided ablations or biopsies, higher resolution and a distinguishable contrast difference between the healthy tissue and tumorous tissue might be required. All of these requirements can be provided using different pulse sequences with MRI but there is not a single pulse sequence that can meet all the requirements. Three of the pulse sequences that are commonly used in interventional MRI GRE, b-ssfp, and Turbo Spin-echo (TSE) are explained more in the following sections.

2.6.1 Gradient-echo (GRE) imaging

Gradient-echo sequence is suitable imaging technology for interventional procedures because of its rapid imaging capability. A sample GRE sequence pulse diagram is given in figure 2.27.

GRE sequence doesn't require an RF pulse that would cause a 90^0 flip. It can provide good tissue contrast images using lower flip angles therefore, the proton spins can return to their original longitudinal magnetizations much faster by using lower flip angle RF pulses. After the RF pulse, first a negative (dephasing) and following that a positive (rephasing) frequency encoding gradient is applied. The negative frequency gradient puts the spins out of phase with each other and the positive frequency gradient puts them back in phase and the signal is obtained. Using a T2* relaxation (transverse relaxation time resulting from dephasing frequency encoding gradient) instead of T2 relaxation (transverse relaxation time without any external inhomogeneity) is another factor that makes GRE a rapid imaging sequence.

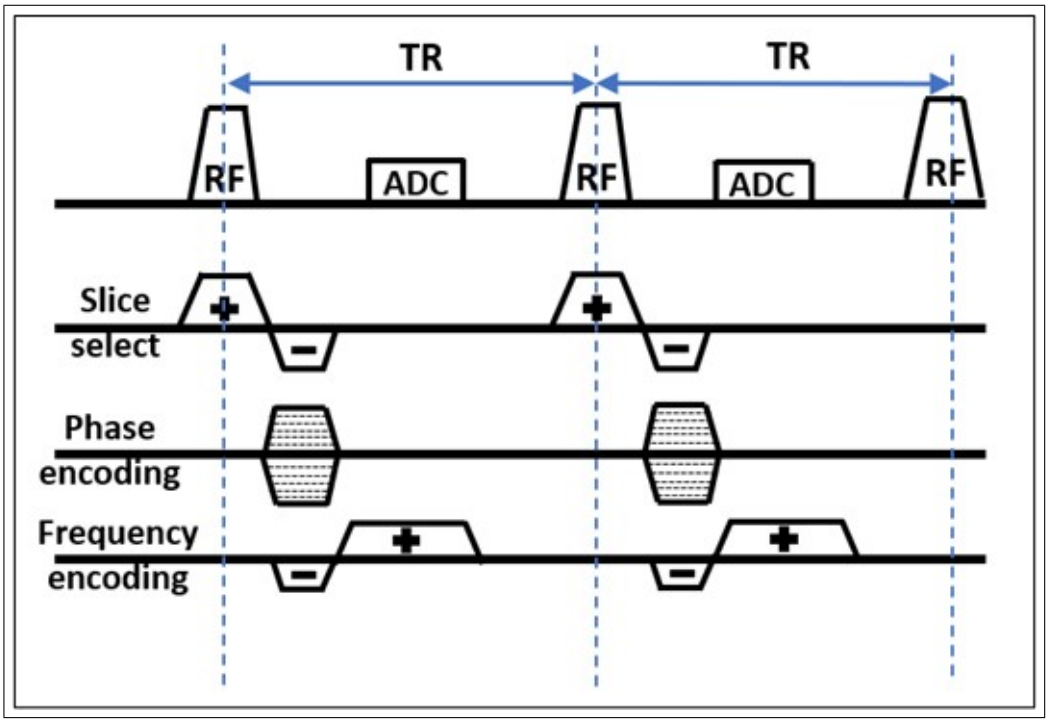

Figure 2.27 Gradient-echo pulse sequence diagram.

2.6.2 Balanced steady-state free precession (b-SSFP) imaging

Balanced steady-state free precession sequence is actually another type of Gradient-echo sequence. In GRE imaging an RF pulse is utilized to flip the proton spins every repetition time (TR). This RF pulse flips the proton spins to a certain angle. When the RF pulse stops proton spins start a relaxation period and dephasing between the proton spins occurs depending on the spatial location of the protons and the gradient fields that are applied to the protons. Longitudinal and transversal components of the net magnetization of the proton spin during relaxation and the relaxation times such as T1 (relaxation time for the spin vector to get back to its original condition) and T2 (relaxation time for an axial spin vector to get back to its original condition) are used for creating the MR image. When the TR values are kept short enough so that consecutive RF pulses hit the proton spins before they could return to their original magnetization state the net magnetization of the spins can be kept in a steady state and this is called steady-state free precession. This phenomenon is first introduced by Carr [120]. Balanced steady-state free precession uses the same phenomenon but it keeps the net dephasing effect of gradient fields in all 3 axes 0 within each TR. A

sample pulse diagram of a b-SSFP sequence is given in Figure 2.28.

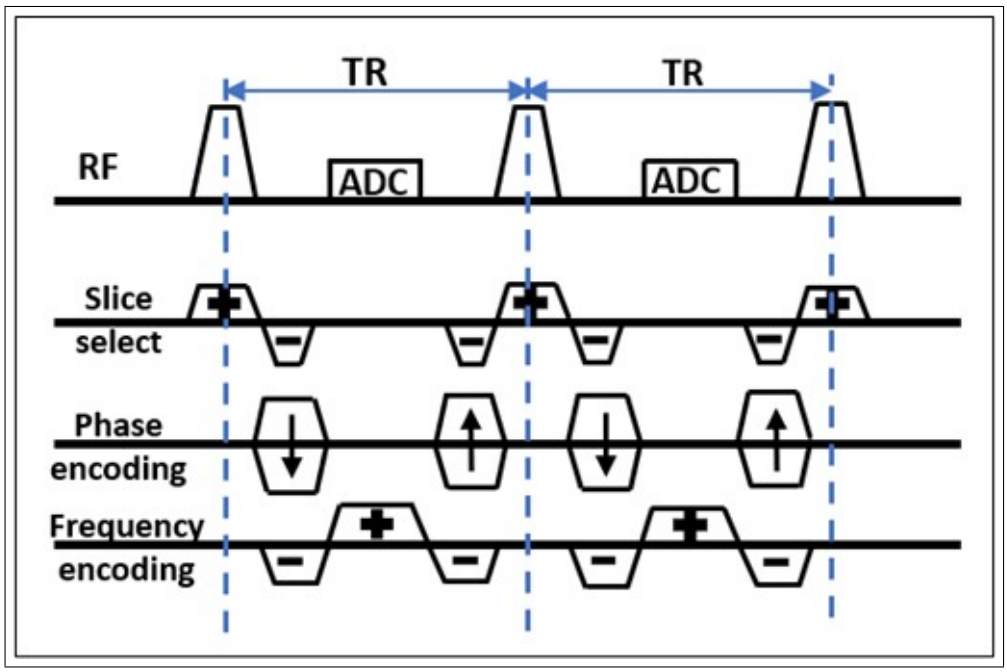

Figure 2.28 Balanced steady-state free precession pulse sequence diagram.

As can be seen in Figure 2.28, all three gradients that are applied to the proton spins are applied again in the opposite direction so that the net effect adds up to 0 in one TR. Using these refocusing gradients provides rapid imaging and also because gradients refocus in all 3 axes within each TR. b-SSFP sequence provides images that are more immune to motion artifacts and constant inhomogeneities in the magnetic field. This immunity makes b-SSFP sequence suitable for cardiac interventions.

2.6.3 Turbo (fast) spin-echo (TSE) imaging

When an RF pulse is supplied to the proton spins, the spins are flipped, resulting in net magnetization in the transverse plane. As the spins dephase, the net magnetism in the transverse plane diminishes. This phenomenon is called free induction decay (FID). If another RF pulse is applied following the first one, de-phased spins can get in phase again and a spin-echo is produced. In a conventional spin echo sequence, a 180^0 RF pulse is used following a 90^0 RF pulse in 1 TR. The 180^0 second RF pulse is called the refocusing pulse. Repetition times in the Spin-echo sequences are much

longer than in the Gradient-echo sequences. Therefore, the SE sequence is much slower compared to GRE-based sequences.

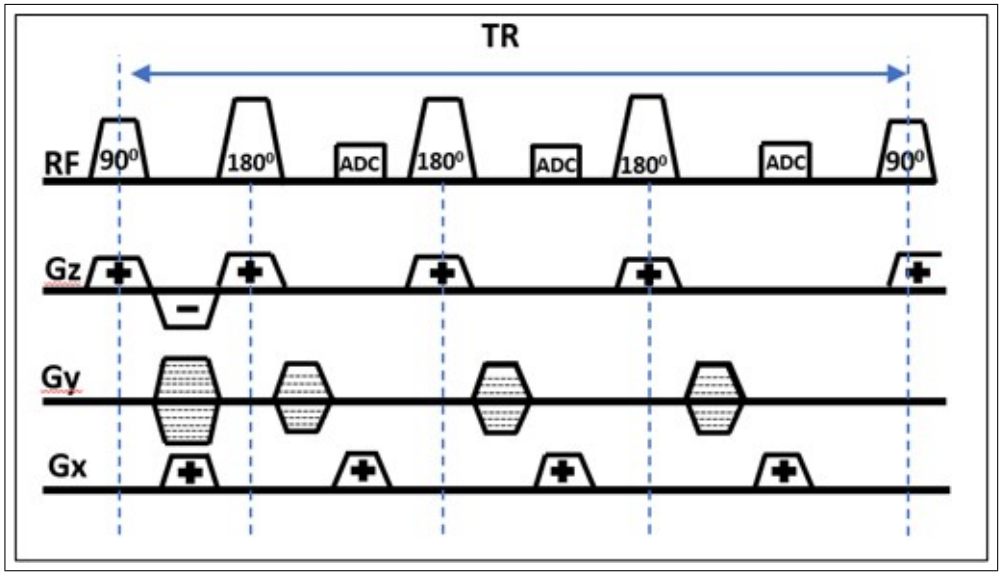

Figure 2.29 Turbo spin-echo sequence diagram.

To speed up the spin-echo sequence Hennig et al introduced Rapid Acquisition with Relaxation Enhancement (RARE) technique [121] which is the technique that describes the Turbo spin-echo sequence. A sample pulse diagram of a TSE sequence is given in Figure 2.29. As can be seen in the figure, instead of waiting for the next TR, multiple refocusing (180^0) RF pulses can be applied after a single 90^0 RF pulse within 1 TR. By applying a different phase encoding gradient for every refocusing RF pulse, instead of acquiring only 1 line from the image, multiple lines can be acquired in 1 TR. Although the TSE sequence is still slow compared to GRE-based sequences, TSE can provide relatively fast and higher-resolution images.

2.7 MRI safety

MRI uses a static strong main magnetic field (B0) and dynamic rapidly changing electromagnetic fields such as RF pulses that are used for flipping the proton spins and gradient fields that accomplish the spatial encoding inside the scanner bore, for creating anatomical images. To avoid potential safety risks that can be caused by the strong

magnetic fields of MRI for both diagnostic imaging or interventional procedures in the MRI environment, every tool or object should be carefully inspected and confirmed that they are either MR-safe or MR-conditional before entering the scanner room.

Items that are labeled as MR-safe don't create any safety hazards and can safely be in the MR environment and don't have any scanning restrictions. Items that are labeled as MR conditional can only be in the MR environment under specific conditions. These conditions may restrict the use of the object depending on the object's distance from the scanner bore, the static magnetic field of the scanner, specific absorption rate (SAR), gradient field levels, etc. MR-conditional devices can't be used in the MRI environment unless these conditions are met. Items that are labeled as MR-unsafe can't be in the MR environment under any conditions.

This chapter will focus on MRI safety of interventional MRI equipment and safety tests that needs to be performed on an interventional device according to the safety standards provided by the American Society for Testing and Materials (ASTM). In the next 2 sections, magnetically induced displacement force testing protocols on interventional devices and RF-induced heating experiment protocols on electrically conductive interventional devices are explained in detail according to ASTM F2052-15 [122] and ASTM F2182-19e2 [123] standards respectively.

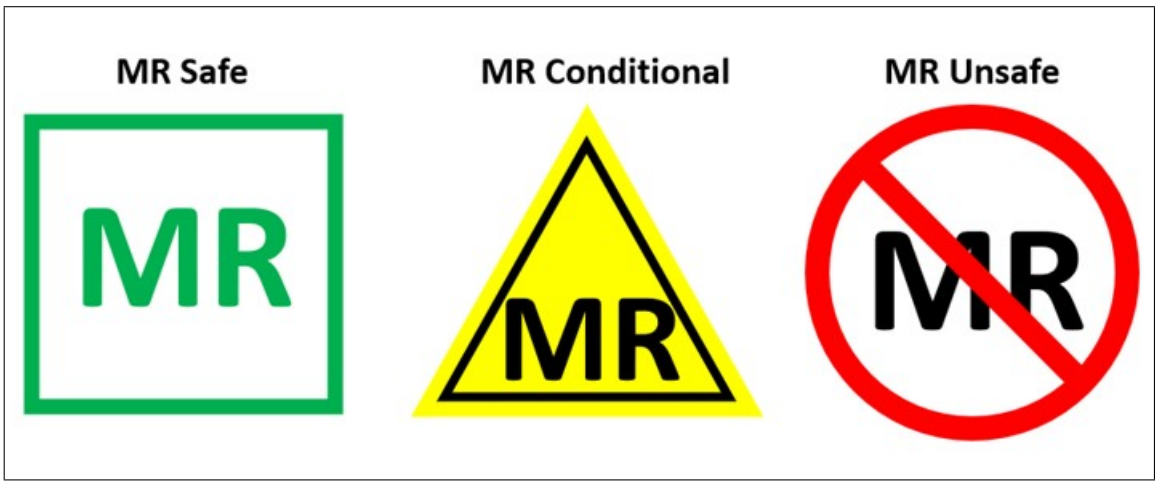

Figure 2.30 MRI safety labels.

2.7.1 Magnetically induced displacement force and torque measurements for interventional device safety under MRI

One of the reasons that many commercially available interventional devices that can be used in X-ray, CT, ultrasound-guided interventions are not safe to use in MRI environment is that they contain ferromagnetic materials. The strong static magnetic field (B_0) of the scanner may induce a force and torque onto the interventional device and may cause safety problems for both the patient and the physician. In this section experimental procedures for magnetically induced displacement force and torque measurements are explained in reference to ASTM 2052-15 [122] and ASTMF2213-17 [124] standards.

The ASTM2052-15 standard claims that the magnetically induced force on a device should be less than the force applied to the device by gravity or the weight of the device to minimize the risks that can be caused by the magnetically induced force. The experiment and the test fixture described in the standard are given in Figure 2.31. The test fixture should be non-magnetic and strong enough to carry the test sample and should contain a protractor to measure the deflection angle of the interventional device when placed in the magnetic environment. The fixture should be placed at the location where the static magnetic field gradient is the strongest and the interventional device should be suspended by a string from the fixture. The deflection angle that is resulted by the magnetically induced force on the interventional device should be recorded. If the angle is less than 45^0, that means the magnetically induced force is less than the weight of the device and it doesn't cause any safety hazards concerning the magnetically induced force.

Similar to magnetically induced displacement force, magnetically induced torque on the interventional device is compared to the equivalent torque applied by the gravitational force to test the safety of the interventional device according to the ASTM 2213-17 standard.

Figure 2.32 shows the test apparatus given in the standard. The non-magnetic

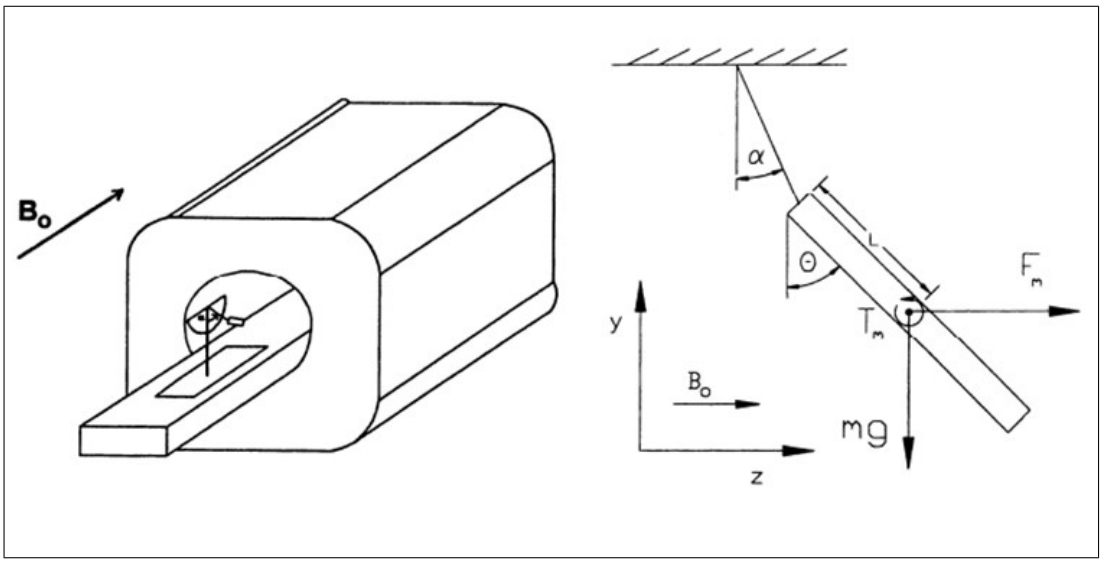

Figure 2.31 Test fixture for Magnetically induced force measurement [122].

test fixture should be placed where the static magnetic field of the scanner is uniform (middle of the scanner bore). The torque that is induced by the interventional device will try to align the long axis of the device with the main magnetic field of the scanner. The magnetically induced torque is calculated by multiplying the deflection angle measured on the test fixture and the spring constant (torsional spring). The gravitational torque induced on the interventional device is calculated by multiplying the weight and the longest dimension of the device.

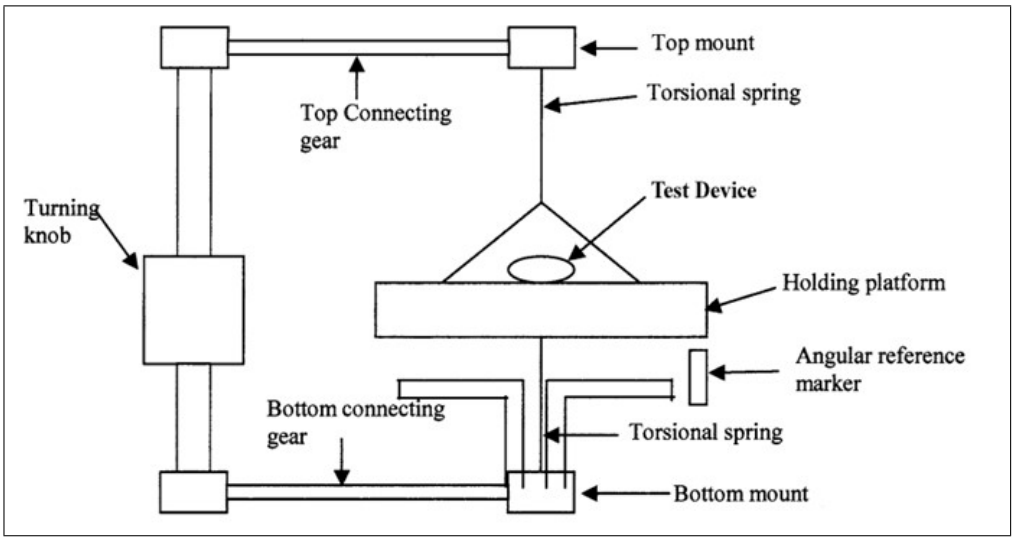

Figure 2.32 Test fixture for Magnetically induced force measurement [124].

2.7.2 RF-induced heating measurements for interventional device safety under MRI

Not containing magnetic materials and not being affected by the static magnetic field of MRI doesn't ensure the safety of an interventional device. The dynamically changing electromagnetic fields (RF pulses and gradient fields) that are used during a scan can increase the temperature of electrically conductive materials to dangerous levels by inducing an alternating current on them. There are many parameters that can affect the level of heating induced on the interventional device such as the length and the structure of the device, static and dynamic field strengths of the scanner, the spatial location of the device under MRI, specific absorption rate (SAR) and so on. In this section experimental procedures of RF-induced heating measurements for interventional devices are explained briefly in reference to ASTM F2182-19e2 [123].

The ASTM standard provides a recipe to prepare a gel phantom, to place the interventional device in it during the RF-induced heating experiments, that mimics the electrical load of an average human body (conductivity: 0.47 +/- 10% S/m, permittivity: 80 +/-20). The local background SAR is not the same everywhere inside the phantom therefore, the location of the interventional device inside the gel phantom should be chosen at a point where the local background SAR is known, and is high enough to generate a temperature change. The interventional device can be placed in a location in the gel phantom where the SAR is maximum so that the maximum temperature rise can be recorded. The standard provides an electric field and SAR distribution map in the gel phantom for 1.5 T and 3 T MRI (figure 2.33). To avoid RF coupling the device should also be placed at least 2 cm away from the surface, bottom or the walls of the phantom container.

3 temperature probes should be placed on the interventional device at points where the highest temperature change is expected (hot spots of the interventional device) to record the temperature changes during the experiments. Another temperature probe should be placed on a 10 cm titanium alloy far from the device under test to record a reference temperature to provide repeatability to the test during the experi-

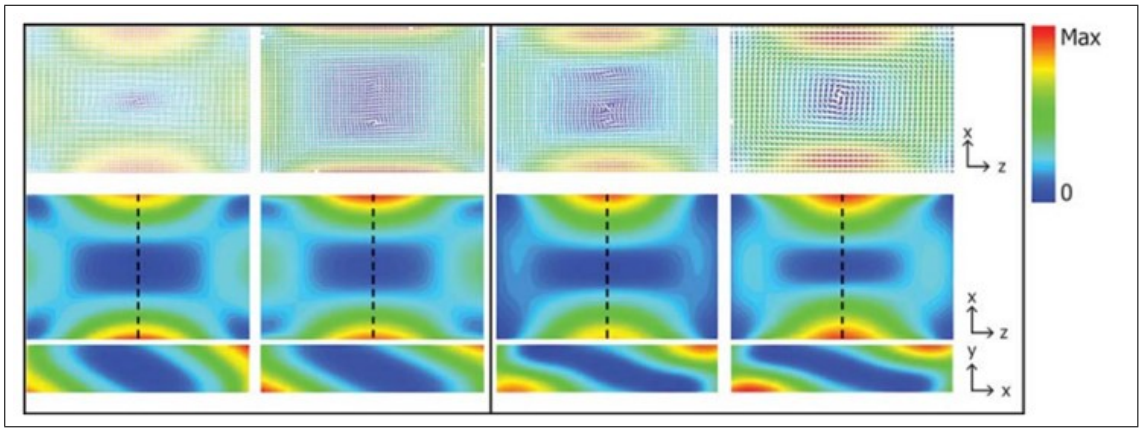

Figure 2.33 Simulated electric field distribution (top) and SAR distribution (middle and bottom) in the gel phantom for 1.5T on the left and 3T on the right [123].

ments.

Figure 2.34 shows an example experiment setup showing the device under test and temperature probe locations. The temperature should be recorded from all 4 probes at the same time. Recording should start at least 30 seconds before the RF exposure starts and at least 2 minutes after the exposure ends to show that there is no other source of heating. The temperature rise should be recorded for 15 minutes during the scan (RF exposure). To eliminate the effect of other parameters from the temperature recordings, all of the recordings should be normalized to a certain background SAR value (1W/kg).

The background SAR value of the interventional device location in the gel phantom can be measured by placing the 10cm titanium rod that contains a temperature probe at the exact same location where the interventional device was placed before. The temperature should be recorded for 6 minutes while the same RF exposure and the same scan parameters are used as in previous experiments. Local background SAR then can be calculated by dividing the temperature change after 6 minutes to 1.30 for 1.5 T and 1.45 for 3 T scanners.

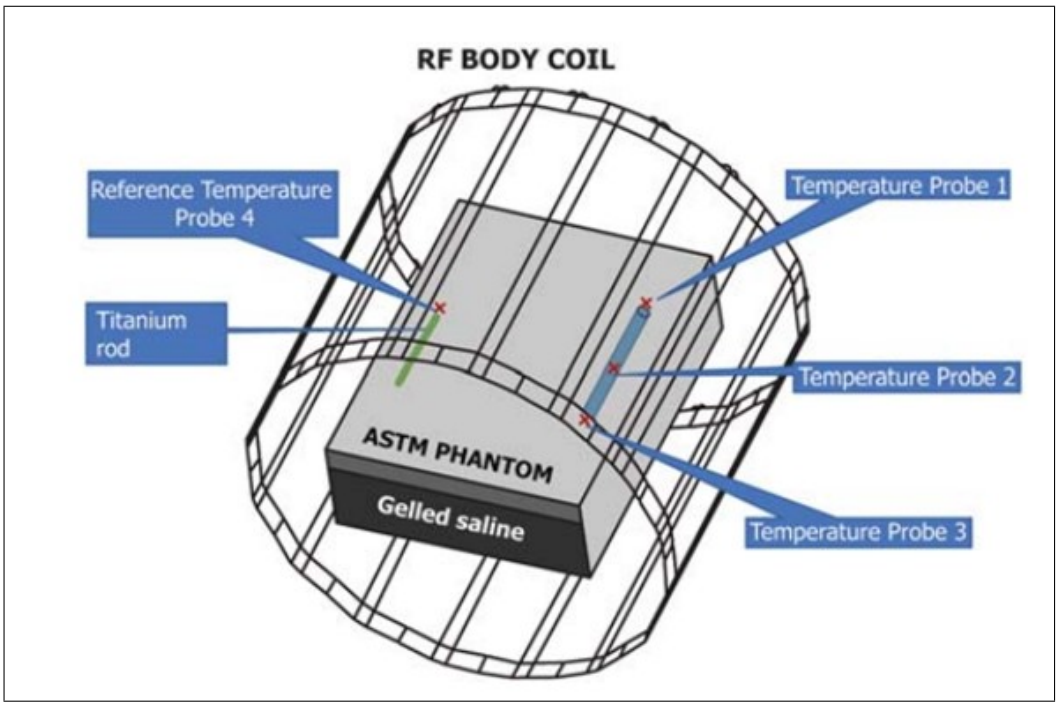

Figure 2.34 RF induced heating test setup [123].

2.8 Thesis objectives

The aim of this thesis is to develop novel technologies and devices that can be used for MR-guided biopsies. 3 main objectives of this study are: First, design a small and compact fiber optic force sensor that could be implemented at the tip of a biopsy needle that can give the physician tactile feedback and distinguish different tissue types as it advances inside the anatomy; second, developing a device tracking method using current controlled conductive ink printed markers to increase the visibility of MR-safe interventional devices; and third, designing an MR-compatible and visible needle prototype and a current supply circuit that could work in the MR environment and test its performance and safety with in-vitro and in-vivo experiments.

Although Interventional MRI is a powerful technology that combines the advantages of minimally invasive procedures with the superior imaging capabilities of MRI, There is still much room for development in this area as it is explained with more detail in the background chapter. The 3 main objectives of this study are explained briefly in the following sections.

2.8.1 Design and implementation of fiber optic force sensor

In our prior work, we proposed a fiber optic force sensor based on Fabry-Perot interferometry (FPI) that can measure forces that reach 13 Newtons (N) with a resolution of 0.1 N. In this thesis, an improved version of the fiber optic force sensor was designed and implemented into an 18-gauge biopsy needle. The range of the force sensor is improved from 13 N to 20 N and the resolution of the sensor is improved from 0.1 N to 0.03 N. The sensor's performance was tested with benchtop experiments and in-vitro experiments under MRI using a prostate phantom that contains Tumor mimicking lesions. The sensor's capability to distinguish different tissue types is tested via further benchtop experiments using different tissue types such as chicken breast, meat, or bovine fat tissues. It was shown that the sensor-implemented biopsy needle is capable of measuring the applied axial forces to the needle tip accurately and distinguishing different tissue types while needle insertion.

2.8.2 Quantitative analysis of current controlled tracking markers using 3 different sequences

Using the 4-axis conductive ink printer system that was designed by our group previously, solenoid coil markers were designed and printed on heat-shrink tubes using conductive ink to be placed on interventional devices for device tracking during MR-guided interventions. The heat-shrink tubes that contain solenoid markers were placed on an MR-safe interventional device mimicking test samples and the markers made visible in MR images via generating external local magnetic fields by applying current to the markers using GRE, b-SSFP and TSE sequences. The performance of the markers was tested under 0.55 T and 1.5 T MRI and, an elaborate analysis of current types (AC/DC) and parameters (amplitude, frequency) that would result in the most conspicuous marker artifacts were determined via in-vitro experiments under 0.55 T MRI for all of the 3 sequences. The capability of the introduced device tracking method to make MR-safe custom or commercial interventional tools visible and trackable under MRI was tested with further in-vitro experiments.

2.8.3 Custom MR-compatible needle prototype and current supply circuit design

A custom MR-compatible nitinol needle prototype was designed, and conductive ink printed tracking markers were implemented on the needle prototype. A signal generator current supply circuit that could work in the MR environment without disrupting the MR image or causing any safety problems was designed next. The performance of the current supply circuit and the visibility performance of the needle were tested under 0.55 T and 1.5 T MRI while using all 3 aforementioned sequences via in-vitro experiments. RF-induced heating tests to ensure the safety of the needle were performed under 0.55 T. Finally, an animal experiment was performed to test the visibility of the needle in-vivo under 0.55 T MRI using b-SSFP sequence.

2.9 Thesis outline

In Chapter 1 a short introduction and motivation of this thesis study is given. In Chapter 2 background information and a literature review about image-guided minimally invasive interventions, working principles of MRI, MRI-guided biopsy procedures, the importance of needle tip force feedback, conventional electrical and fiber optic force sensors, and fiber optic interferometry types, conventional device tracking technologies for interventional MRI and device tracking by DC applied markers, Pulse sequences for interventional MRI and MR safety concerning interventional devices are explained.

In Chapter 3, Fabry-Perot interferometry-based fiber optic sensor with enhanced force range and resolution for needle tip force feedback is introduced. Design and fabrication steps are explained. The performance of the sensor is shown in the experiment results. In Chapter 4 conductive ink printed marker design is introduced and quantitative analysis is performed about the applied current type and parameters that would result in high conspicuity under MRI for GRE, b-SSFP, and TSE sequences. The performance of the markers is shown with the in-vitro experiment results. In Chapter 5 the implementation of conductive ink printed markers to a custom-designed nitinol

needle prototype and the design of a current supply circuit that could work in the MR environment are described. The performance of both the needle and the current supply circuit is shown via in-vitro and in-vivo experiments.

In chapter 6 an overall general conclusion, discussion and future work are discussed.

3. OPTICAL FORCE SENSOR WITH ENHANCED RESOLUTION FOR MRI-GUIDED BIOPSY

3.1 Introduction

With benefits including reduced postoperative discomfort, recovery time, infection risk, and total cost of medical care, image-guided minimally invasive treatments are growing in popularity over traditional open surgical approaches [125]-[126]. Due to MRI's excellent soft tissue contrast, 3D anatomical imaging capability, and radiation-free mechanism [127]-[129], performing minimally invasive procedures under this technology improves the overall operation process. However, a physician's skills and experience play an important role in the success of the operation [130]. Especially, handling interventional medical devices, such as biopsy needles, professionally during minimally invasive operations can take many years of practice. Applying improper force to the needles during minimally invasive procedures may cause flawed operations, necrosis, infection, and scarring [131].

In order to manage the targeting, guiding, and manipulation of the biopsy needle, it is beneficial to include a small profile force sensor at the distal end of a needle during MRI-assisted biopsy procedures [132]. This results in a safer and more precise biopsy procedure. Due to its dielectric nature, chemical inertness, and nontoxicity [86], Fabry-Perot Interferometry (FPI) based fiber optic sensors are safe for clinical usage, MRI compatible, and an excellent choice for needle tip force measurements during MRI-guided biopsy operations.

In theory, an FPI sensor could be created by securing two distinct optical fibers at certain intervals inside a rigid chamber. Two mirror surfaces (R1 and R2) reflect back small portions of the transmitted light at the sensor probe, producing an interference pattern. When an axial force is applied to the sensor tip, the air cavity length between the two optical fibers varies, altering the optical path of the second reflected light beam

(R2) and the interference pattern's light intensity (Figure 3.1-a). Figure 3.1-b shows the interference pattern's change in relation to the variation in cavity length. At the selected linear segment of the interference pattern, a correlation between the applied force and the light intensity signal may be observed.

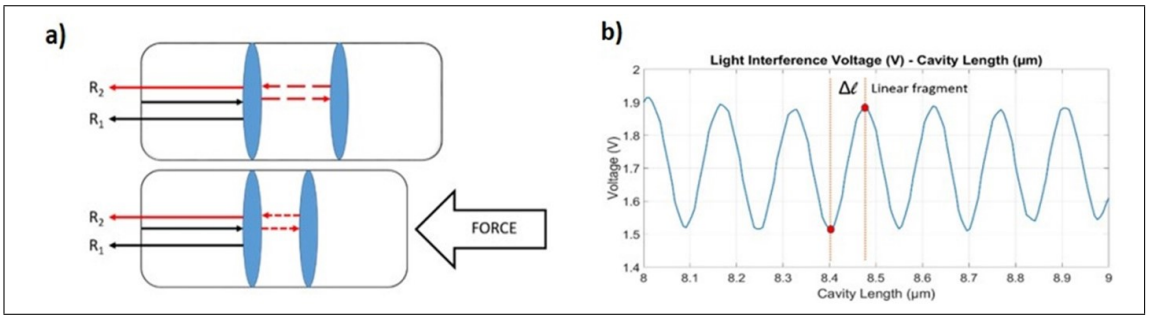

Figure 3.1 **a.** FPI-based sensor **b.** Light intensity of the interference pattern with respect to reflected light beam path difference.

Minimally invasive procedures that require high sensitivity and accuracy, such as epidural needle injections or biopsy operations, might include potential needle deflections because of the various mechanical properties of various tissue types, which can result in safety risks or false negative findings. The success and safety of the procedures can both be enhanced by the real-time assessment of needle tip force during needle insertion. On top of that, needle tip force measurement enables differentiation between tissues of varying stiffness, such as benign and malignant tumorous tissues.

3.2 Methods

3.2.1 Sensor probe design and fabrication

The Design of the FPI-based fiber optic sensor probe is given in Figure 3.2. Polished end surfaces of a single-mode optical fiber (transmitting fiber, 125 μm cladding diameter) and a multimode optical fiber (reflecting fiber, 400 μm cladding diameter) fixed inside of a glass capillary to form two mirror surfaces necessary for FPI-based force sensing via reflected light beams. Two optical fibers are fixed inside the glass tube by applying UV curable adhesives through the micro holes on the glass, forming

an air cavity between them. The air cavity creates a path difference between the two reflected light beams and hence forms an interference pattern.

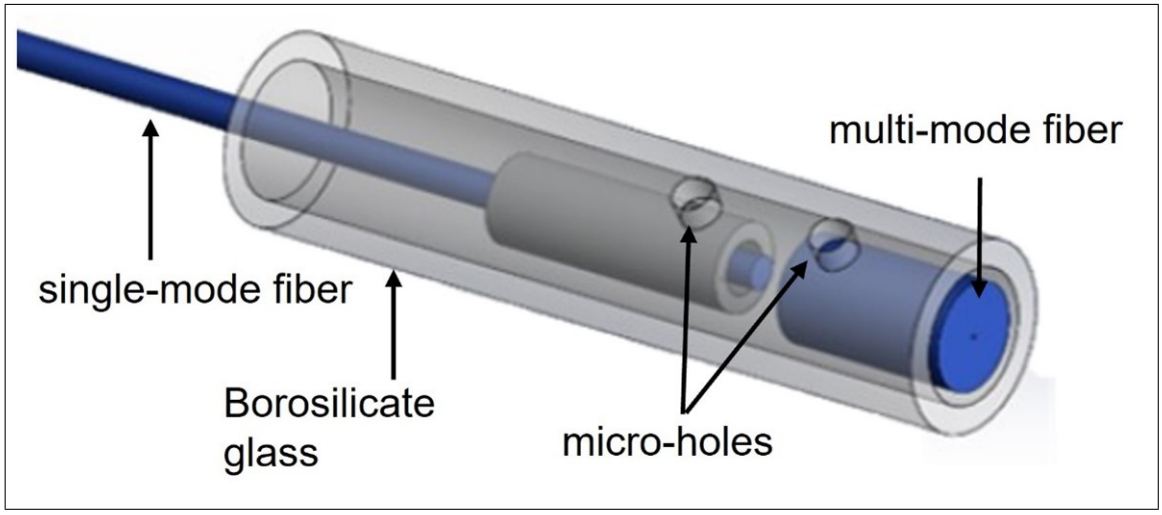

Figure 3.2 Custom fiber optic force sensor probe design using Fabry-Perot interferometry.

Through the placement of micro-hole anchoring points, this innovative sensor probe design enables us to specify the maximum force range. We can also improve the signal-to-noise ratio (SNR) performance by capturing the light reflected from the multimode fiber's broad mirror surface. The gauge length, which is determined by the micro-holes created on the glass capillary, is the distance between the fixing points of two mirror surfaces to the glass tube. The relationship between the gauge length and the usable force range of the manufactured sensor probe is shown in Eq. 3.1 given below.

$$\Delta L_C = F \cdot (1 - 2\mu) \cdot L_G / E\pi(r_o^2 - r_i^2) \tag{3.1}$$

In equation 3.1, ΔL_C is the cavity length between two mirror surfaces, F is the applied force, μ is the poisons ratio,L_G is the gauge length (distance between two micro-holes), E is the elastic modulus of the glass tube, r_o and r_i are the outer and

inner diameter of the glass tube respectively.

Only 4% of the exposed light beam reflects back from a polished bare fiber surface [133]. Using a multimode fiber with a larger reflective surface as the secondary optical fiber helps obtaining the maximum possible SNR but it does not increase the signal intensity. Increasing the light intensity of the secondary reflected light can result in a higher intensity of the interference pattern and hence a higher SNR. It is shown that one efficient method for improving the resolution through greater reflected light intensity is to coat the multimode fiber with a material of higher reflectivity, such as titanium (Ti), aluminum (Al), or magnesium (Mg) in Figure 3.3-b. Figure 3.3 shows Titanium coated multi-mode fiber surface and the light intensity of the interference pattern with regard to the cavity length change between the two fibers for bare fiber and Ti or Mg-coated multimode fibers. The sensor probe with the multimode fiber coated with titanium produces the highest intensity reflected light.

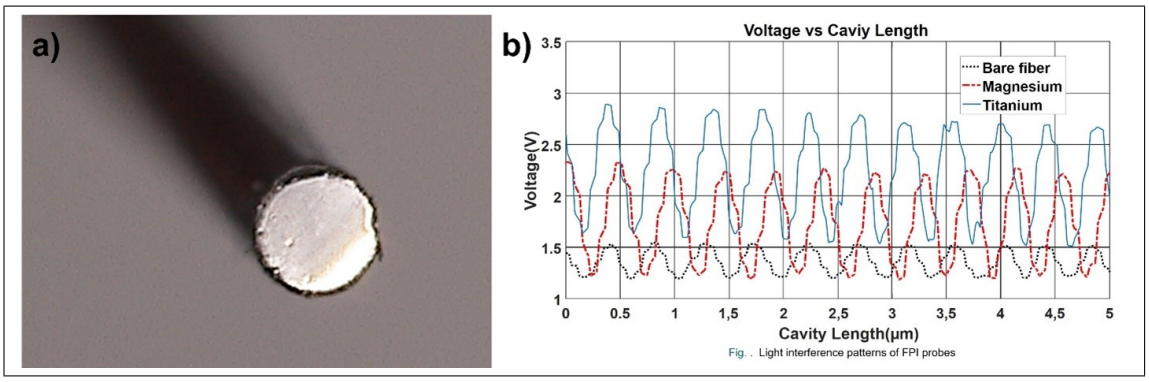

Figure 3.3 **a.** Titanium coated multi-mode fiber surface **b.** The effect of cavity length on the light intensity of interference patterns using bare fiber, Magnesium coated, and Titanium coated multi-mode fibers as the secondary mirror surfaces.

Figure 3.4 shows the fabrication steps of the fiber optic sensor probe and the integration of the sensor probe into the biopsy needle at the needle tip. As the first step of the sensor fabrication, A CO_2 laser engraver system (Epilog Helix Laser) was used for cutting a 4 mm long glass tube (outer diameter (OD): 0.7 mm, inner diameter (ID): 0.5 mm) and forming 0.1 mm diameter micro-holes on the glass surface as shown in figure 3.4-a. To increase the reflectivity of the multi-mode fiber end surface, after polishing the muti-mode fiber it was coated with titanium using sputtering method.

The polished surface of the multi-mode fiber is shown in figure 3.4-b. As the next step multi-mode fiber was placed inside the glass capillary tube and fixed to the borosilicate glass by applying UV-curable adhesive through one of the micro-holes.

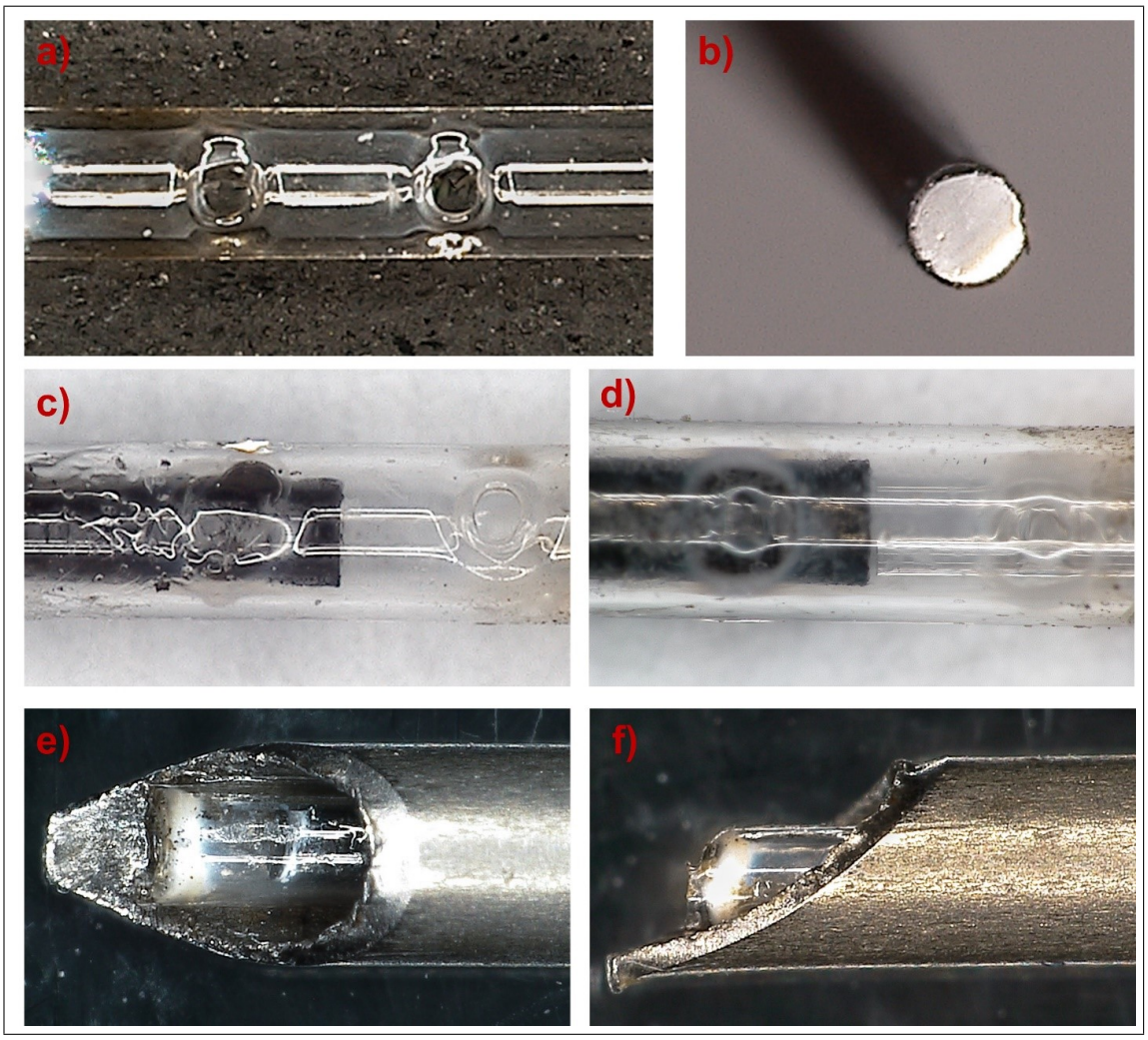

Figure 3.4 **a.** Micro-hole formation on the borosilicate glass tube. **b.** Ti-coated multi-mode fiber surface. **c.** Placing and fixing the multi-mode fiber in a glass tube by applying UV curable adhesive through the micro-hole. **d.** Placing and fixing the single-mode fiber in the glass tube by applying UV curable adhesive through micro-hole **e-f.** integration of the sensor probe into the biopsy needle.

The glass tube with multi-mode fiber fixed inside of it is shown in figure 3.4-c. The single-mode optical fiber that will carry the light from the laser source to the sensor probe was placed inside the glass tube from the other side of the glass and fixed at a position leaving a small cavity between two fiber surfaces by applying UV curable adhesive through the second micro-hole. The glass tube with 2 fibers with a cavity length between them is shown in figure 3.4-d. Finally, the sensor probe was inserted

into the nitinol biopsy needle and placed and fixed at the needle tip using UV curable adhesive. Figure 3.4-e and f shows the sensor position at the needle tip.

3.2.2 Optical setup of the fiber optic force sensor

The optical setup for measuring the needle tip force is given in figure 3.5. The optical setup is composed of, a laser driver circuit (Thorlabs Ek1101), a laser diode (Thorlabs LP635-SF8), an optical cage that contains 2 fiber collimators, a beam splitter and a photodetector (Thorlabs APD), a micro controller (Texas Instruments MSP 430), and finally a laptop for monitoring.

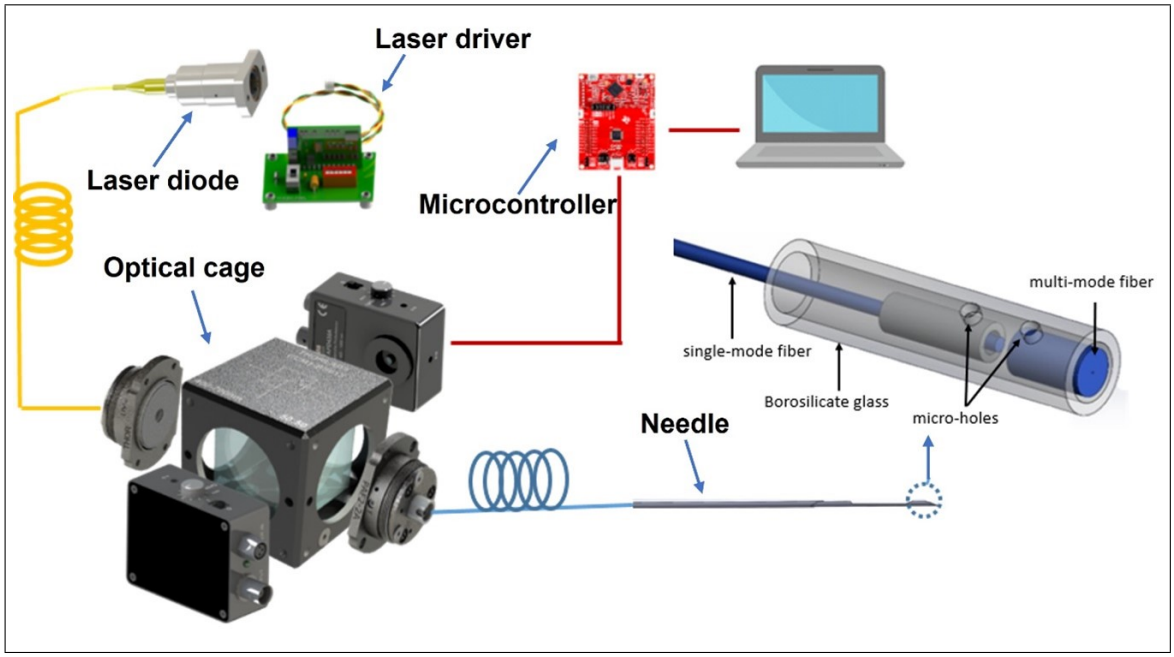

Figure 3.5 Optical setup for force measurements using fiber optic sensor.

A coherent light beam with 635 nm wavelength is supplied by the laser diode which is driven with the laser driver. The laser light passes through the first collimator of the optical cage and the light that passes through the beam splitter enters into the first optical fiber of the sensor probe via the second fiber collimator. The light beams travel to the sensor probe and a fraction of transmitted light beam reflects back from 2 mirror surfaces. Reflected light beams return to the beam splitter passing through the

second fiber collimator. Half of the returning light reflects 90^0 by the beam splitter and falls on the photodetector. The photodetector transforms the light into voltage and transfers the light intensity signal to the microcontroller. The microcontroller converts the analog signal to digital and sends it to the PC via serial port communication. The signal is read from the serial port using MATLAB software (Mathworks) and the signal is recorded and plotted in real time using MATLAB software.

3.2.3 Benchtop experiments

Benchtop studies were performed to test the functionality of the biopsy needle that is integrated with the custom-designed FPI-based fiber optic force sensor. By comparing the responses of the FPI-based force sensor with commercial tension/compression test equipment (LF-Plus, Lloyd Instruments Ltd.) against an applied axial force, The maximum force value that can be measured with the sensor probe and the resolution of the FPI force sensor were determined with benchtop experiments.

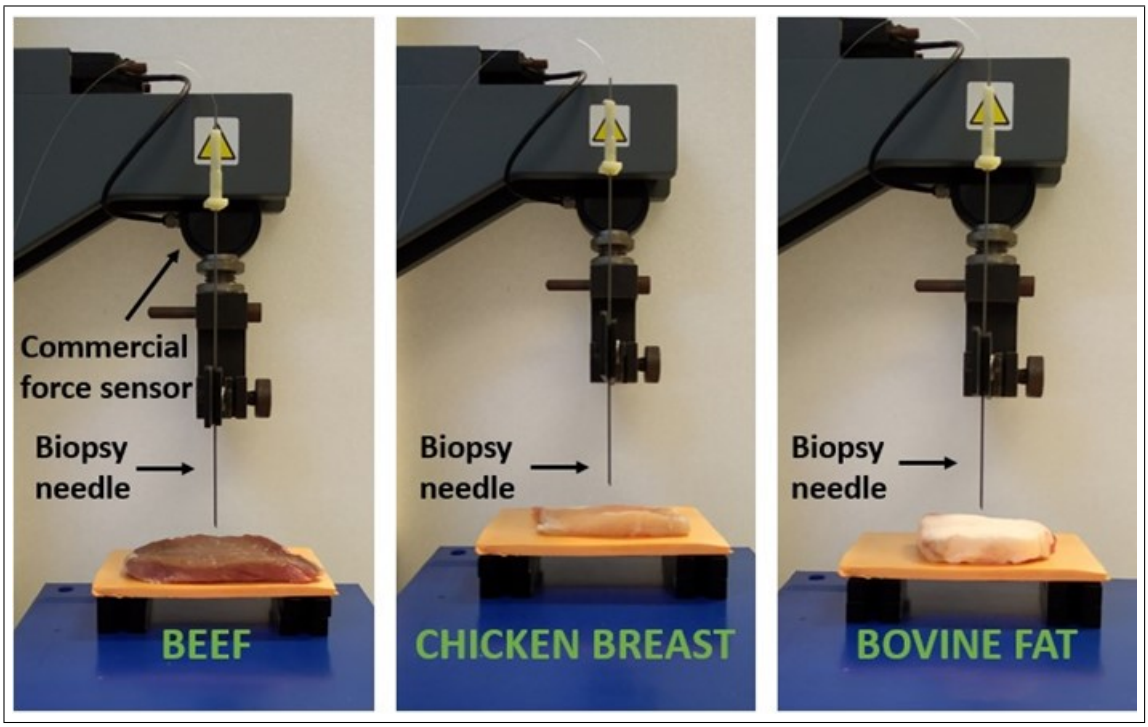

Figure 3.6 Benchtop needle insertion experimental setup with different tissue types.

After determining the range and resolution of the sensor, the fiber optic force

sensor's capability of distinguishing different tissues was tested during needle insertion using tissue types with different stiffness. Beef, chicken breast, and bovine fat tissues were used for this experiment. The biopsy needle that contains the FPI-based sensor at the needle tip was integrated into the commercial tension/compression test equipment. The needle was inserted into the tissue samples at a constant speed using the compression feature of the test equipment making a vertical angle with the samples. The force measurements are recorded with both the tension-compression test equipment and the optical setup of the FPI-based force sensor. The experimental setup is shown in Figure 3.6. To see the effect of increasing the sensor resolution via increasing the reflectivity of multimode fiber by titanium coating, the same experiment was repeated using another biopsy needle that contains an FPI sensor that is designed using a bare multi-mode fiber instead of a titanium-coated one.

Initial benchtop needle insertion tests were performed using beef, chicken breast, and fat tissues representing different tissue stiffness levels. Next, to test the FPI-based force sensor's capability to measure the stiffness gelatin samples with different stiffness levels were prepared using gelatin powder. Gelatin samples with 5 different stiffness levels were prepared by mixing gelatin powder with water in 5 different concentrations. The stiffness levels of the gelatin samples were measured using the tension-compression test equipment. Gelatin concentrations of the samples and the mean elastic modulus values of the samples are given in Table 3.1 below. The stiffness detection performance of the force sensor was tested by inserting the biopsy needle into the gelatin samples and recording the insertion force measurements.

Table 3.1
Stiffness values of gelatine phantoms

Gelatin concentrations (kg/L)	Bloom value of gelatin powder	Mean elasticity (kPa)
0.08	100	19.2
0.12	100	34.3
0.08	200	49.9
0.12	200	91.6
0.2	200	210.7

3.2.4 Experiments under MRI

The performance of the FPI-based force sensor integrated biopsy needle was tested under MRI (3T Siemens Magnetom Trio). A commercially available prostate phantom (CIRS Prostate Phantom Model 070L) that contains tumor-mimicking lesions was used as the test sample. A hydraulic custom-designed prostate biopsy robot that was designed by our group for another project was used for inserting the needle into the prostate phantom at a constant speed from the scanner control room.

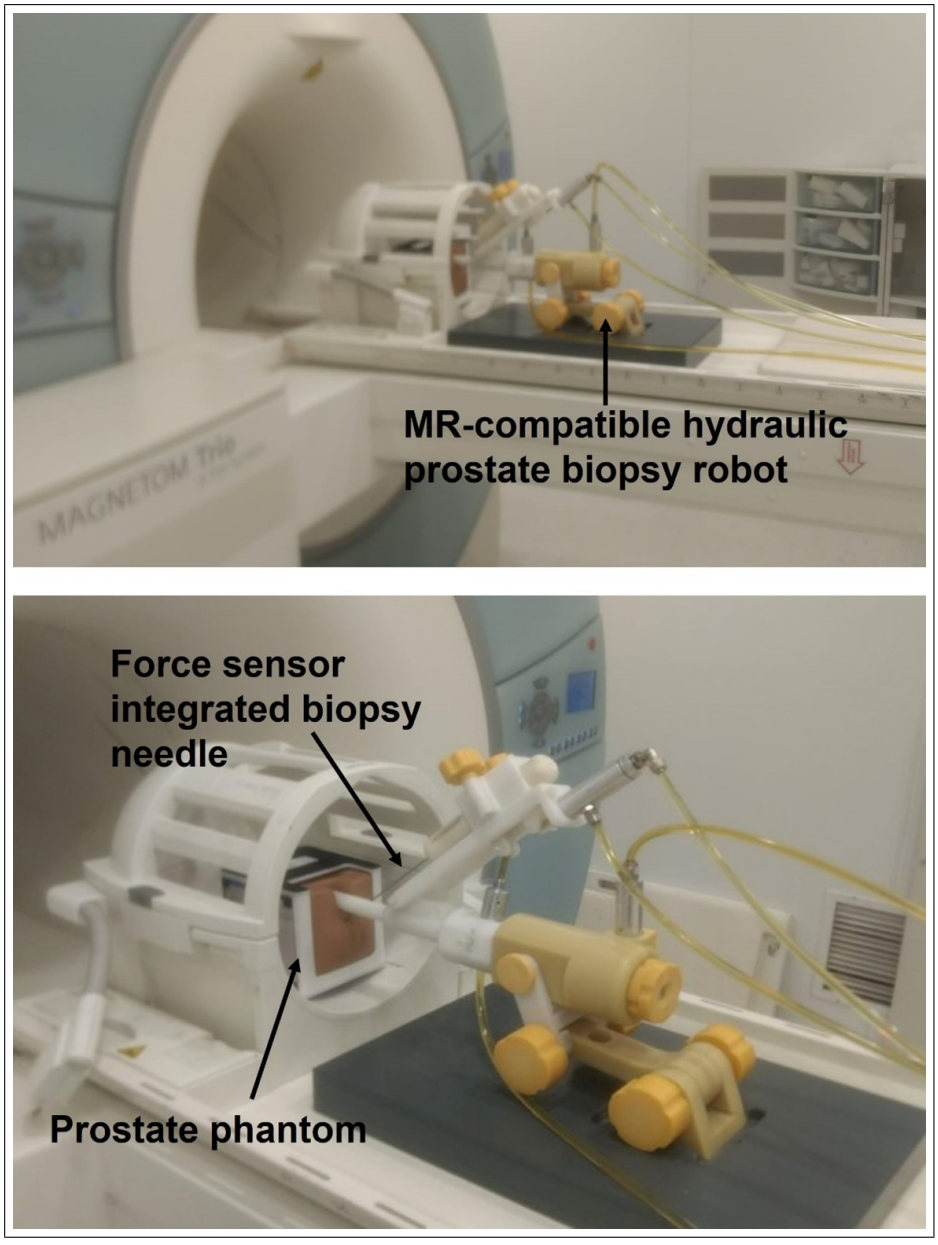

Figure 3.7 In-vitro experimental setup under MRI.

The experimental setup for the in-vitro MRI experiment is given in Figure 3.7. MRI compatibility of the biopsy needles with integrated sensors, their performance, and their response against the applied axial force during the penetration into the prostate phantom was tested using the experimental setup. For the experiment, the prostate phantom was placed inside of a head coil on the patient table under MRI. The MR-compatible prostate biopsy robot was placed and stabilized on the patient table behind the phantom. FPI-based force sensor integrated biopsy needle is placed on the prostate biopsy robot and inserted in the prostate phantom in 3 steps by guiding the needle with respect to the MR images. In the first step, the needle is inserted into the phantom through the outer layer of the phantom. in the second step, the needle is further advanced and inserted into the lesion inside the phantom. Finally, in the 3rd step, the needle was further advanced and exited the lesion. The MR images and the force measurements were recorded during these 3 steps.

3.3 Results

Figure 3.8 illustrates the response of the FPI-based fiber optic force sensor incorporated into a biopsy needle to an axial force when the needle is pushed against a stiff surface. It can be shown that the custom-designed sensor correctly senses the applied force and reacts to the small force changes accurately. In Figure 3.8-a. it is shown that the maximum force that can be measured is discovered to be 20 N. In Figure 3.8-b. the resolution of the sensor is discovered to be 0.03N by coating the multi-mode fiber with titanium and improving the sensor's SNR.

Benchtop studies utilizing beef, chicken breast, and bovine fat tissues are used to examine how biopsy needles with integrated custom-designed FPI-based force sensors respond to various types of tissues. Figure 3.9 compares the responses of the high-resolution sensor probe, which is built using a titanium-coated multimode fiber as the secondary mirror surface, and the sensor probe which is designed using a bare multimode fiber as the secondary mirror surface.

A High-resolution Ti coated sensor provides a greater SNR even though both FPI sensor probes can detect needle penetration into beef and chicken breast tissues. As a result, using a sensor probe with a Ti coating makes measuring stiffness and distinguishing different tissue types easier and more precise. While the Ti-coated sensor probe is producing a discernible reaction to it, bovine fat tissue, which has a lower elastic modulus than beef and chicken breast, could not elicit a response on the bare fiber sensor probe during needle insertion.

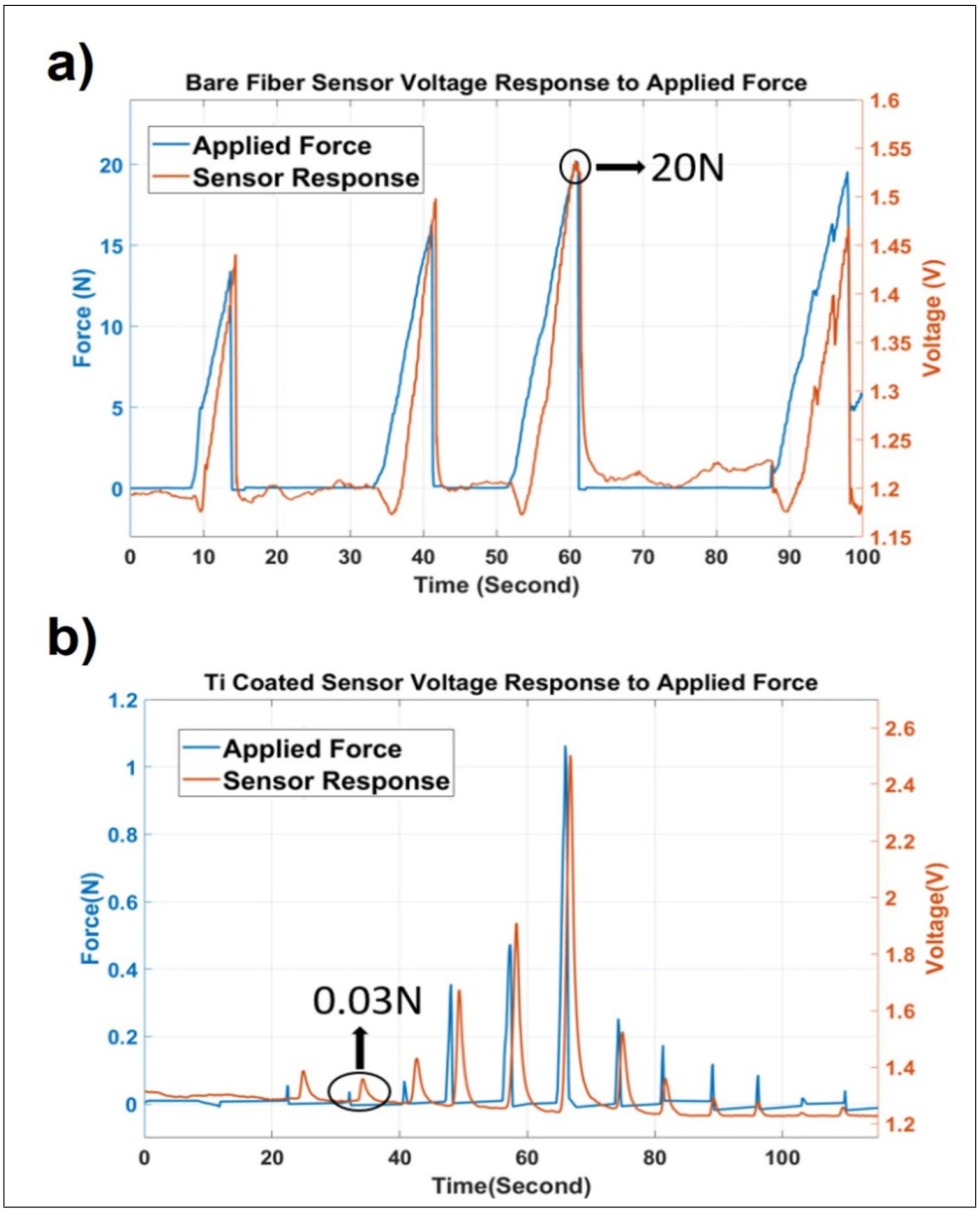

Figure 3.8 Custom designed force sensor response against the force applied to the needle tip. **a.** Force range. **b.** Resolution

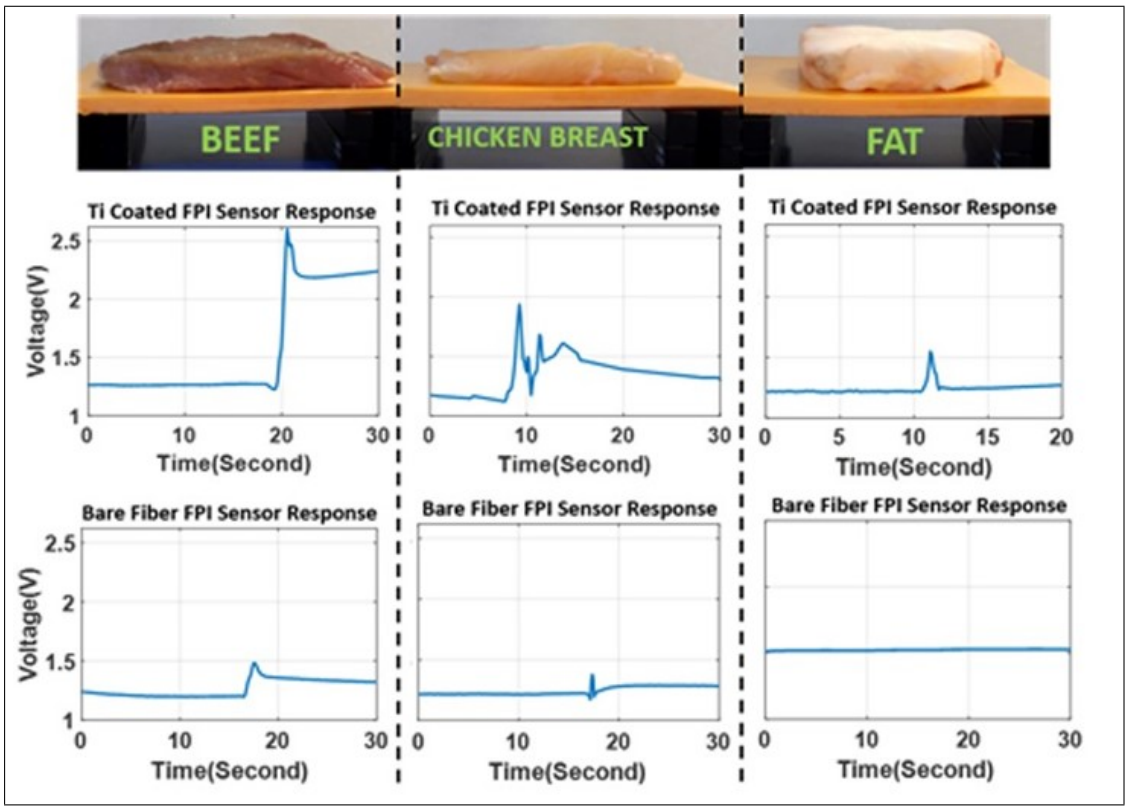

Figure 3.9 Fiber optic force sensor response to different tissue types using Titanium coated and bare multimode fibers .

Further experiments were performed with the high-resolution Ti-coated sensor probe, to test its capability to detect stiffness, utilizing prepared gelatin samples that mimicked different tissue types that have different stiffness and various elastic moduli. Figure 3.10 shows the sensor's response plot to a 210.7 kPa gelatin sample during needle penetration. Table 3.2 shows the response of the fiber optic force sensor during needle insertion into the gelatin samples with different elastic modulus values from 19.2 kPa (kilo pascal) to 210.7 kPa. It can be seen that the high-resolution force sensor can successfully detect the stiffness of a sample.

Figure 3.11 shows the high-resolution FPI based sensor response during needle insertion into the commercial prostate phantom under MRI. During the experiment, the needle was inserted into the prostate phantom in three steps by advancing the needle at a constant speed using the MR-compatible prostate biopsy robot. In the first step, the needle was inserted into the phantom's outer layer. (Outer layer of

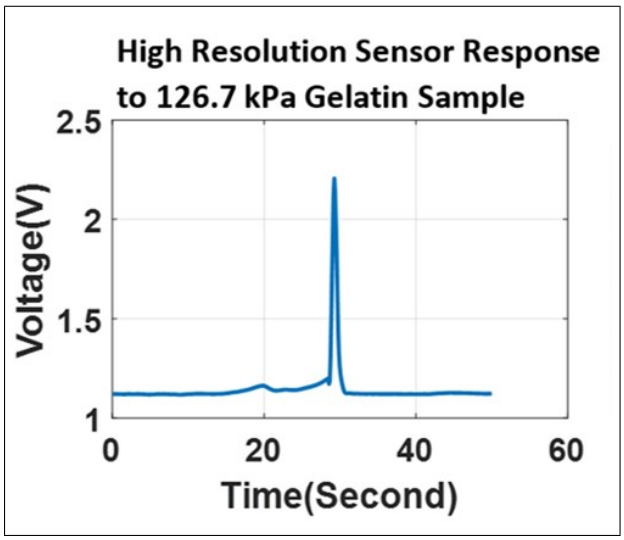

Figure 3.10 Ti-coated sensor response to 210.7 kPa gelatine sample

Table 3.2
High resolution sensor response during needle insertion into gelatin samples

Gelatin sample number	Elastic modulus (kPa)	Sensor response (V)
1	19.2	0.09
2	34.3	0.19
3	49.9	0.26
4	91.6	0.37
5	210.7	1.03

the phantom mimics the skin) MR image of the biopsy needle that is inserted into the outer layer of the prostate phantom is given on the left and the sensor's response during the needle insertion is given below. In the second step, the needle is advanced further to the lesion in the prostate. MR image of the biopsy needle inserted into the lesion inside the prostate is given in the middle and the sensor response is given below the corresponding MR image. In the third step, the needle advanced in the phantom further and exited the lesion. MR image of the third step is given on the right and the sensor response of this step is given below the corresponding MR image. As can be seen in Figure 3.11 the needle tip force sensor was able to successfully detect all 3 steps during needle insertion. MRI compatibility of the biopsy needle and the fiber optic sensor was also tested this way. It was seen that the nitinol biopsy needle and

the fiber optic force sensor were not affected by the high magnetic field environment of the MRI and don't generate any image degradation.

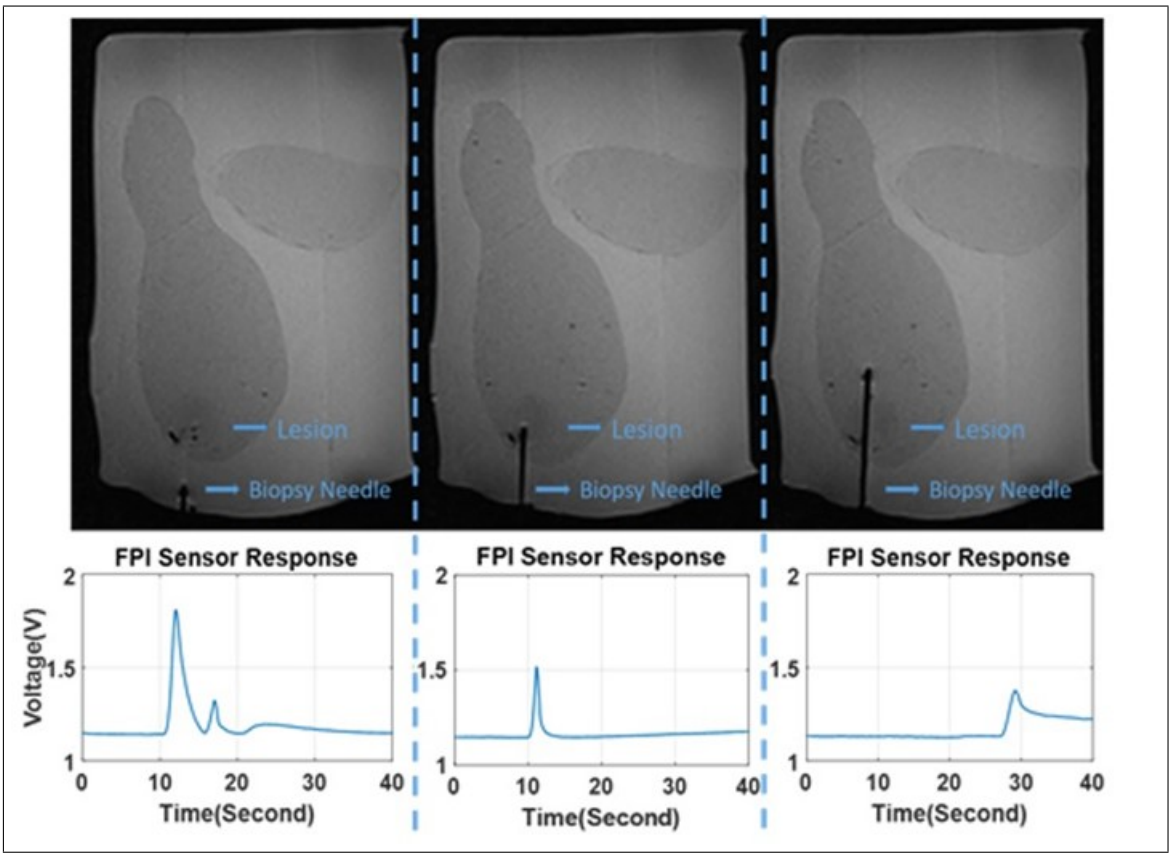

Figure 3.11 MR image and sensor response during needle insertion into the prostate phantom with lesions in three steps

3.4 Conclusion

In this study, we introduced Titanium coated and bigger diameter multi-mode fiber into the sensor cavity to increase the force measurement range and resolution of our Fabry-Perot interferometry-based fiber optic force sensor. An 18-gauge MR-compatible biopsy needle was integrated with the novel sensor. The needle was shown to be capable of detecting needle insertions, peaks, tiny fluctuations in applied force, discriminating between different tissue types, and potential needle deflections in real-time during benchtop and phantom MRI experiments. The new FPI-based force sensors in the custom-designed biopsy needles can detect contact forces up to 20 N. The sensor

with Ti coating on the second reflecting surface of the multimode fiber was found to have an enhanced resolution of 0.03N.

3.5 Discussion

By combining MRI's excellent soft tissue contrast with the capacity to measure force applied to the needle tip, biopsy needles with force feedback capability could potentially be used to increase both the accuracy and safety of MRI-guided minimally invasive procedures, particularly biopsies. As an ideal candidate for force measurement applications for MRI-guided procedures, FPI-based sensors are compact, biocompatible, and resistant to electromagnetic and RF interferences.

Our team has demonstrated that a biopsy needle equipped with an integrated FPI-based force sensor is capable of measuring applied axial forces up to 13 N at the needle tip with a resolution of 0.1 N in our earlier work [134]. To reduce signal losses caused by angle mismatches between the two reflecting surfaces and to provide a simpler manufacturing procedure, we have chosen a bigger diameter multimode fiber as the second reflective surface of the FPI cavity in this study. By varying the spacing between the micro-holes on the glass capillary, we are able to determine the force range of the sensor using our novel sensor probe design.

In order to create a sensor probe with a greater resolution, the new sensor design incorporates a Ti coating on the multimode fiber's reflecting surface. The enhanced sensor probe was demonstrated to be capable of detecting force changes as small as 0.03 N during in vitro studies and measuring contact forces up to 20 N.

Improved resolution force sensing biopsy needles can distinguish between tissues with varying degrees of stiffness, as demonstrated by in vitro tests. When the sensor was inserted into beef, chicken breast, or bovine fat tissues, the response of the sensor differs with respect to the tissue's stiffness. Additionally, it was discovered that the sensor's reaction to the gelatin samples was consistent with the samples' elastic moduli.

Table 3.3
Stiffness values of benign and malignant breast and prostate tissues from previous studies.

Study	Benign tissue (kPa)	Malignant tissue (kPa)	Tissue type
Evans et al. [135]	40	153	Breast
Bayat et al. [136]	30.18	90.66	Breast
Athanasiou et al. [137]	45.3	146.3	Breast
Krouskop et al. [138]	36	100	Prostate
Barr et al. [139]	21.2	58	Prostate
Ahmad et al. [140]	74.9	133.7	Prostate

Given that the mechanical properties of malignant and benign tumorous tissues, or healthy tissues, differ, biopsy needles with high-resolution force sensing capability have a great potential to be used for cancer diagnosis without requiring any biopsy procedures at all. Table 3.3 shows the elastic modulus values of healthy and tumorous prostate and breast tissue samples from the literature. It can clearly be seen from the table that there is a significant difference in the mechanical properties of malignant and benign tissue samples. Being able to perform cancer detection without needing a biopsy sample can be very important because cutting a piece of a tissue sample during biopsy might spread the tumorous tissue cells to the bloodstream [141],[142]. The risk of transferring tumorous tissue cells to the bloodstream during a biopsy operation may be greatly decreased by the stiffness detection approach that has been established using FPI-based force sensing.

4. ANALYSIS ON CURRENT CONTROLLED MARKER INHOMOGENEITIES FOR DEVICE TRACKING UNDER MRI

4.1 Introduction

iMRI is a powerful technique that combines the advantages of minimally invasive procedures with the exceptional imaging capabilities of MRI, such as superior soft tissue contrast, real-time imaging with high signal-to-noise ratio (SNR), multi-planar imaging, and an ionizing radiation-free environment [22]-[27]. Using this technology, clinicians may perform a variety of image-guided procedures, including biopsies [46],[143],[144], ablations [145], and catheter-based therapies [146]-[148], with more precision and accuracy than traditional approaches. However, due to the safety issues associated with the high magnetic field environment of MRI and radiofrequency (RF) generated heating on elongated metallic interventional equipment [149]-[152], the use of standard interventional equipment under MRI is substantially limited. Furthermore, the poor visibility of MR-safe interventional equipment, as well as the limited workspace and mobility provided by MRI, might have an impact on operation success [153]-[155].

Improvements in MRI technology began to address some of these issues, making MRI a more appropriate imaging medium for real-time interventional operations. Despite having a lower SNR than high-field standard MRI scanners, low-field and open bore MRI scanners can enhance iMRI therapies. Reduced magnetic field intensity necessitates less shielding and lowers RF-induced heating as well as picture distortions generated by metallic devices [156],[157]. An open bore allows clinicians additional freedom to handle the interventional instruments during procedures [144]. Designing visible and safe interventional instruments is another problem of this profession, even though MRI is becoming a more accessible and appropriate imaging modality for interventional operations every day. To address this issue and improve the visibility of MR-compatible non-magnetic materials, tracking markers are being employed.

Passive markers [107],[109],[110], active markers [111],[112],[158],[159], and semi-active (resonant) markers [114]-[116],[160] are the three types of fiducial markers that have been investigated often in the literature. Winding a conductive wire on the interventional device and delivering direct current (DC) to the wire is another technique for interventional device tracking under MRI [117]. By disturbing the homogeneity of the MRI's magnetic field, the external magnetic field created by the applied DC generates a negative contrast close to the conducting wire. The size of the marker artifacts could be changed by adjusting the applied current, which is a significant benefit over passive markers. Furthermore, unlike active markers, this technique does not require extra software or device-specific hardware, nor does it necessitate a low flip-angle scan or be in resonance with the MRI scanner's Larmor frequency, unlike semi-active markers.

Glowinski et al. [117] demonstrated that by providing a continuous DC and therefore interrupting the B0 field while employing a Gradient-echo (GRE) sequence, this approach could be utilized for catheter tracking, and Eibofner et al. To lessen the refocusing impact of Spin-echo (SE) [118] and Balanced Steady State Free Precession (b-SSFP) [119] sequences on continuous inhomogeneities, used transient DC while employing these sequences for device tracking.

The aim of this chapter is to demonstrate that current applied conductive ink-printed coil markers, rather than wires, can be used for device tracking in all three sequences mentioned above (GRE, b-SSFP, TSE), as well as to conduct a detailed analysis of the effect of applied current type (DC or AC) and parameters (amplitude, frequency, trigger timing with respect to the scan pulse sequence) on tracking marker performance without any image postprocessing.

4.2 Methods

4.2.1 Conductive ink printed solenoid coil design

A 4-axis conductive ink printer system that was built in our earlier work [28] was used for drawing solenoid coils, to be used as current controlled device tracking markers, on polyester heat shrink tubes (103-0580, Nordson Medical, NH, wall thickness = 0.0006") using silver conductive ink (AG-500, Kayaku Advanced Materials, MA). The 4-axis conductive ink printer system is shown in Figure 4.1. Preliminary solenoid coil designs printed using conductive ink using the conductive ink printer system on Peebax tubes are shown in Figure 4.2.

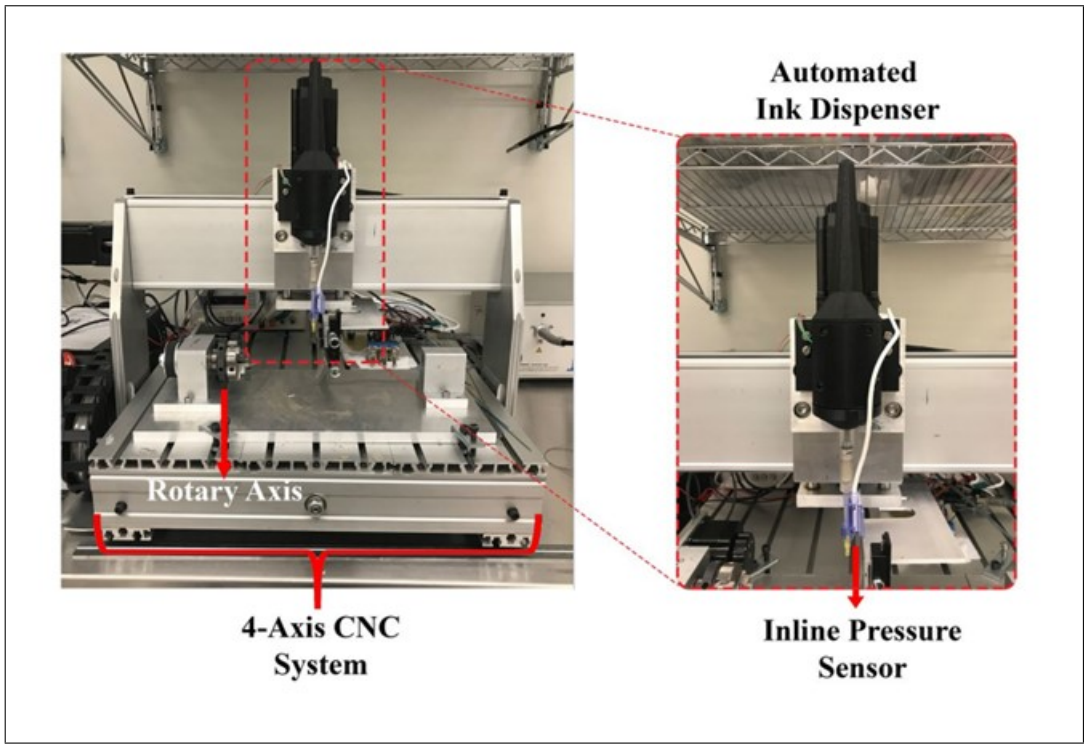

Figure 4.1 4-axis conductive ink printer system [28]

25 mm apart, 5mm long 3 solenoid coils that have 10 turns, 0.2 mm coil pitch, 0.3 mm line width and 0.02 mm line thickness are printed on each heat-shrink tube. The conductive ink printed solenoid coil design is shown in figure 4.3-b. 3 layers of heat-shrink tubes are sleeved and shrunk (hot air station 210-A BEAHM Design inc.) on 6 French (Fr) PEEK rod, shown in figure 4.3-a, that is nearly invisible under

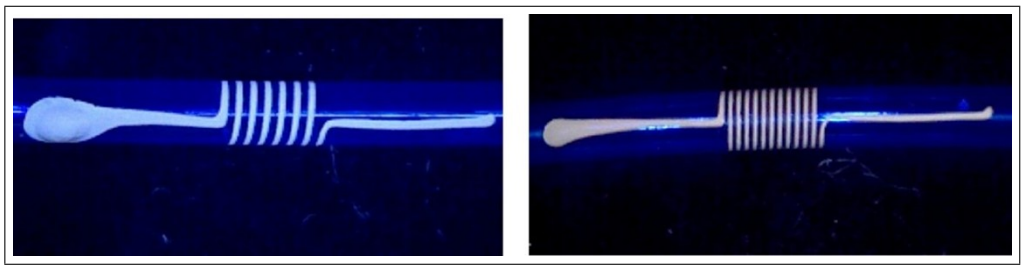

Figure 4.2 Conductive ink printed solenoid coil trials using 4-axis conductive ink printer.

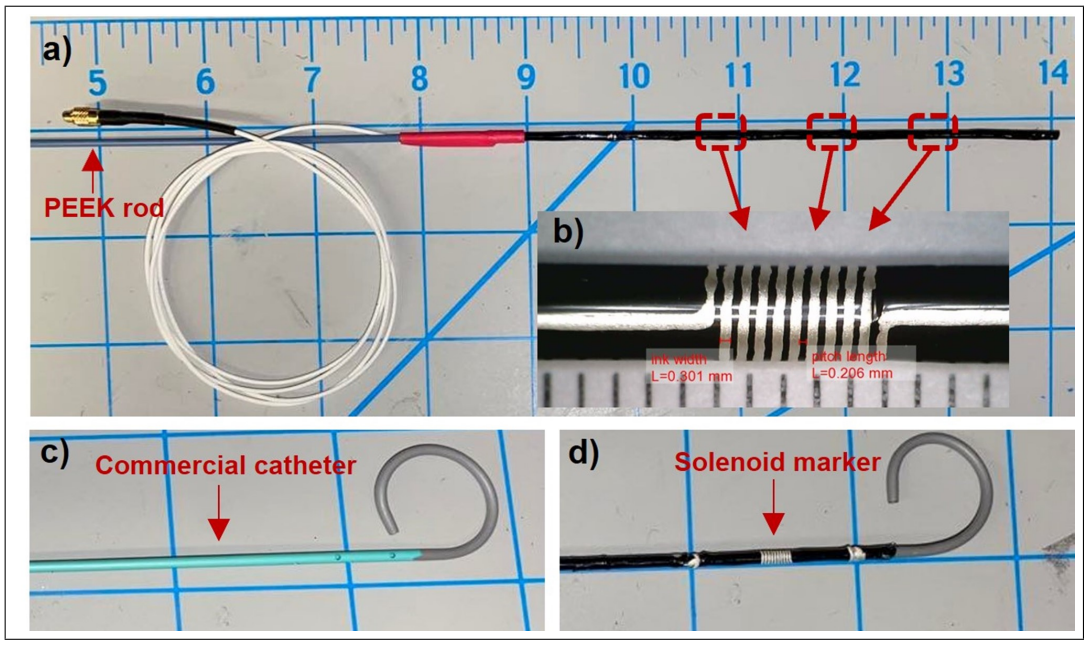

Figure 4.3 **a.** Peek rod test sample that contains 3 layers of polyester heat-shrink tubes with solenoid coil markers **b.** Solenoid coil marker printed polyester heat-shrink tube **c.** Commercially available flush pigtail catheter **d.** Commercially available catheter with a solenoid coil marker..

MRI, mimicking an MR-safe interventional tool. Both the first and the second layers of heat-shrink tubes contain 3 coils that are aligned on top of each other to form the 3 markers. Two layers are electrically connected to each other at the distal tip with silver conductive ink completing the fiducial marker circuitry. Inner and outer conductors of a coaxial cable (9436- WH033, Alpha Wire, NJ) are connected to the fiducial marker circuit from the proximal end of first and second layers respectively. A male mmcx connector was soldered to the proximal end of the coaxial cable, terminating the circuitry for an easy connection to a current supply. A final and a third layer of heat shrink tube placed on the test sample to completely insulate the marker circuit from its surroundings

Another test sample is prepared using a commercially available 5 Fr. flush pigtail catheter (Boston Scientific Imager II M001315230) shown in figure 4.3-c to test the capability of current applied conductive ink printed markers to increase the visibility of commercial MR-compatible interventional tools under MRI. Heat-shrink tubes that contain only 1 marker that is placed at the base of the pigtail of the catheter were used to prepare the catheter sample (figure 4.3-d). The same remaining steps were followed to finalize the sample.

4.2.2 Experimental setup

The experimental setup that was used to test the performance of conductive ink-printed markers under MRI and analyze the effect of current parameters on marker artifacts for 3 different sequences (GRE, TSE, and b-SSFP) is given in Figure 4.4. The test sample, which was prepared using the PEEK rod, was placed inside of a gel phantom, that was prepared following the instructions in ASTM F2182 standard [123], at the isocenter of the scanner making a 45^0 angle with the main magnetic field (B_0) on the XY plane. The current was supplied to the markers either by a DC power supply or a waveform generator from the control room and a reed relay was used when it was needed to trigger the supply current at specific times with respect to the sequence pulse diagrams.

The same experimental setup was used for the commercially available MR-compatible flush pigtail catheter test sample. The only difference was that the catheter sample was placed in the gel phantom parallel with the main magnetic field instead of making a 45^0.

4.2.3 In-vitro experiments

The visibility of both the PEEK rod test sample that contains 3 solenoid coil markers and the commercially available catheter sample that contains 1 solenoid coil

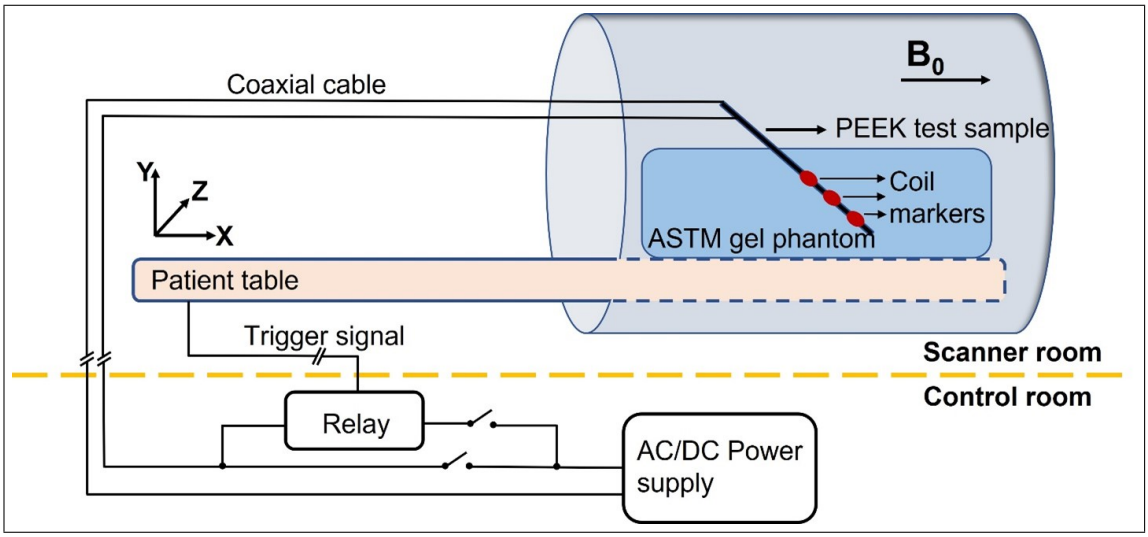

Figure 4.4 Diagram of the experimental setup for in-vitro MRI experiments.

marker were tested under a high performance 0.55 T (prototype Magnetom Aera, Siemens Healthcare, Erlangen, Germany) and 1.5 T (Siemens Magnetom Aera, Siemens Healthcare, Erlangen, Germany) scanners using GRE, b-SSFP and TSE sequences.

For each of the given 3 sequences the effect of applied current type (AC or DC) and applied current parameters such as amplitude and frequency on generated marker artifact sizes are tested and determined using the PEEK rod test sample under high performance 0.55 T scanner. After determining the optimum current type and current parameters for each sequence, the visibility of the commercially available catheter sample was tested under both 0.55 T and 1.5 T scanners using the determined current parameters. Sizes of the marker artifacts were measured and compared using a DICOM imaging software (MicroDICOM) with respect to current parameters such as amplitude and frequency.

MR compatibility of the commercially available pigtail flush catheter was tested under MRI by performing an RF-induced heating experiment, a magnetically induced force experiment, and an artifact experiment before placing the conductive ink-printed solenoid coil on the catheter. RF-induced heating experiment, artifact experiment, and visibility tests are all performed in the ASTM gel phantom. Opsens fiber optic temperature probe (OTG-M170) and Tempsens multi-channel signal conditioner were

used for temperature readings and recordings during RF-induced heating tests. A polyimide port(ID:0.001", length: 100 cm) was fixed to the catheter under test using one-inch-long heat shrink tubes at 5-inch intervals. It was made certain that the polyimide ports are in contact with the catheter at the catheter tip (potential hotspot on the catheter).

The catheter with a polyimide port was aligned parallel to the main magnetic field and placed in a high SAR spot in the ASTM gel phantom under MRI. The fiber-optic temperature probe was first advanced maximally to the distal tip of the polyimide port. the fiber optic probe was withdrawn manually at a constant speed to obtain a longitudinal temperature profile during a 75^0 flip-angle scan using an interactive b-SSFP sequence. The spot that heats up the most on the catheter (the hot spot of the catheter) was determined by manually advancing and withdrawing the temperature probe in the polyimide port with respect to the temperature readings during the MRI scan. The temperature change was recorded at the hot spot for 90 seconds during the scan with 75, 65, and 45 degrees flip angles. Finally, the temperature was recorded for 15 minutes during the scan with 75^0 flip angle to see the maximum temperature rise in the worst case scenario.

The magnetically induced force experiment was performed using the experimental apparatus, given in Figure 4.5, which consisted of a paper protractor placed on an acrylic stand. A brass threaded rod was screwed into the top support and pierced through the paper protractor. The protractor was positioned such that the 90^0 mark was vertical. The guidewire was coiled into a 15 cm diameter coil and suspended from the brass rod such that it was free to swing. The apparatus was placed on the patient table of a 0.55 T MRI scanner such that the distance from the isocenter to the center of the apparatus was 85 cm in the z-direction. This was as close to the isocenter as the apparatus could be placed due to size constraints in the bore. The deflection angle reading on the paper protractor was recorded which is the result of the magnetically induced force on the catheter.

Induced currents on the metallic braidings of catheters or other materials on

the catheters, during RF excitations due to E-field coupling can lead to artifacts in the close vicinity of the catheters. using spin echo imaging bright signal artifact sizes are measured and using gradient echo sequence signal void artifact sizes are measured when the catheter was placed inside of a copper-sulfate (CuSO4) phantom both parallel and perpendicular to B_0.

Figure 4.5 Magnetically induced force measurement test setup.

After completing MR-compatibility tests of the commercially available catheter sample, the experimental setup given in Figure 4.4 was prepared under the 0.55 T scanner, and the visibility of the PEEK rod test sample is evaluated by applying a 25 mA continuous DC and +/- 25 mA continuous AC to the coil markers while using a GRE sequence as a start. The size of the generated marker artifacts is compared. The artifact size control via adjusting the applied current amplitude was tested by comparison between the artifact sizes with respect to the applied current amplitude. The parameters of the GRE sequence were: TE (echo time)/TR (repetition time) = 10 ms/100 ms, BW (bandwidth) = 260 Hz/px, slice thickness = 3mm, matrix size =

256x256, field of view = 400x400 mm^2.

Next, the performance of the conductive ink-printed markers was tested using a b-SSFP sequence. To test the effect of the applied current type on marker artifacts in a b-SSFP sequence and a transient inhomogeneity in the magnetic field instead of a continuous one, 20 mA DC and then +/- 20 mA AC Finally, to test the signal frequency with respect to the repetition time of the sequence, a continuous AC signal with different frequency values (10 Hz - 800 Hz with 10 Hz increments) was applied to the markers. Images were recorded and artifact sizes were compared with respect to different current types and parameters. The parameters of the b-SSFP sequence were: TE/TR = 1.5/3 ms, 2/4 ms, 2.5/5 ms (Three different scans with different TE and TR values were used to test the relationship between the repetition frequency of the sequence and the frequency of the applied AC signal), BW = 235 Hz/px, slice thickness = 8mm, matrix size = 240x158, the field of view = 399x399 mm^2. was applied to the coil markers only during the readout period of the sequence by triggering the applied current with the reed relay first. After that, to test the effect of the current amplitude on marker artifacts a continuous AC signal with different amplitudes was applied to the markers.

As a third step current applied marker artifacts are evaluated using a t2-weighted turbo spin-echo (TSE) sequence with respect to the applied current type (AC or DC) and parameters. Images were recorded and artifact sizes were compared to determine the optimum parameters for the highest conspicuity. The parameters of the TSE sequence were: TE/TR = 75/4000 ms, BW = 95 Hz/px, slice thickness = 3mm, matrix size = 448x336, field of view = 340x340 mm2.

After determining the effect of the current type and parameters on marker visibility for each sequence, visibility of commercial 5 Fr. pigtail catheter that contains a conductive ink printed marker (Boston Scientific Imager II M001315230) was tested under 0.55T scanner for all 3 sequences. Finally, the visibility of both the 5 Fr. pigtail catheter and 6 Fr. Peek rod is tested under 1.5 T scanner. The marker images were recorded for all 3 sequences under 1.5 T scanner to show the capability of cur-

rent applied conductive ink-printed markers to work under MRI scanners with different magnetic strengths.

4.3 Results

The results of MR-compatibility experiments performed under high performance 0.55 T scanner are given in Figure 4.6 and Figure 4.7. Figure 4.6 shows the 90-second heating recordings from the hotspot of the commercial catheter during interactive b-SSFP scans with 75^0, 65^0, and 45^0 flip angles and a 15-minute long interactive b-SSFP scan with 75^0 flip angle. Temperature changes for 90-second scans are recorded as 0.69^0C, 0.65^0C, and 0.48^0C for 75^0, 65^0, and 45^0 flip angles respectively. After the 15-minute long scan, a 1.31^0C temperature rise was recorded.

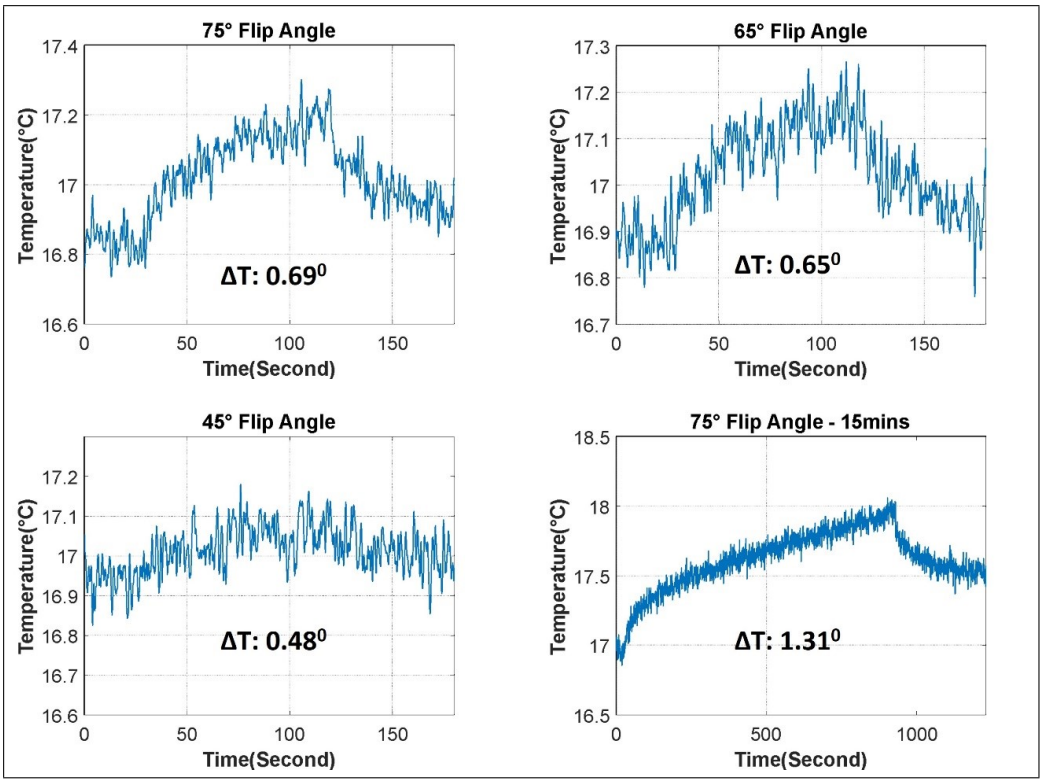

Figure 4.6 RF induced heating experiments of the commercially available catheter (Boston Scientific Pigtail Flush catheter).

Figure 4.7 shows Gradient-echo and Spin-echo artifact images of the commercial catheter when the catheter is parallel to the main magnetic field and vertical to the

main magnetic field. No artifact formation was observed when the catheter was parallel to the main magnetic field and artifacts with 1.8 mm and 6.2 mm sizes were observed when the catheter was placed perpendicular to the main magnetic field for SE and GRE images respectively.

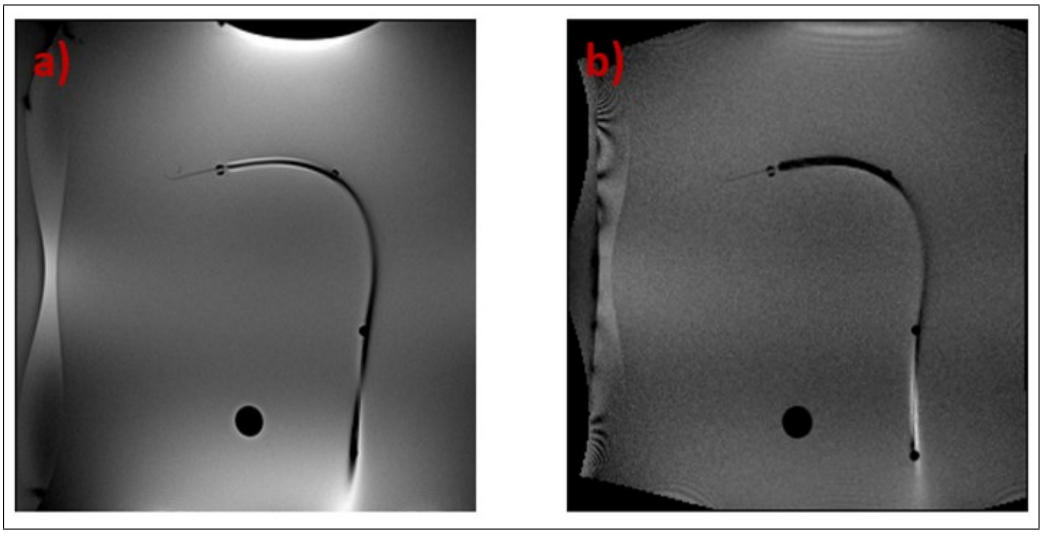

Figure 4.7 Artifact experiments of the commercially available catheter (Boston Scientific Pigtail Flush catheter) **a.** Spin-echo image **b.** Gradient-echo image.

In Figure 4.8, a sample GRE pulse sequence diagram and below the diagram 2 different current types that were applied to the markers separately with respect to the pulse diagram during the GRE imaging are given. Alongside the sample GRE pulse diagram, the resulting sagittal MR images of the solenoid coil marker artifacts are shown in the figure. The MR image placed on top resulted from the application of 25 mA continuous direct current to the conductive ink-printed markers. The MR image placed at the bottom resulted from the application of +/- 25mA 5 Hz (half the repetition frequency of the sequence) alternating current to the conductive in printed coil markers. The generated distal tip marker artifact sizes were measured as 8.6 mm and 8.8 mm for Direct current and Alternating current respectively. It can be seen that the marker artifact size doesn't get affected much by the applied current type. The only remarkable difference between the 2 images is the shape of the generated artifact. While an elliptical artifact was generated by applying a continuous DC to the markers, applying a continuous AC, the artifacts took on a cross-shaped appearance in the sagittal images because of the change in the externally generated magnetic field's

direction every read-out period.

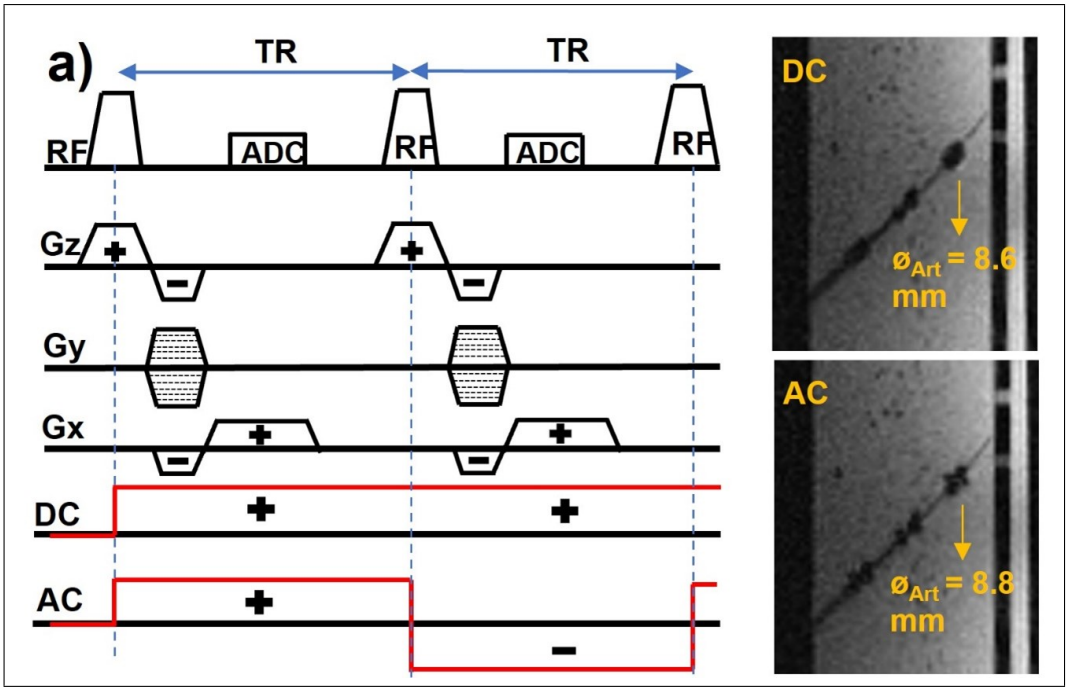

Figure 4.8 Two different applied current types with respect to GRE sequence pulse diagram and resulting MR images of conductive ink printed markers.

The effect of applied current amplitude on generated marker artifact sizes with sagittal (first row) and coronal (second row) images of the PEEK rod are given in figure 4.9. A continuous and constant DC was applied to the fiducial markers with current amplitudes, 0mA, 25mA, 50mA from left to right. Applying 25 mA DC resulted in distal marker artifacts with 8.6 mm and 8.5 mm radii and, applying 50 mA DC resulted in distal marker artifacts with 10.3 mm and 10.1 mm radii in sagittal and coronal images respectively. It can be seen that without applying any current to the markers the PEEK rod prototype is nearly invisible using GRE sequence and applying a constant and continuous DC to conductive ink printed coil markers can form conspicuous artifacts in a GRE sequence and the marker artifact sizes can be controlled by adjusting the applied current amplitude.

In Figure 4.10, a sample b-SSFP pulse sequence diagram and below the diagram 2 different current types that were applied to the markers separately with respect to the pulse diagram during the b-SSFP imaging are given. Both the DC and AC were applied

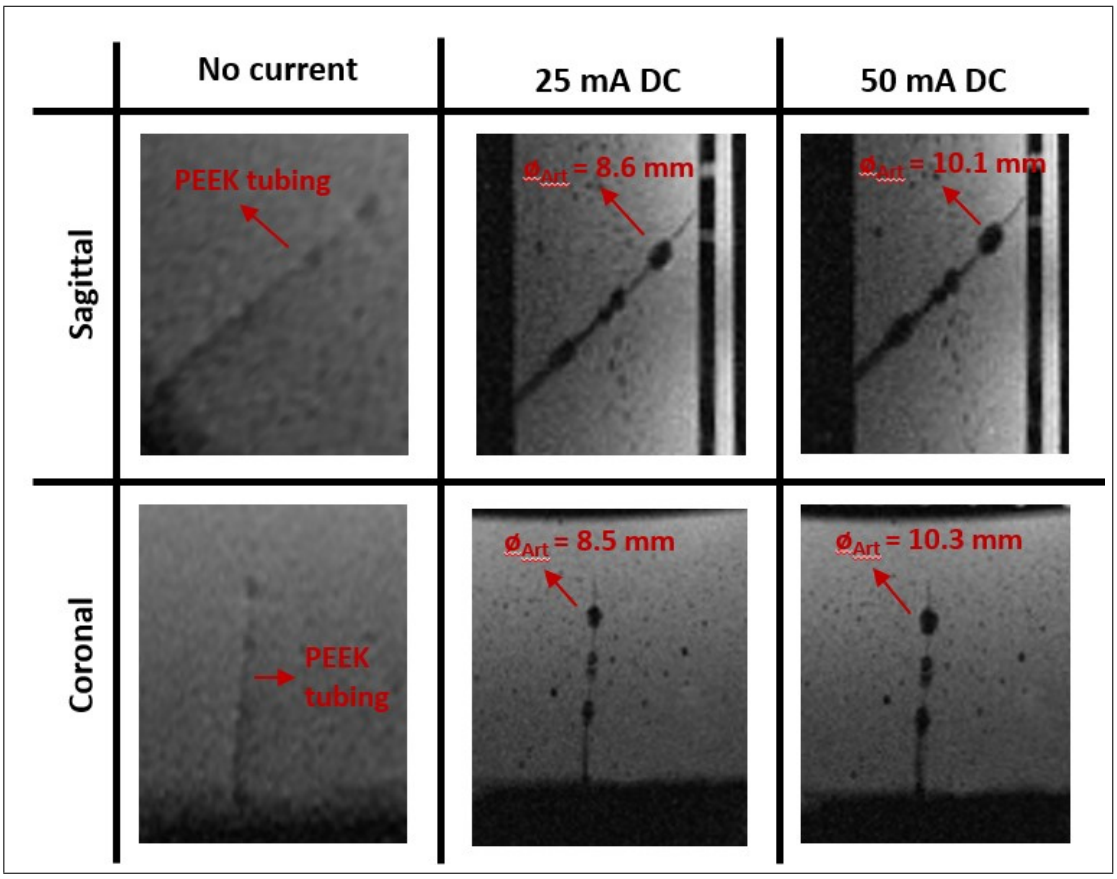

Figure 4.9 Coronal and sagittal GRE images of AC applied conductive ink printed markers and the effect of current amplitude on the marker artifact size.

to the markers only during the readout period of the b-SSFP sequence by triggering the applied current using a reed relay. Alongside the sample b-SSFP pulse diagram, the resulting sagittal MR images of the solenoid coil marker artifacts are shown in the figure. The MR image placed on top resulted from the application of 20 mA triggered direct current to the conductive ink-printed markers. The MR image placed at the bottom resulted from the application of +/- 20 mA 166 Hz (half the repetition frequency of the sequence. The repetition time of the b-SSFP sequence was 3 ms.) alternating current to the conductive in printed coil markers. The generated distal tip marker artifact sizes were measured as 4.7 mm and 10.7 mm for Direct current and Alternating current respectively. It can be seen that because of the effect of refocusing gradients of b-SSFP sequence on constant inhomogeneities, applying DC to the marker artifacts can't form artifacts as large as AC-generated artifacts. For b-SSFP sequence changing the direction of generated inhomogeneity in every consecutive read-out period

of the sequence can overcome the refocusing effect of gradient fields and can form more conspicuous artifacts.

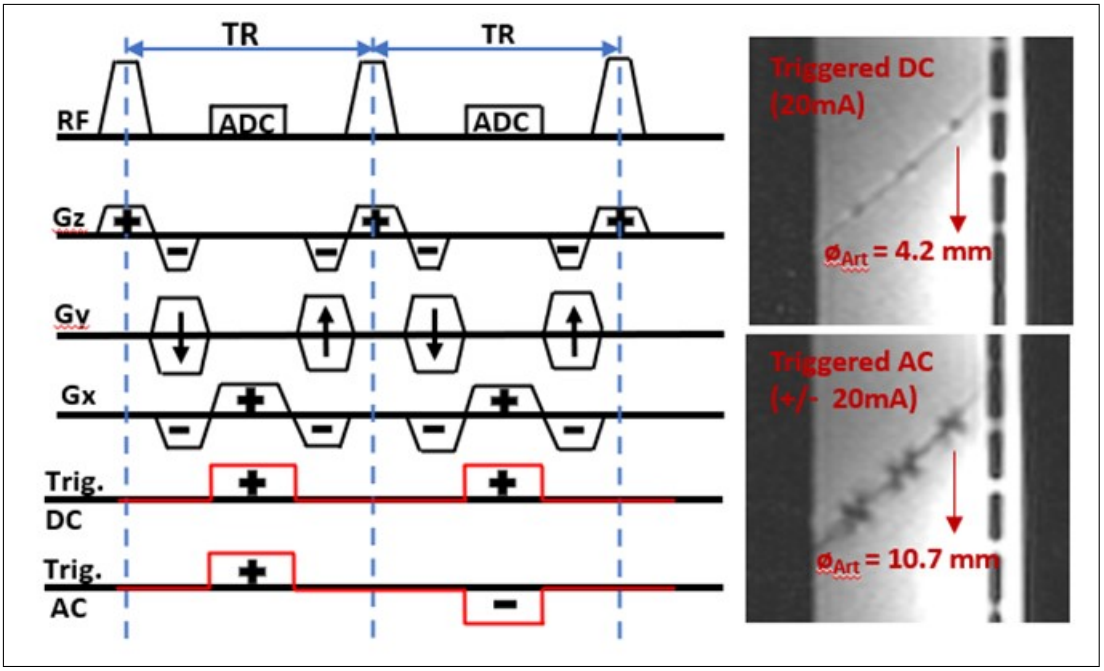

Figure 4.10 Two different applied current types with respect to b-SSFP sequence pulse diagram and resulting MR images of conductive ink printed markers.

The effect of applied current amplitude on generated marker artifact sizes using b-SSFP sequence with 3 ms repetition time with sagittal (first row) and coronal (second row) images of the PEEK rod are given in Figure 4.11. A continuous AC was applied to the fiducial markers with current amplitudes, 0 mA, +/- 10 mA, and +/- 20 mA from left to right. In the first column of images, the PEEK prototype is almost invisible without any current application. Applying +/- 10 mA 166 Hz AC resulted in distal marker artifacts with 10.2 mm and 6 mm radii and, applying +/- 20 mA 166 Hz AC resulted in distal marker artifacts with 13.0 mm and 8.9 mm radii in sagittal and coronal images respectively. It can be seen that without applying any current to the markers the PEEK rod prototype is nearly invisible using b-SSFP sequence and applying an alternating current, that changes its direction every consecutive read-out period of the sequence instead of a constant direct current, to conductive ink printed coil markers can form conspicuous artifacts in a b-SSFP sequence and the marker artifact sizes can be controlled by adjusting the current amplitude.

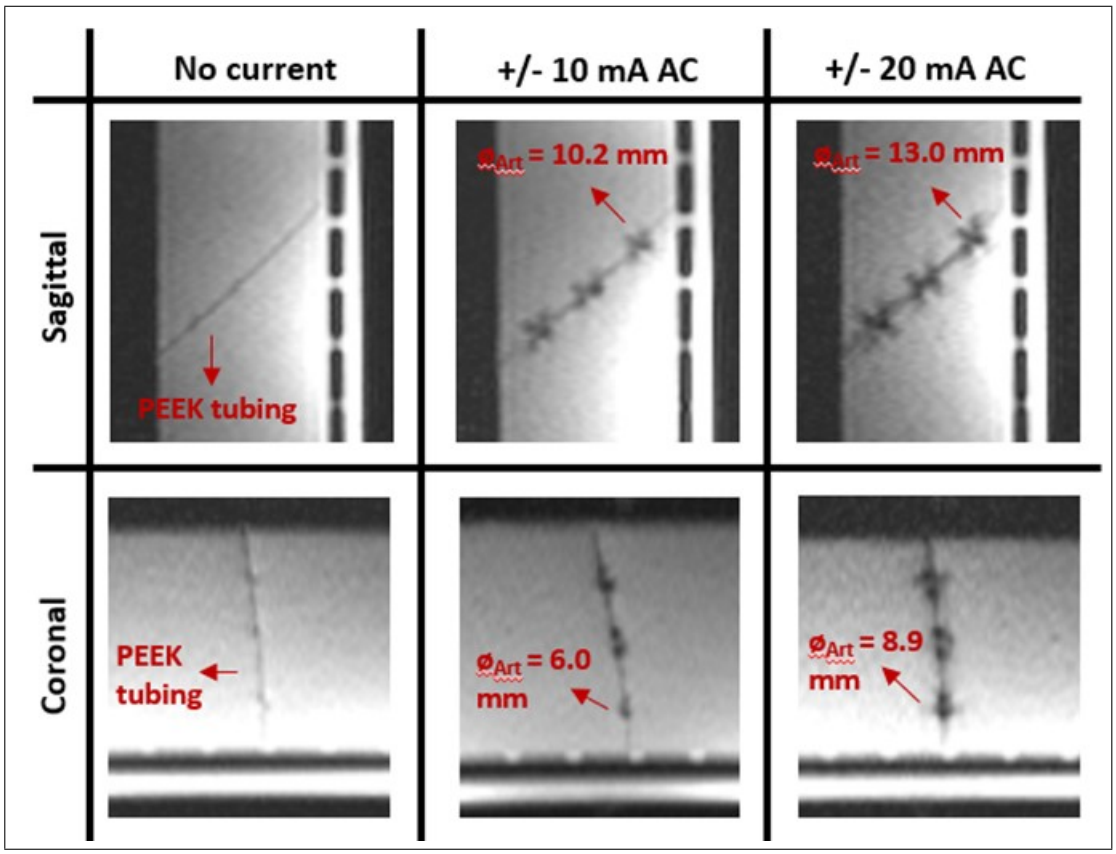

Figure 4.11 Coronal and sagittal b-SSFP images of AC applied conductive ink printed markers and the effect of current amplitude on the marker artifact size.

The effect of the applied current frequency on marker artifact sizes for different repetition times (TR) using b-ssfp sequence is shown in the plot given in figure 4.12. Distal marker artifact sizes are measured on b-SSFP images of the PEEK prototype while +/- 10 mA AC was applied to the markers with frequency values between 10 Hz and 800 Hz with 10 Hz increments for 3 ms, 4 ms, and 5 ms scan repetition times.

It can be seen that the largest artifact sizes were obtained when the frequency of the applied current was half of the repetition frequency of the b-SSFP sequence. For 3 ms repetition time, the repetition frequency is 333.33 Hz, for 4 ms repetition time the repetition frequency is 250 Hz, and finally for 5 ms repetition time the repetition frequency is 200 Hz. It can be seen in Figure 4.12 that the highest marker artifact was obtained when 166 Hz AC (between 160 Hz - 170 Hz in the figure) was applied during a b-SSFP scan with 3 ms TR, 125 Hz (between 120 Hz -130 Hz in the figure) AC was applied during a b-SSFP scan with 4 ms repetition time and, 100 Hz AC was

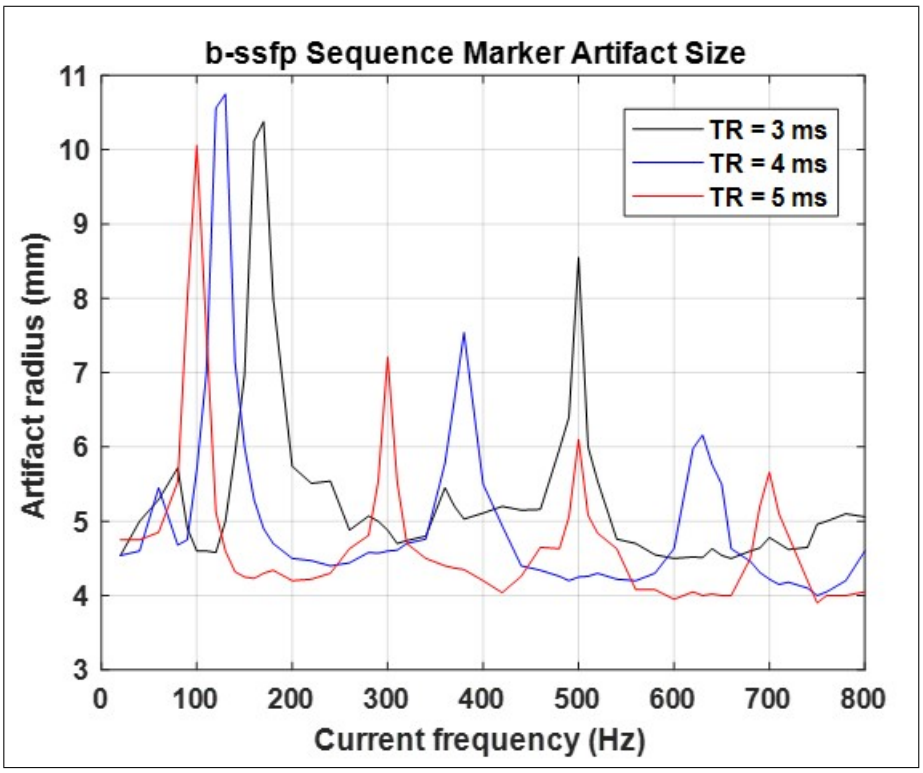

Figure 4.12 Marker artifact sizes with respect to applied AC frequency for different TR values using b-SSFP sequence.

applied during a b-SSFP scan with 5 ms repetition time. Therefore, the frequency of alternating current that will form the largest and most conspicuous artifacts can be directly related to the sequence TR value because there is only one echo (read-out) in every TR.

In Figure 4.13, a sample T2-weighted TSE pulse sequence diagram and below the diagram 2 different current types that were applied to the markers separately with respect to the pulse diagram during T2-weighted TSE imaging are given. Alongside the sample TSE pulse diagram, the resulting sagittal MR images of the solenoid coil marker artifacts are shown in the figure. The MR image placed on top resulted from the application of 10 mA continuous direct current to the conductive ink-printed markers. The MR image placed at the bottom resulted by the application of +/- 10 mA 33 Hz (half the echo-spacing frequency of the sequence) alternating current to the conductive in printed coil markers. The generated distal tip marker artifact sizes were measured as 5.1 mm and 14.6 mm for Direct current and Alternating current respectively.

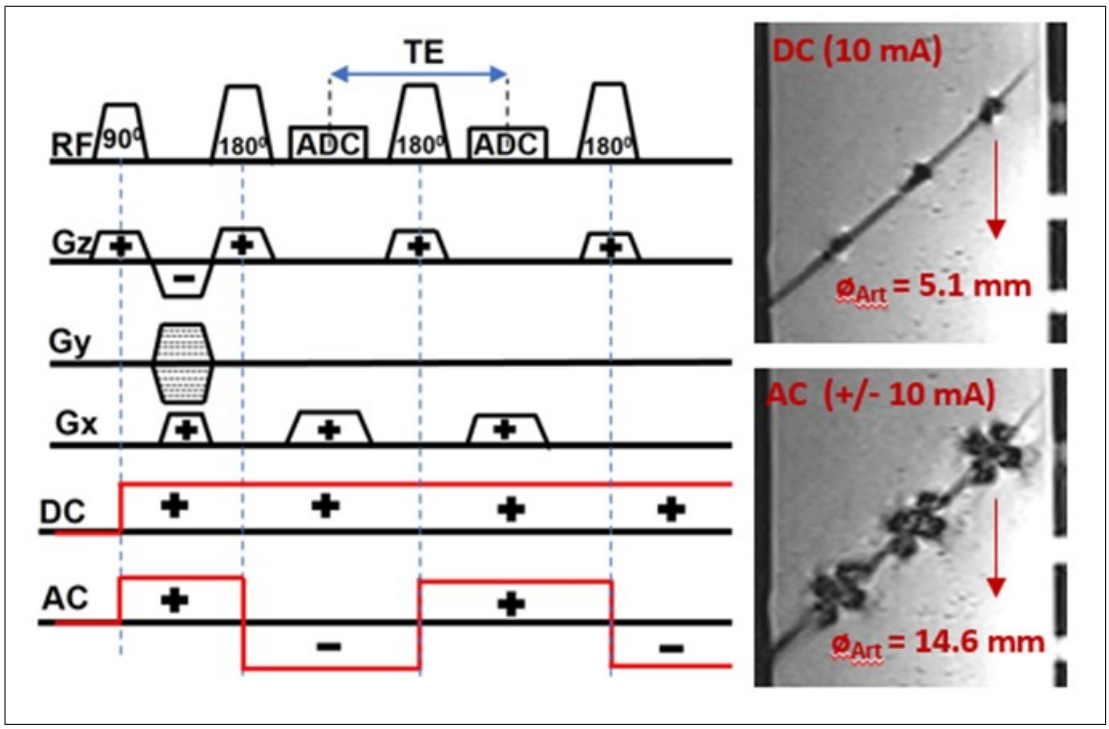

Figure 4.13 Two different applied current types with respect to T2-weighted TSE sequence pulse diagram and resulting MR images of conductive ink printed markers.

It can be seen that changing the direction of the generated external magnetic field every readout period by applying AC instead of DC forms larger artifacts same as b-SSFP sequence. The refocusing 180^0 RF pulses of TSE sequence suppresses constant inhomogeneities on the MR image therefore, inhomogeneities around the markers created by applying a constant DC to the markers get refocused by the refocusing RF pulses of the sequence. On the other hand, by changing the externally introduced local magnetic field direction in every consecutive read-out period (applying AC) the refocusing effect of 180^0 can be canceled and larger and more conspicuous artifacts can be generated.

The effect of applied current amplitude on generated marker artifact sizes using a T2-weighted TSE sequence with 15 ms echo-spacing time with sagittal (first row) and coronal (second row) images of the PEEK prototype are given in Figure 4.14. A continuous AC was applied to the markers with current amplitudes, of 0 mA, +/- 5 mA, and +/- 10 mA from left to right. In the first column of images, the PEEK prototype is visible but not very conspicuous and would be difficult to track in-vivo

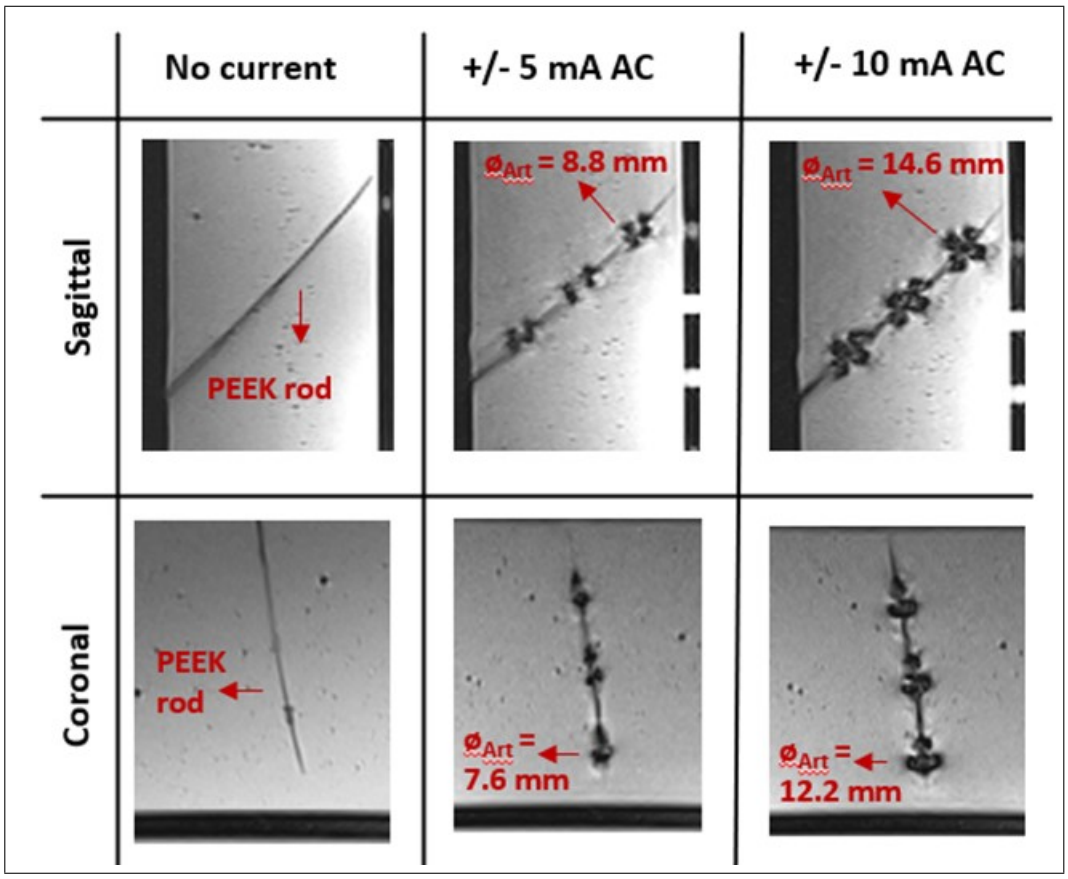

Figure 4.14 Coronal and sagittal T2-weighted TSE images of AC applied conductive ink printed markers and the effect of current amplitude on the marker artifact size.

without any current application to the markers. Applying +/- 5 mA 33 Hz (half of the echo spacing frequency) AC resulted in distal marker artifacts with 8.8 mm and 7.6 mm radii and, applying +/- 10 mA 33 Hz AC resulted in distal marker artifacts with 14.6 mm and 12.2 mm radii in sagittal and coronal images respectively.

After determining the current type (AC/DC) and current parameters that would create the largest artifact and the highest conspicuity for each aforementioned imaging sequence, the current controlled conductive ink-printed marker's capability to increase the visibility of a commercially available MR-compatible catheter was tested under 0.55 T scanner using the optimum current type and parameters.

Figure 4.15 shows conductive ink-printed markers are successfully capable of increasing the visibility of MR-compatible interventional tools using a commercial

catheter. Coronal (first column) and sagittal (second column) images of 5 Fr. a catheter with 1 fiducial marker that is placed at the base of its pigtail using GRE (first row), b-SSFP (second row), TSE (third row) sequences. 50 mA DC was applied to the marker using GRE sequence and generated marker artifact radius measured as 9.9 mm and 10 mm in coronal and sagittal images respectively. +/- 20 mA 166 Hz AC was applied to the marker using b-SSFP sequence with 3 ms repetition time and generated marker artifact radius was measured as 12.9 mm and 13.8 mm in coronal and sagittal images respectively. Lastly, +/- 10 mA 33Hz AC was applied to the marker using TSE sequence with 15 ms echo spacing time, and generated marker artifact radius was measured as 14mm and 11,4 mm in coronal and sagittal images respectively.

Finally, in Figure 4.16, MR images of both the PEEK sample and the commercial catheter are shown using all 3 sequences under a 1.5 T scanner. The radii of the PEEK sample's distal marker artifact and the catheter sample's only artifact are measured and given in the figure. In the first-row GRE images were recorded while applying 50 mA DC to the markers. Artifact sizes were measured as 11.8 mm and 12.2 mm for the PEEK sample and 11.0 mm and 10.8 mm for the catheter for coronal and sagittal images respectively. In the second-row b-SSFP images were recorded while applying +/- 20 mA to the markers. Artifact sizes were measured as 15.7 mm and 15.5 mm for the PEEK sample and 16.6 mm and 16.1 mm for the catheter sample for coronal and sagittal images respectively. In the third-row TSE images were recorded while applying +/- 10 mA to the markers. Artifact sizes were measured as 12.1 mm and 13.6 mm for the PEEK sample and, 12.8 mm and 14.2 mm for the catheter sample for coronal and sagittal images respectively.

4.4 Discussion

One of the key factors preventing the advancement of the interventional MRI field is the high magnetic field environment of MRI. Compared to other imaging modalities like X-ray or CT, there are fewer commercially available interventional instruments that can be utilized for MR-guided procedures.

The interventional MRI device tracking method introduced in this chapter can be used for both commercially available and custom-designed MR-compatible interventional tools across a range of magnetic strengths. It is compatible with commonly used sequences such as GRE, b-SSFP, and TSE sequences which are frequently employed for MR-guided interventions. As expected, these sequences may not fulfill all the imaging requirements of every interventional procedure. GRE and b-SSFP sequences offer rapid imaging capabilities, making them suitable for real-time clinical applications such as device placement into the anatomy and tracking during advancing the device to the target area [161],[162]. The bSSFP sequence, with its ability to distinguish blood flow and blood vessels from surrounding tissue, along with its real-time imaging capability and immunity to motion artifacts, is particularly advantageous for cardiac interventions [146],[147]. Although the T2-weighted TSE sequence is slower compared to GRE and b-SSFP sequences, it is used for interventional procedures that require better resolution and soft tissue contrast [161].

The results of this study indicate that applying AC to conductive ink-printed markers can result in larger marker artifacts in b-SSFP and TSE sequences. Applying a constant DC to the markers creates a consistent external magnetic field around the markers. Although this constant inhomogeneity can still create an artifact, refocusing gradients of b-SSFP sequence and multiple 1800 refocusing pulses of TSE sequence help mitigate the impact of persistent inhomogeneities on the resulting image [118],[119]. In contrast, applying an AC that changes its direction every read-out period of the pulse sequence reverses the direction of the external local magnetic field during every consecutive read-out period. Therefore, the artifacts formed by an alternating current around the markers don't get suppressed by the sequence, leading to their increased visibility.

In image-guided interventions, minimizing alterations to the profile and geometry of interventional devices is crucial for the success of the procedure. By printing solenoid coil markers on polyester heat-shrink tubes, it becomes feasible to incorporate markers to various interventional tools such as catheters, guidewires, or needles with minimal profile alterations. This proposed approach eliminates the need for winding

disruptive conductive wires around interventional devices, resulting in a smoother overall profile. Additionally, it eliminates the risks associated with the shearing of marker components and potential damage to surrounding tissue.

The introduced device tracking method represents a significant advancement in the field of interventional MRI, offering several key benefits compared to other tracking methods. Firstly, it provides a simple and compact solution to address the poor conspicuity problem commonly encountered with many MR-compatible instruments. Secondly, it is compatible with all 3 sequences used commonly for MR-guided interventions by adjusting the supply current. Thirdly, the marker artifact size can be controlled to align with the specific needs of the procedure, unlike passive markers. It can facilitate device tracking by enlarging the marker artifacts during interventional device implantation towards the target area and it doesn't block the anatomical image underneath the markers by diminishing the marker artifacts or turning them off completely during operations that need high precision.

Same as other conventional marker technologies [163], the orientation of the conductive ink-printed markers with respect to the main magnetic field of the scanner affects the marker artifact size. However, the introduced method can allow us to minimize the effect of device orientation on marker artifact size by adjusting the applied current amplitude accordingly. The proposed method is adaptable to different MRI systems with varying magnetic strengths, unlike semi-active markers that need to be tuned to a specific Larmor frequency. Also, it doesn't require device-specific hardware, a connection to a separate receive channel on the scanner, or external image processing software for device visibility, unlike active markers.

Although this method increases the visibility of interventional tools, it can't form colorized artifacts, as it is, around the markers and may limit differentiation from other anatomical susceptibilities during an interventional procedure. As a trade-off for the simplicity of the design, colorized marker artifacts can be generated by using external software or image postprocessing as Eibofner et al. describe using a b-SSFP sequence [119].

Another limitation of the introduced method is the use of a long coaxial cable that carries the supply current to the test sample from the control room. The electrical length of an interventional device is important in the MR environment due to the potential risk of RF-induced heating on the device, which can reach dangerous levels for the patient. As the next step, we have been working on implementing conductive ink-printed markers on an MR-compatible Nitinol needle prototype with a current supply circuit that could work safely in the scanner room without disrupting the MR image. The objective is to shorten the overall electrical length. Once the MR safety phantom tests including RF-induced heating assessments have been conducted under MRI, the current controlled markers can be further evaluated in vivo.

4.5 Conclusion

In this chapter, device tracking markers were designed as solenoid coils and printed on polyester heat-shrink tubes using conductive ink to be placed on MR-compatible interventional tools to increase their visibility under MRI. The visibility performance of current controlled markers was tested using a custom designed 6 Fr. PEEK prototype that contains 3 markers (one in the distal end one in the middle and one in the proximal end of the prototype) and a commercial MR-compatible 5Fr. pig-tail flush catheter that contains 1 marker (right below the catheter's pigtail) under 0.55 T and 1.5 T MRI for GRE, b-SSFP, and TSE pulse sequences. The applied current type and parameters that generate the most conspicuous artifacts were determined by comparing the artifact size formed by the distal marker of the PEEK sample under 0.55 T MRI for each sequence. Marker artifact size control via applied current amplitude adjustments was successful for all 3 sequences as expected.

In a GRE sequence, the size of the generated artifact was not significantly affected by applying DC or AC to the markers. The main difference was that because the direction of externally generated magnetic fields reversed with each TR, the AC-generated artifacts took on a cross-shaped appearance rather than an elliptical one. In both b-SSFP and TSE sequences, when compared to DC-generated artifacts of the same

current amplitude, the AC-generated ones showed significantly higher conspicuity. The effect of the applied current frequency on resulting marker artifact sizes was evaluated in b-SSFP sequence. It is demonstrated that the maximum artifact size was achieved when the current frequency is half of the read-out (echo spacing) frequency of the sequence. Finally, an MR-compatible commercial pigtail catheter is successfully made visible under both 0.55T and 1.5T scanners with the introduced methodology for all 3 aforementioned sequences.

The next chapter introduces the custom-designed MR-compatible needle prototype design and the current supply circuit design that can work safely in the MR environment.

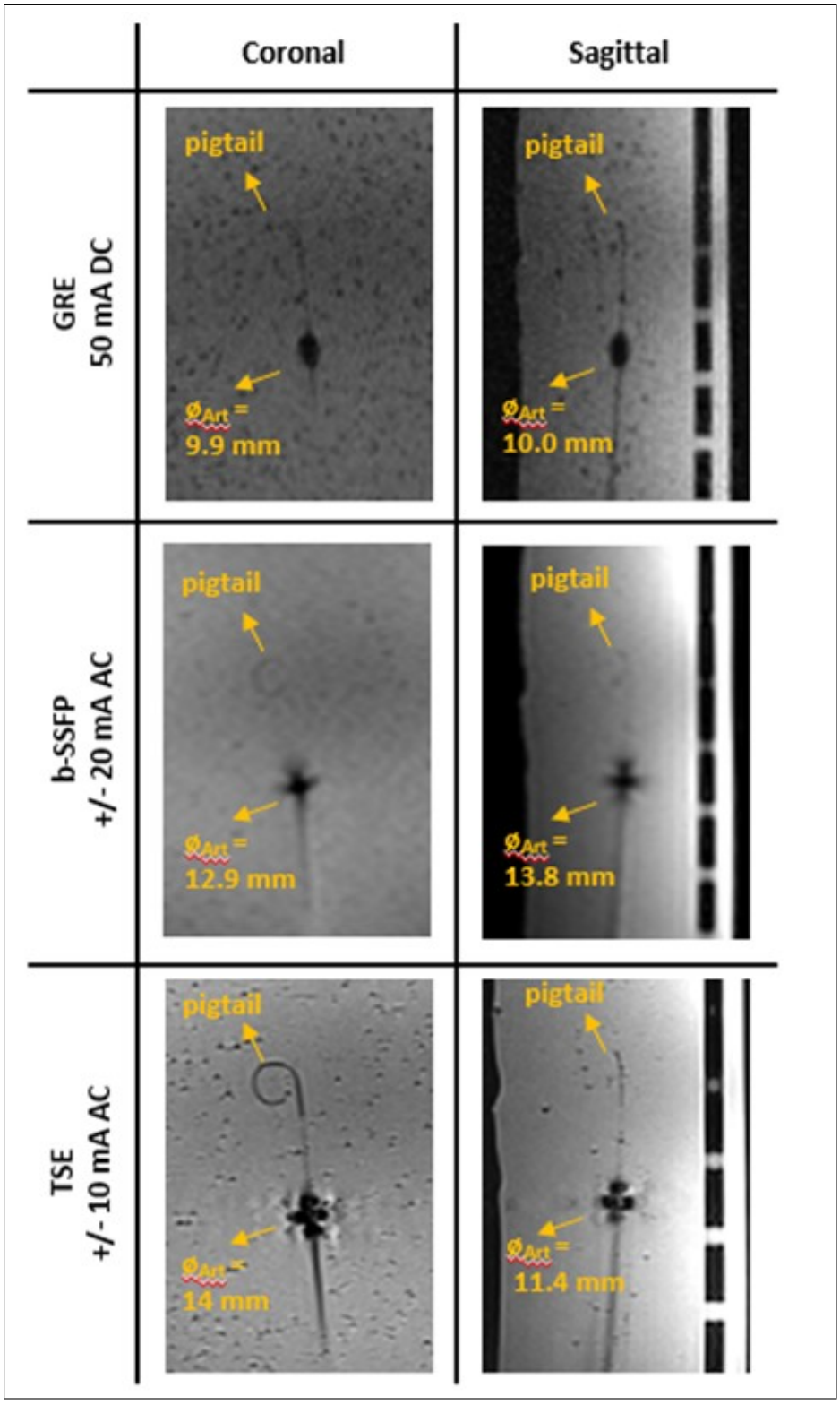

Figure 4.15 Commercial 5 Fr. catheter images with current applied conductive ink printed marker using GRE, b-ssfp and TSE sequences under 0.55T scanner.

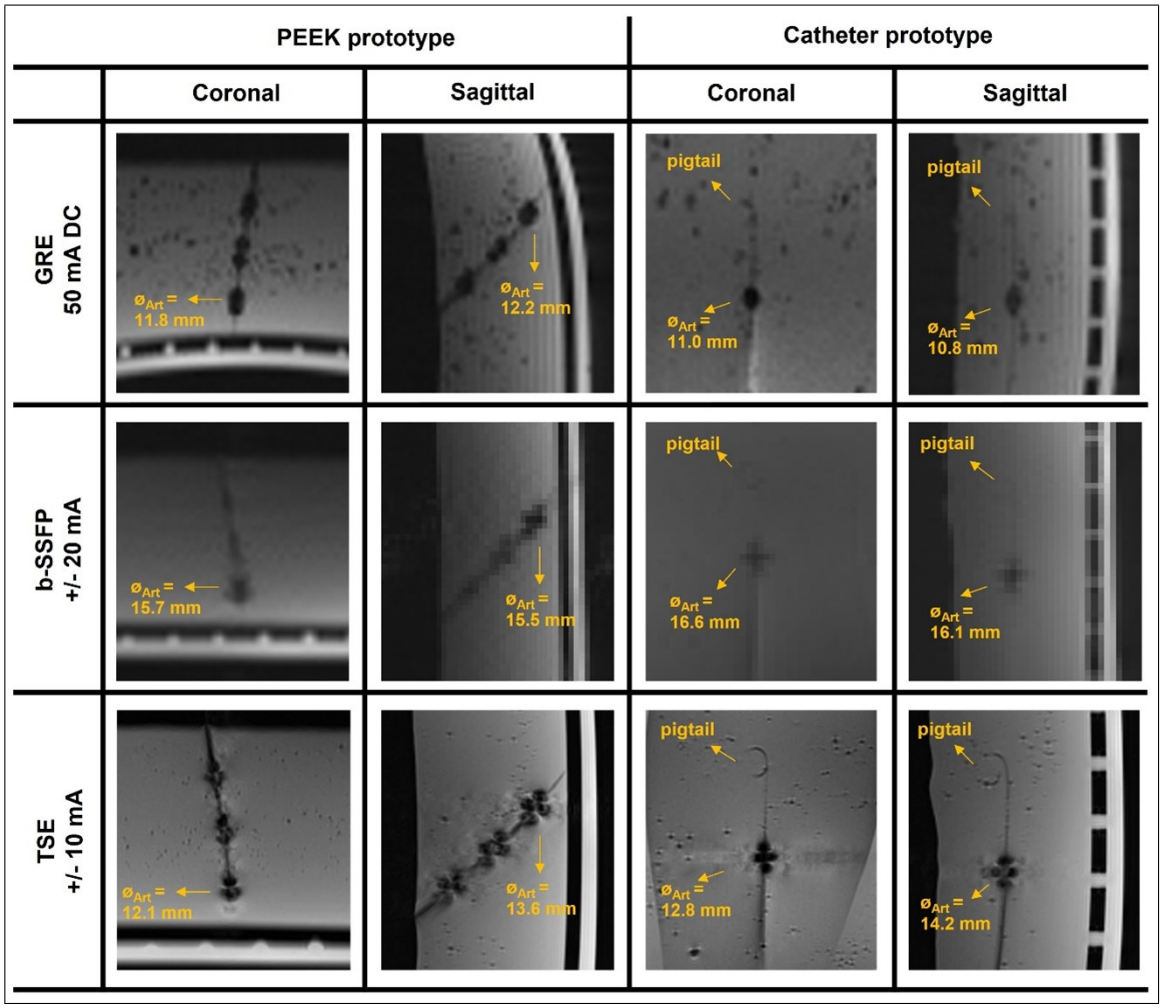

Figure 4.16 1.5 T MR Images of 6 Fr. PEEK rod and 5 Fr. commercial pigtail catheter using GRE, b-SSFP, and TSE sequences. 50 mA DC was applied to the markers for GRE sequence images (first row), +/- 20 mA AC was applied to the markers in b-SSFP sequence images (second row), +/- 10 mA AC was applied in TSE sequence images (third row).

5. 20-GAUGE NEEDLE PROTOTYPE AND SIGNAL GENERATOR CIRCUIT DESIGN FOR CURRENT CONTROLLED NEEDLE TRACKING UNDER MRI

5.1 Introduction

Real-time imaging modalities such as X-ray fluoroscopy, computed tomography (CT), ultrasound, and magnetic resonance imaging (MRI) have improved, allowing for therapeutic and interventional diagnostic minimally invasive procedures to be performed with precise image guidance [164]. What distinguishes MRI from other imaging modalities is its absence of ionizing radiation and its ability to provide excellent soft tissue contrast and fast multiplanar imaging with high spatial resolution [22]-[27]. The challenge of designing custom interventional tools such as catheters guidewires or needles that are visible under MRI and safe when exposed to radio frequency (RF) radiation and a strong magnetic field remains, and it is the trade-off for MRI's many benefits.

Different techniques were devised to increase the visibility of MR-compatible interventional instruments by placing active, passive, or resonant tracking markers on interventional devices, and each of them has advantages and drawbacks [109]-[112],[114]-[116]. Active markers use miniature receiving coils to detect the MRI signal in their immediate vicinity and deliver the signal to the scanner via an independent receiver channel. As a result, the active markers can be tracked by superimposing the marker signal on top of the anatomical image by an external software. Despite their high conspicuity under MRI, active markers are difficult to design, magnetic field strength dependent, they need to be connected to the scanner's receive channel via a device-specific hardware and they require an external software [111],[112],[158],[159].

Passive markers take advantage of the inhomogeneities in the magnetic field created by the susceptibility of the marker material and can generate negative or positive

contrast. Although passive markers are much simpler to design and do not require any additional hardware or software, they may be more challenging to track under MRI [107],[109],[110]. The artifact size generated by the passive markers can't be controlled. Depending on the device orientation relative to the main magnetic field, the artifact size might be too large to view the anatomical image underlying during interventions that require high accuracy or too small to clearly identify over the course of the procedure.

When an MR sequence with a low flip angle is used, resonant markers inductively couple to the scanner's transmit RF coils, and the induced RF current on the markers causes flip angle amplification in the close vicinity, resulting in a bright signal that helps to locate the position of the marker in the image. Resonant markers are easier to design compared to active markers, but they are also magnetic field strength dependent, and the low flip angle sequence can affect the signal-to-noise ratio of the anatomical image [114]-[116],[160].

Another method for device tracking under MRI is introduced by Glowinski et al [117]. Catheter visualization was achieved by applying direct current to the conductive wires placed on the catheter surface. Main magnetic field homogeneity was distorted by the localized external magnetic field formed by current-carrying conductive wires and a negative contrast was formed in Gradient Echo (GRE) images. A similar method was used in another work for device visualization in spin-echo (SE) images using sequence-triggered DC pulses as the supply current [118]. This method allows the user to control the artifact size during the MR-guided procedure by adjusting the applied current. It facilitates device tracking easier by enlarging the marker artifacts and avoids any blockage on the anatomical image by reducing the artifact size or turning it off completely when necessary.

In the previous chapter, it was shown that miniature solenoid coil markers can be printed on polyester heat-shrink tubes and these heat-shrink tubes can be placed onto custom-made or commercially available MR-compatible interventional devices and can be used as current controlled markers to increase the devices' visibility under MRI. The current type and current parameters that should be applied to the conductive

ink printed markers to form conspicuous, trackable, and controllable artifacts using Gradient-echo, Turbo Spin-echo, and balanced steady-state free precession sequences were determined. In this chapter, a custom 20-gauge nitinol needle prototype that contains 3 coil markers and, a current supply circuit that can be safely used in the MRI environment without disrupting the MR image was designed. The needle prototype and the current supply circuit were tested via in-vitro imaging and safety experiments under MRI and finally, an in-vivo animal experiment was performed.

5.2 Methods

5.2.1 Custom needle and miniature coil design

Miniature coil markers were designed and placed on custom MR-compatible nitinol (Memry Corp CT) needle prototypes, that are 10 cm long (OD: 0.75 mm), using a conductive ink printer system that was built in our earlier work [28]. 3 markers were placed on the needle at the distal tip, middle, and proximal end of the needle to provide accurate tip and shaft location information. Conductive paths and solenoid coils, which will act as 3 tracking markers, were printed on heat shrink polyester tubes (ID: 0.050", wall thickness: 0.0006", Advanced Polymers, NH) using silver conductive ink (AG-500, Kayaku Advanced Materials, MA) as shown in figure 5.1. Two layers of the polyester tube, each of them containing 30 mm apart 3 solenoid coils, were sleeved and heat shrunk (hot air station 210-A BEAHM Design inc.) around the needles. Coil markers printed on the first and the second layer of polyester tubes were wound in the opposite direction so that by placing the coils on top of each other localized magnetic field created by the coil markers, via passing electrical current on them, can be superimposed, and increased. All the markers were designed identical in any other way. Each marker was designed as 3 mm long solenoid coils with a conductive line width of 150 μm and a line thickness of 15 μm. Solenoid coils have a diameter of 830 μm and 920 μm on the first layer and the second layer respectively.

Conductive lines on the first and second layer of heat shrink tubes were elec-

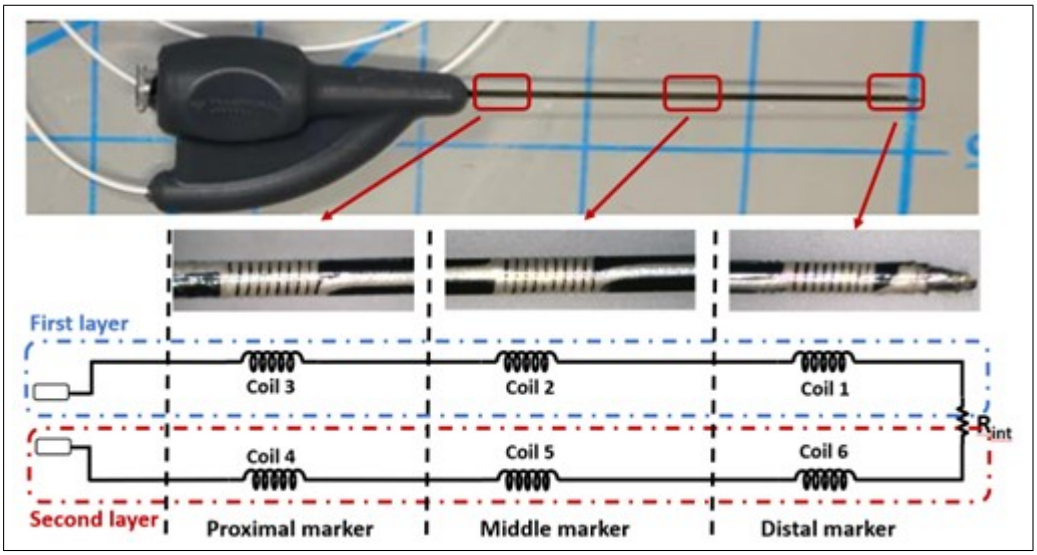

Figure 5.1 Needle prototype with markers and Electrical representation schematics of the conductive ink printed markers.

trically connected using conductive ink at the distal tip of the needle completing the current controlled marker circuit. 1mm long marker bands were cut (Laser make, model) from a nitinol hypo tube (Memry Corp CT, ID:0.864mm and OD: 0.965 mm) were used for providing the connection between the printed circuit on the needle and the coaxial cable that will carry the supply current to the needle. Two marker bands were placed on the first and second layer of the marker circuit at the proximal end and the connection was ensured by using conductive silver epoxy between the rings and the conductive ink printed lines after soldering the rings to the inner and outer conductors of the 36 AWG coaxial cable (9436- WH033, Alpha Wire, NJ). A final heat shrink tube (make model ID OD) was placed on the needle for complete insulation. A small handle consisting of a luer-lock is 3-D printed and placed at the proximal end of the needle providing a protection for the needle-coaxial cable connection point and an easy integration to commercial syringes. The prototype was finalized by soldering a male mmcx connector at the proximal end of the coaxial cable.

5.2.2 Current supply circuit design

An electronic circuit that can supply an AC signal to the needle markers was designed using a microcontroller (Arduino Nano 33 IOT) and a signal generator module (AD9833). The schematics of the circuit design was given in Figure 5.2. An operational amplifier (JRC2021) was used for amplifying the output of the AD9833 module and a potentiometer was used as the gain of the amplifier so that the signal amplitude can be controlled manually. An AC current buffer was designed using 2 BJT transistors so that a current up to 200 mA peak-to-peak (p-p) can be generated if needed. The AC current is supplied to the markers on the needle through a female mmcx connector. The signal generator circuit was powered by non-magnetic lithium polymer MRI-safe batteries (GM-NM103450-PCB, PowerStream, UT) and a power switch is added to the circuit so that the markers can be turned on and off when needed. The circuit allows the user to determine the signal frequency via the microcontroller and adjust the signal amplitude manually using the potentiometer. Finally, the circuit was placed in a custom 3D-printed case and the inner wall of the 3D-printed case was shielded using copper tape.

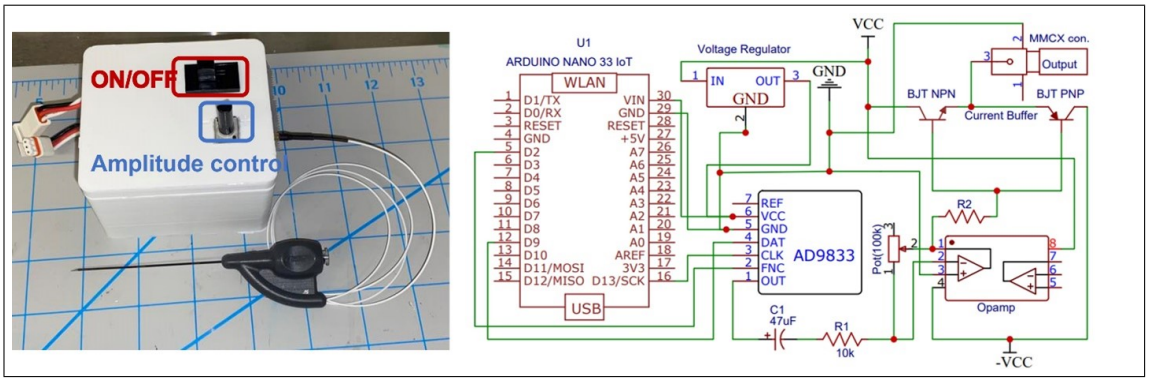

Figure 5.2 Current supply circuit image and circuit schematics

5.2.3 In-vitro experiments

20 G needle prototype with miniature localized current controlled tracking markers were tested under high performance 0.55T MRI scanner (prototype Magnetom Aera, Siemens Healthcare, Erlangen, Germany) for marker visibility and artifact size control

using the marker control circuit using 3 different sequences namely: GRE, TSE, and b-SSFP. The same setup was used under 1.5T MRI scanner (Siemens Magnetom Aera, Siemens Healthcare, Erlangen, Germany) to test the magnetic field dependency of the introduced tracking method. Additionally, RF-induced heating experiments were performed for validating the safety of prototypes.

Current based marker artifact size with respect to the frequency and amplitude of the applied current and performance of the signal generator circuit were tested and current parameters that were determined by the in-vitro experiments in chapter 3 were confirmed via in-vitro experiments using a real time b-ssfp sequence (TE/TR: 2/4 ms, FOV: 399x399 mm^2, bandwidth: 340 Hz/px , matrix: 240x158, slice thickness: 8 mm). The performance of the needle prototype and the current supply circuit were further tested using GRE sequence (Parameters) and T2-weighted TSE sequence (parameters). The needle prototypes were placed at the isocenter of the scanner 450 oblique to the main magnetic field and parallel to the main magnetic field (B0) plane in the gel phantom prepared according to ASTM 2182-19 [123]. Imaging performance of conductive ink printed marker design was tested by applying alternating currents with various current amplitudes to the tracking markers. Marker artifact sizes were measured using a DICOM imaging software (MicroDICOM).

RF-induced heating tests were performed to validate the safety of the current applied needle prototypes. Fiber optic temperature probes (Opsens model ID: OD:) were used for recording the temperature during real-time b-SSFP sequence with different flip angles (45^0, 60^0, 75^0) and hence different SAR(2.74 W/kg, 3.58 W/kg, 3.95 W/kg) values. Polyimide tubes were fixed alongside needle by polyester heat-shrink tubes and fiber optic temperature sensors (Opsens OTG-M170) were placed inside the polyimide ports. Needles were placed at the isocenter of the scanner making 45 degrees with the Z axis and 2 cm away from the right edge of the gel phantom (High SAR area according to the ASTM standard). Heating profile along the needle is recorded by pulling the temperature probe back slowly in a constant speed starting from the distal end to the proximal end during 75^0 flip-angle b-SSFP scan to determine the hot spot (the spot on the needle that heats up the most) of the needle. Static heating

experiments were performed by recording the temperature change from the needle's hot spot during 90 second scans using b-SSFP sequence with different flip angles (45^0, 60^0, 75^0). Finally, a 10-minute static heating experiment is performed with 75^0 flip angle to observe the long-term temperature change.

5.2.4 Post-mortem animal experiments

Mechanical and MRI visibility performance of the needle prototypes were tested in vivo under real-time MRI guidance. The needle prototypes were inserted into the liver of a deceased swine. MR images of the prototype needle in the liver tissue were recorded and the marker artifact sizes were measured. The signal generator circuit was turned off next and the image of the needle without the markers was captured in the same location. The signal generator circuit was modified by programming the microcontroller to turn on and off with 2-second intervals to create "blinking" markers during the rest of the experiment. Video files of needle insertion into the liver and blinking marker artifacts were generated using DICOM images.

The same real-time b-SSFP sequence as in vitro experiment was used during in vivo experiments as well and MonteCarlo interactive interface was used for interactive plane selection throughout the experiment. In order to reduce the use of animals, the experiment was conducted following another non-survival porcine experiment. Animal experiments were approved by the National Heart, Lung and Blood Institute (NHLBI) Animal Use and Care Committee and performed according to the contemporary National Institutes of Health standards.

5.3 Results

5.3.1 In-vitro experiments

Figures 5.3 and 5.4 show the in vitro MR images of the needle prototype with respect to different frequency and amplitude values of applied current to the conductive ink printed markers using b-SSFP sequence. The applied alternative current generates an external local magnetic field around the solenoid coil markers and creates a controllable negative contrast on the image by introducing a non-constant offset to the gradient fields. It is shown in Figure 5.3 that the largest marker artifacts can be obtained when the current was applied with a frequency exactly half of the repetition frequency (When TR = 5ms, repetition frequency = 200Hz applied current frequency = 100Hz) of the b-SSFP sequence. The artifact size decreases as the applied current frequency value moves away from the ideal frequency. Figure 5.4 shows the effect of the current amplitude on the marker artifact size. It can be seen that the artifact size increases with the amplitude of the current and the artifacts disappear when the signal generator circuit is switched off as expected.

In figure 5.5 you can see the contrast comparison between the alternating current controlled marker artifact and a passive marker artifact. 100 mg Iron-oxide powder (Fe_2O_3) was mixed with 1 ml. of UV curable adhesive and was spread and cured on the needle tip so that a 3 mm long (same length as the current controlled solenoid coil marker) passive marker to create the passive marker artifact on the MR image. Figure x.a and b shows the sagittal and the transversal images of the artifact formed by the passive marker respectively. Figure x.c and d shows the sagittal and transversal images of the current controlled artifact images respectively. Using the transversal images of both of the markers contrast to noise ratio of the images are calculated for a quantitative comparison between the passive and the current controlled markers. The contrast to noise ratio of the passive marker is calculated as -1.1 and the contrast to noise ratio of the current controlled artifact is calculated as -1.3. Because we are comparing negative contrasts smaller valued current controlled artifacts shows a better performance. The contrast to noise ratio of the artifact images are calculated by subtracting the mean

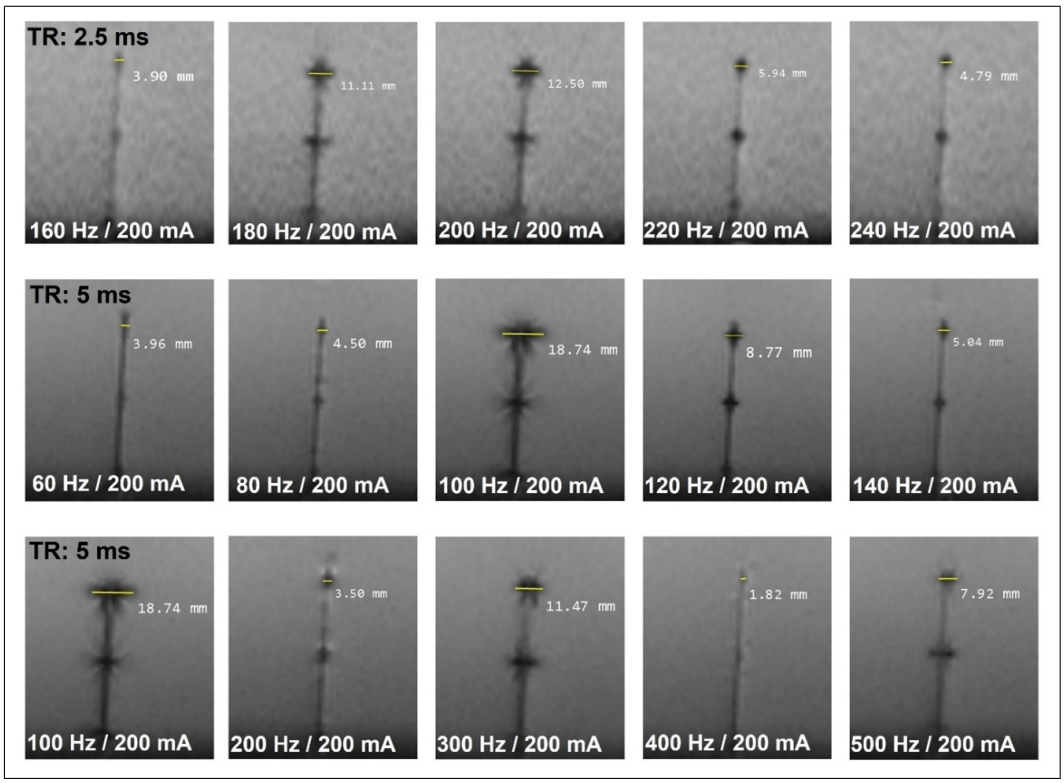

Figure 5.3 In vitro marker artifact sizes with respect to TR value of the b-ssfp sequence and frequency of the applied current

phantom pixel values from mean artifact pixel values and dividing the resulting value to the mean noise value of the image.

Figure 5.6 shows MR images of the needle prototype that contains current applied conductive ink printed solenoid coil markers using GRE and T2-weighted TSE sequences. The current parameters that were determined in Chapter 3 for forming conspicuous artifacts were used for both GRE and T2-weighted TSE images. 60 mA AC with a frequency of 5 Hz was applied to the conductive ink printed markers for the GRE image that has a TR value of 100ms and 10 mA and 20 mA AC with a frequency of 33 Hz was applied to the conductive ink printed markers for the T2-weighted TSE images that have an echo spacing value of 15 ms.

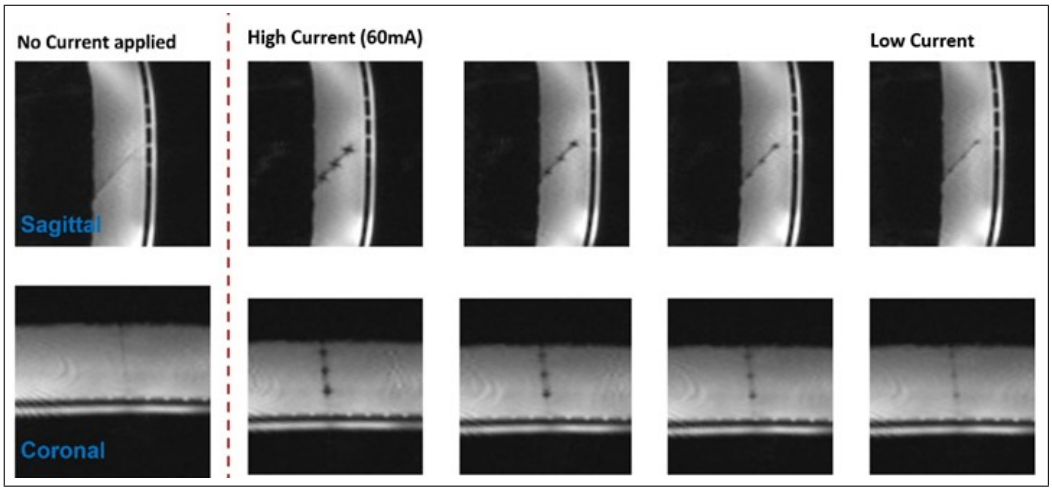

Figure 5.4 In vitro needle prototype images and the effect of current amplitude to marker artifacts.

5.3.2 Post-mortem animal experiments

Post-mortem MR images of the needle prototype inserted in the liver tissue with real-time MRI guidance are given in figure 5.8. It can be seen that the marker artifacts disappear when the signal generator circuit was turned off and the conspicuity of the needle drastically diminishes. The dark vertical lines on the images have resulted from cross-plane signal saturation of intersecting slices during real-time capture with MonteCarlo interactive interface software.

5.3.3 Discussion

Earlier studies in the literature have demonstrated that device tracking can be accomplished via forming a negative contrast by applying continuous direct current to conductive markers while using a GRE sequence [117] or by applying transient direct current and image postprocessing while using an SE or b-ssfp sequences [118],[119]. In this work it was shown that employing alternating current with a frequency that is exactly half of the repetition frequency of a b-SSFP sequence gives the best results without any image postprocessing or any need for an external connection between the scanner and the interventional device. Additionally, applying alternating current with

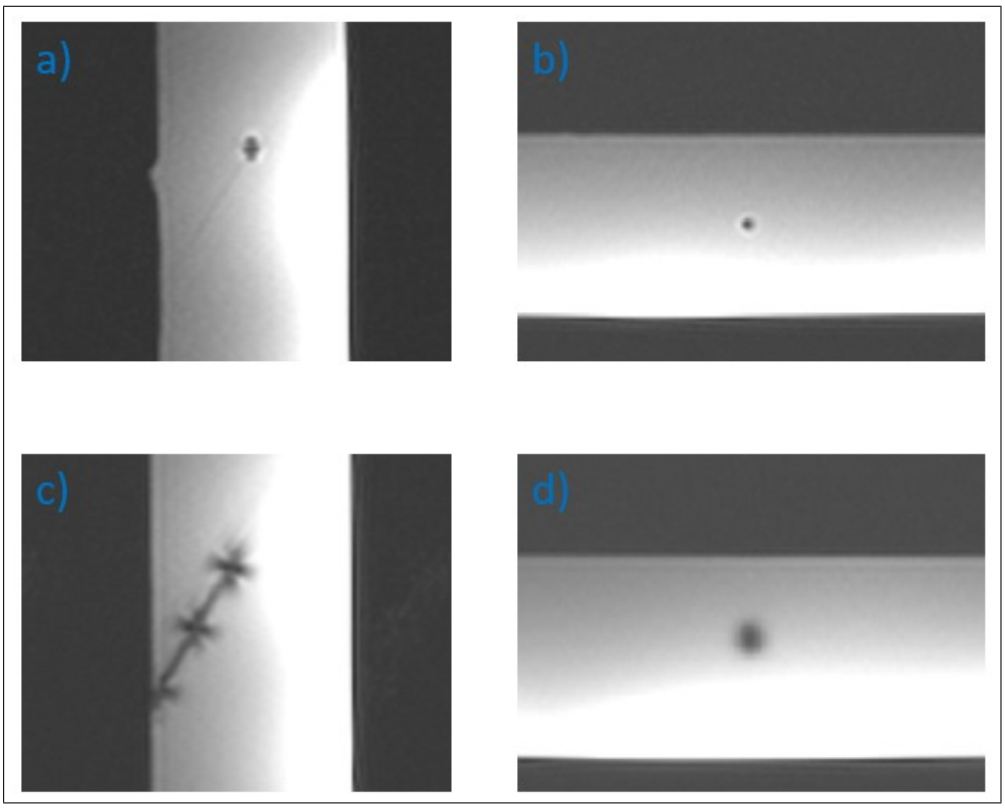

Figure 5.5 Passive and current controlled marker comparison

a frequency that is exactly half of the echo frequency of a turbo Spin-echo sequence and applying either a continuous DC or AC with a frequency half of the repetition frequency of a Gradient-echo sequence results in marker artifacts with high conspicuity. The frequency and the amplitude of the AC signal can be adjusted using the custom-designed signal generator circuit therefore, device tracking can be accomplished for different sequences and the marker artifact size can be adjusted in accordance with the procedure.

Being able to adjust the artifact size is a significant advantage of this method over passive markers because the anatomical image underneath the interventional device can be observed without any external artifact by decreasing the applied AC signal amplitude. Although the introduced method is not capable of forming colorized marker artifacts that are as conspicuous as active markers, it is simpler to design and easier to use. The introduced method does not require an external software, a device specific hardware or a separate receive channel to connect to the scanner. Both active and

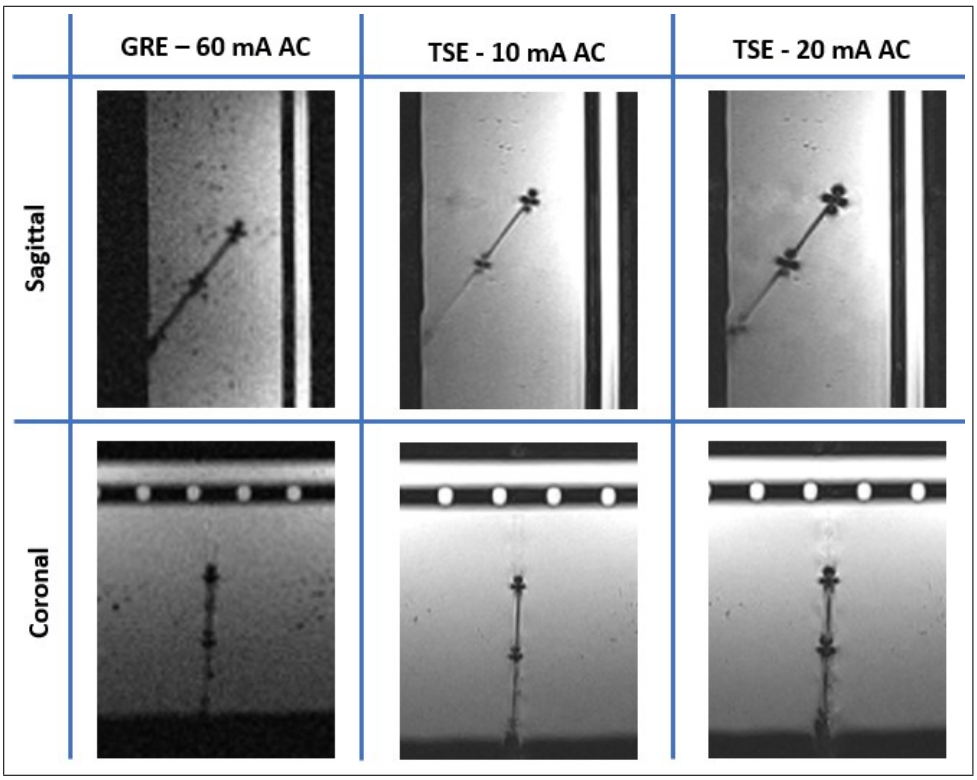

Figure 5.6 Current applied needle prototype images using GRE and TSE sequences.

semi-active(resonant) devices need to be tuned to the Larmor frequency of the MRI scanner. Therefore, they can only be used under one specific magnetic field strength. On the other hand, current controlled markers are not Larmor frequency dependent and can be used in various MR scanners with different strengths as shown in this work for 0.55T and 1.5T scanners.

The size of interventional devices and a smooth outer profile without lumps can be crucial for the safety and success of the procedure. Designing solenoid coil markers by printing conductive ink on heat-shrink polyester tubes instead of winding copper wires on interventional devices keeps the increase of the device thickness to a minimum and results in a smoother outer profile. Another advantage of this method is conductive ink-printed heat shrink tubes can be sleeved and fixed on any interventional tool such as catheters, guidewires or needles. Therefore, using the same signal generator circuit, any commercial or custom-made MR-compatible interventional device can be made visible under MRI.

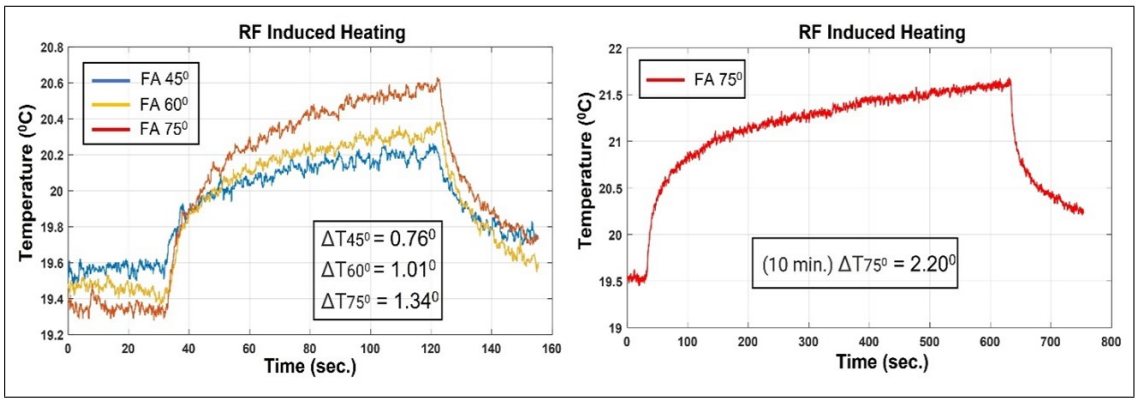

Figure 5.7 RF induced heating measurement of the needle prototype.

RF-induced heating is one of the main issues concerning the safety of interventional devices under MRI. The temperature rise of elongated metallic devices under RF exposure can be high enough to cause a tissue damage. The results of RF-induced heating tests that were performed according to the ASTM standard [123] showed 1.34^0C rise during a 90-second scan and 2.20^0C rise during a 10-minute scan under the worst-case scenario (with the highest possible flip angle and SAR value). The temperature rise caused by the applied current to the conductive ink-printed markers without the RF exposure was recorded as 0.2^0C after 10 minutes. The increase in temperature at the hot spot of the needle prototype is within clinically acceptable limits. Finally, the electrical safety of the prototype is ensured by entirely insulating the needle with the final layer of polyester heat-shrink tube and the 3D printed hub.

5.3.4 Conclusion

In this study, AC-controlled, conductive ink-printed coil markers to be used in real-time MRI-guided procedures is developed as a method for improving the visibility of MR-compatible interventional devices. A low-profile custom nitinol needle is used, as an interventional tool, to test the performance of the introduced methodology. The visibility of the needle is tested under both 0.55T and 1.5T MRI scanners using b-SSFP sequence. Marker artifact control is tested with in-vitro experiments under a 0.55 T scanner using the custom signal generator circuit. In both in vitro and in

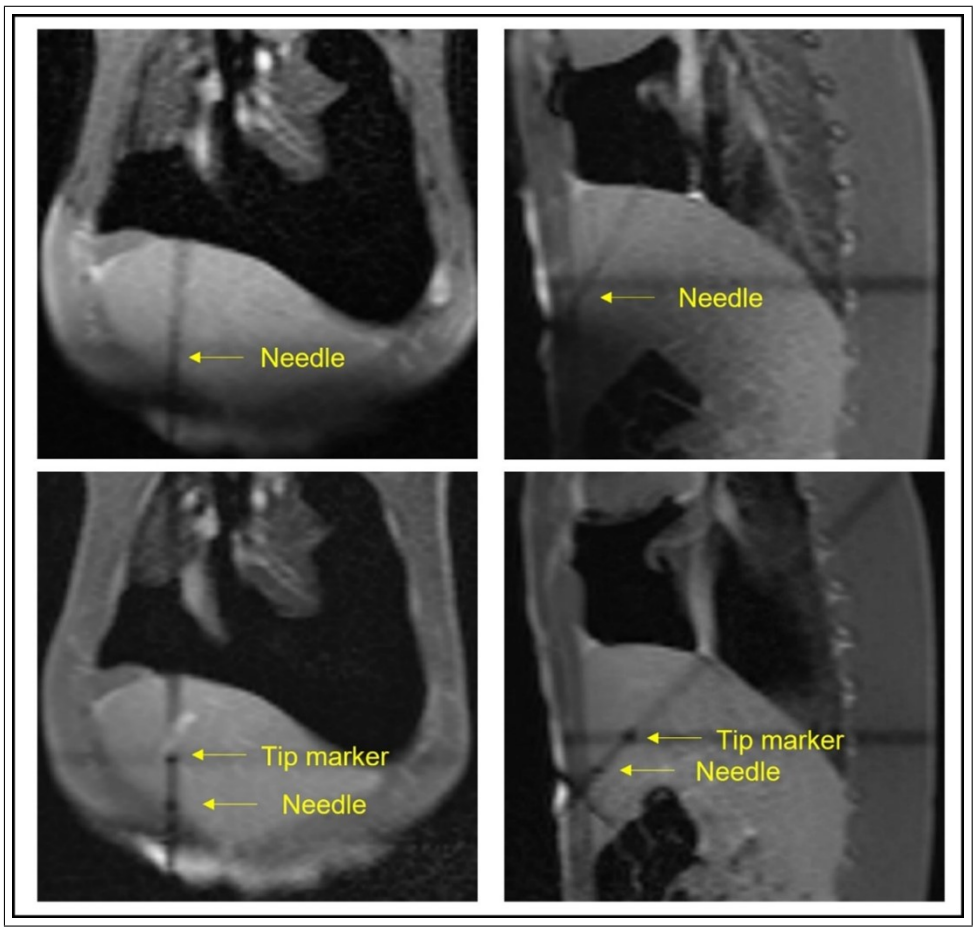

Figure 5.8 Post-mortem needle prototype images.

vivo experiments under MRI, the conspicuity of the MR-safe nitinol needle prototype was clearly increased. RF-induced heating experiments showed that the maximum temperature change was 1.34^0C after 90-second using 75^0 FA at the hot spot of the prototype was under clinically accepted levels.

6. GENERAL CONCLUSION AND FUTURE WORK

In this thesis study novel device technologies that could improve the field of MR-guided needle interventions, particularly biopsy operations, were introduced and tested via in-vitro and in-vivo experiments. Minimally invasive operations are replacing conventional open surgical methods with advantages such as reduced post-operative discomfort for the patient, decreased recovery time, decreased infection risks, reduced total cost of medical care, and so on. Combining these great advantages of minimally invasive operations with image guidance of MRI that could provide to physicians with excellent soft tissue contrast, real-time imaging with a high signal-to-noise ratio, and multiplanar imaging in an ionizing radiation-free environment can increase the success of the operations significantly.

The use of conventional interventional tools for MR-guided procedures is constrained by safety issues that can arise from the high static magnetic field (main magnetic field B_0) of the MRI environment and the RF-induced heating on metallic interventional devices that can be caused by the dynamically changing electromagnetic fields (gradient fields and RF pulses) of the MRI. Furthermore, MR-safe custom designed, or commercially available interventional devices have very poor conspicuity under MRI therefore, it is challenging to visualize and track these devices during the course of MR-guided interventions. These challenges of performing minimally invasive procedures with MRI guidance make it necessary to develop new methodologies for device localization and tracking under MRI for increasing the safety and success of the operations. This thesis study has successfully achieved its three main objectives that could improve the field of interventional MRI.

The first objective of this study was to design a novel, small, compact, and MR-compatible force sensor that could be integrated into the needle tip to provide a tactile feedback and a needle tip location information by measuring the real-time axial force that is applied to the needle tip during needle insertion into the target

tissue. This objective was achieved by designing a Fabry-Perot interferometry-based fiber optic force sensor with the enhanced resolution by titanium coated secondary mirror surface and improved design for an easier fabrication. The FPI-based sensor probe was integrated at the tip of an 18-gauge biopsy needle. According to the benchtop experiments, the introduced FPI-based force sensor was capable of measuring forces up to 20 N with a resolution of 0.03 N.

The sensor was successful at detecting small changes in the applied axial force to the needle tip, this way the physician can appreciate the small changes in the mechanical properties of different tissue types along the needle insertion trajectory using the tactile feedback that is provided by the needle tip force sensor. Further benchtop experiments showed that the introduced fiber optic force sensor was capable of detecting different tissue types by measuring the force during needle insertion into different tissue types such as chicken breast, beef and bovine fat tissues. Additionally, it was demonstrated that the fiber-optic force sensor was successful at measuring the stiffness of gelatin test samples that have different elastic modulus values. Being able to distinguish different tissue types and capability to detect the stiffness level could make cancer diagnosis possible without needing a biopsy sample because it was shown that there is a significant difference between the mechanical characteristics of malignant and benign tissues. It was shown that neither the 18-gauge biopsy needle nor the fiber optic force sensor that was integrated at the needle tip caused any safety issues in the MR environment or any disruption in the MR image by performing phantom experiments under MRI.

The second objective of this study was to introduce a device tracking method that could easily be implemented on custom or commercially available MR-compatible interventional tools, particularly biopsy needles, that could increase their visibility and conspicuity during MR-guided interventions. In chapter 4, electrical current controlled conductive ink printed miniature solenoid coil markers were introduced and successfully increased the device conspicuity using three different MRI pulse sequences namely b-SSFP sequence, GRE sequence and T_2-weighted TSE sequence.

A quantitative analysis was performed, using a custom made 6 Fr. PEEK prototype that contains conductive ink printed markers, to determine the optimal current type and parameters that would form the most conspicuous marker artifacts for each of the aforementioned MR pulse sequences. It was shown through in-vitro experiments, for both b-SSFP and T2-weighted TSE sequences applying an alternating current with a frequency that is half of the echo frequency of the pulse sequences can form significantly larger artifacts. For GRE images it was demonstrated that using either alternating or direct current can form conspicuous marker artifacts. The artifact size control by controlling the applied current amplitude was successful for all three sequences. The capability of introduced device tracking method using conductive ink printed markers to increase the visibility of MR-compatible commercially available interventional tools was successfully demonstrated using a 5 Fr. pigtail flush catheter. Performing in-vitro visibility experiments under both 0.55 T and 1.5 T MRI scanners for all three sequences showed that the introduced device tracking method is independent of the Larmor frequency or magnetic strength of the MRI scanners.

The third and the final objective of this study was to introduce a custom designed MR-compatible 20-gauge nitinol needle prototype that contains current controllable conductive ink printed markers and a current supply circuit that could be safely used in the MR environment without causing any disruption on the MR image. The needle prototype and the current supply circuit that could be used in the MR-environment was successfully designed and introduced in chapter 5.

The needle prototype contained 3 conductive ink printed markers and the current supply circuit was capable of providing an alternating current to those markers with an adjustable amplitude up to +/- 60 mA and a frequency up to 12.5 MHz. It was shown that the conspicuity of the custom designed nitinol needle prototype was increased significantly by connecting it to the current supply circuit and adjusting the applied current according to the current parameters that was determined in chapter 4 with respect to the MRI pulse sequence. RF-induced heating experiments were performed on the current applied needle prototypes under MRI and after showing that the RF-induced temperature rise doesn't reach dangerous levels the needle prototype and

the current supply circuit was tested further in-vivo with an animal experiment. An interactive b-SSFP sequence was used during the in-vivo experiment and the needle was inserted into the liver tissue of a pig. The conspicuity of the needle prototype was successfully increased by applying an alternating current with predetermined parameters to the conductive ink printed markers using the current supply circuit.

As a summary, the safety and the success of MR-guided biopsy operations can be increased by using the introduced novel device technologies and methodologies throughout this thesis study. This study showed that a biopsy needle can be custom designed using an MR safe material such as nitinol. An FPI based fiber optic force sensor can be integrated into the designed biopsy needle and provide real-time tactile feedback, needle tip location information and information about the tissue stiffness to the physician without causing any safety problems during an MR-guided procedure. Additionally, by placing conductive ink printed markers on the needle and using the current supply circuit, the MR-safe needle prototype can be made visible and trackable during biopsy operations under MRI in many clinical setups. The size of the marker artifacts can be controlled and adjusted with respect to the needs of the procedure, which is another great advantage of the introduced method.

In the future, the current controlled device tracking makers can be improved further by colorizing the marker artifacts using image post processing and the markers can be made more conspicuous this way. To be able to colorize the marker artifacts by image processing, the negative contrast formed by the externally generated local magnetic fields should be distinguished from the negative contrast formed by the anatomical susceptibilities. This can be achieved by creating a mask that can be overlayed onto the anatomical MR image like Eibofner et al [119] do in their work. Another way to distinguish the marker artifacts from the anatomical susceptibilities could be using the blinking artifact that was achieved by programming the current supply circuit in chapter 5. After achieving to form colorized marker artifacts by image post processing a superior biopsy needle, that could be safe and visible under MRI and could provide a needle tip force feedback, will be custom designed using a nitinol hypo tube and integrating the FPI based fiber optic force sensor and the current controlled device

tracking markers together.

APPENDIX A. Publications

A.1 Journal Publications

A.1.1 First Author

1. Uzun D, Ulgen O, and Kocaturk O, "Optical force sensor with enhanced resolution for MRI guided biopsy." IEEE Sensors Journal 20.16, 2020: 9202-9208.

2. Uzun D, Yildirim DK, Bruce CG, Halaby R, Jaimes A, Potersnak A, Ramasawmy R, Campbell-Washburn AE, Lederman RJ, Kocaturk O, "Interventional device tracking under MRI via alternating current controlled inhomogeneities. In progress for Magn. Reson. Med. (MRM)

A.1.2 Not first author

1. Ulgen NO, Uzun D, and Kocaturk O, "Phantom study of a fiber optic force sensor design for biopsy needles under MRI." Biomedical optics express 10.1 2019: 242-251.

2. Yildirim DK, Bruce C, Uzun D, Rogers T, O'Brien K, Ramasawmy R, Campbell-Washburn AE, Herzka DA, Lederman RJ, Kocaturk O, "A 20-gauge active needle design with thin-film printed circuitry for interventional MRI at 0.55 T." Magnetic resonance in medicine 86(3), 2021: 1786-1801.

3. Yildirim DK, Uzun D, Bruce C, Kahn TM, Rogers T, Shenke WH, Ramasawmy R, Campbell-Washburn AE, Herzka DA, Lederman RJ, Kocaturk O, " An interventional MRI guidewire combining profile and tip conspicuity for catheterization at 0.55 T" Magnetic resonance in medicine 89(2), 2023: 845-858.

4. Bruce CG, Yildirim DK, Kolandaivelu A, Khan JM, Rogers T, Uzun D, Jaimes AE, Halaby RN, Herzka DA, Babaliaros VC, and Greenbaum AB, "EDEN (Elec-

trocardiographic Radial Depth Navigation): A Novel Approach to Navigate Inside Heart Muscle." JACC: Clinical Electrophysiology, 2023.

A.2 International Conference Proceedings

1. Uzun D, Ulgen O, and Kocaturk O, "FPI-based force sensor for prostate biopsy needle interventions under MRI." In Optical Fiber Sensors 2018, Lausanne, September, (p. ThE6). Optica Publishing Group.

2. Uzun D, Ulgen O, and Kocaturk O, "Evaluation of FPI-based custom force sensor design for biopsy needles." The International Society for Magnetic Resonance in Medicine (ISMRM) 27th Annual Meeting & Exhibition, Canada, 11-16 May 2019.

3. Uzun D, Kocaturk O, "Enhanced FPI-based force sensor designed for MR-compatible biopsy needle." The International Society for Magnetic Resonance in Medicine ISMRM & ISMRT Virtual Conference & Exhibitions, 08-14 August 2020.

4. Uzun D, Yildirim DK, Ramasawmy R, Potersnak A, Campbell-Washburn AE, Lederman RJ, Kocaturk O, "Real-time Needle Tracking Under 0.55T MRI Using Current Controlled B1 Field Artifacts." The International Society for Magnetic Resonance in Medicine ISMRM & ISMRT Virtual Conference & Exhibitions, Canada, 03-08 May 2023.

REFERENCES

1. Galloway, R. L., "The process and development of image-guided procedures," *Annual Review of Biomedical Engineering*, Vol. 3, no. 1, pp. 83–108, 2001.

2. Peters, T. M., "Image-guided surgery: from x-rays to virtual reality," *Computer Methods in Biomechanics and Biomedical Engineering*, Vol. 4, no. 1, pp. 27–57, 2001.

3. Taylor, R. H., and L. Joskowicz, "Computer-integrated surgery and medical robotics," *Standard Handbook of Biomedical Engineering and Design*, pp. 325–353, 2002.

4. Han, B. K., M. D. Schnall, S. G. Orel, and M. Rosen, "Outcome of mri-guided breast biopsy," *AJR Am J Roentgenol*, Vol. 191, no. 6, pp. 1798–1804, 2008.

5. Saikus, C. E., and R. J. Lederman, "Interventional cardiovascular magnetic resonance imaging: a new opportunity for image-guided interventions," *JACC: Cardiovascular Imaging*, Vol. 2, no. 11, pp. 1321–1331, 2009.

6. Buecker, A., E. Spuentrup, T. Schmitz-Rode, and S. K. et al., "Use of a nonmetallic guide wire for magnetic resonance-guided coronary artery catheterization.," *Investigative Radiology*, Vol. 39, no. 11, pp. 656–660, 2004.

7. Jaffray, B., "Minimally invasive surgery," *Archives of Disease in Childhood*, Vol. 90, no. 5, pp. 537–542, 2005.

8. Palep, J. H., "Robotic assisted minimally invasive surgery," *Journal of Minimal Access Surgery*, Vol. 5, no. 1, p. 1, 2009.

9. Salgado-Nesme, N., O. Vergara-Fernandez, L. A. Espino-Urbina, H. A. Luna-Torres, and A. Navarro-Navarro., "Advantages of minimally invasive surgery for the treatment of colovesical fistula," *Revista de Investigacion Clinica*, Vol. 68, no. 6, pp. 299–304, 2017.

10. Matern, U., and P. Waller, "Instruments for minimally invasive surgery," *Surgical Endoscopy*, Vol. 13, no. 2, pp. 174–182, 1999.

11. Schurr, M. O., A. Melzer, P. Dautzenberg, B. Neisius, R. Trapp, and G. Buess, "Development of steerable instruments for minimal invasive surgery in modular conception," *Acta Chirurgica Belgica*, Vol. 93, no. 3, pp. 73–77, 1993.

12. Bock, M., and F. K. Wacker, "Mr−guided intravascular interventions: Techniques and applications," *An Official Journal of the International Society for Magnetic Resonance in Medicine*, Vol. 27, no. 2, pp. 326–338, 2008.

13. Rogers, T., K. Ratnayaka, J. M. Khan, and A. S. et al., "Cmr fluoroscopy right heart catheterization for cardiac output and pulmonary vascular resistance: Results in 102 patients," *Journal of Cardiovascular Magnetic Resonance*, Vol. 19, no. 1, pp. 1–13, 2017.

14. Brown, M. A., and R. C. Semelka, *MRI: Basic Principles and Applications*, John Wiley & Sons, 2011.

15. Friedman, B. R., J. P. Jones, G. Chavez-Munoz, A. P. Salmon, and C. Merit, *Principles of MRI*, John Wiley & Sons, 1989.

16. Doan, B. T., S. Meme, and J. C. Beloeil, *General Principles of MRI*, Chichester, UK: John Wiley & Sons, 2013.

17. Ella, A., D. A. Barriere, H. Adriaensen, D. N. Palmer, T. R. Melzer, N. L. Mitchell, and M. Keller, "The development of brain magnetic resonance approaches in large animal models for preclinical research," *Animal Frontiers*, Vol. 9, no. 3, pp. 44–51, 2019.

18. Lauterbur, P. C., "Image formation by induced local interactions: examples employing nuclear magnetic resonance," *Nature*, Vol. 242, no. 5394, pp. 190–191, 1973.

19. Hendrick, R. E., "Breast mri: Using physics to maximize its sensitivity and specificity to breast cancer," *Med Phys*, Vol. 31, no. 6, p. 1737, 2004.

20. Haynes, H., and W. Holmes, *The Emergence of Magnetic Resonance Imaging (MRI) for 3D Analysis of Sediment Beds*, Vol. 1 of *Geomorphological Techniques*. Wiley Sons, 2013.

21. Lewin, J. S., S. G. Nour, and J. L. Duerk, "Magnetic resonance image-guided biopsy and aspiration," *Topics in Magnetic Resonance Imaging*, Vol. 11, no. 3, pp. 173–183, 2000.

22. Rogers, T., and R. J. Lederman, "Interventional cmr: Clinical applications and future directions," *Current Cardiology Reports*, Vol. 17, no. 5, pp. 1–9, 2015.

23. Nageotte, S. J., R. J. Lederman, and K. Ratnayaka, "Mri catheterization: Ready for broad adoption," *Pediatric Cardiology*, Vol. 41, no. 3, pp. 503–513, 2020.

24. Ratnayaka, K., A. Z. Faranesh, M. A. Guttman, O. Kocaturk, C. E. Saikus, and R. J. Lederman, "Interventional cardiovascular magnetic resonance: Still tantalizing," *Journal of Cardiovascular Magnetic Resonance*, Vol. 10, no. 1, pp. 1–23, 2008.

25. Guttman, M. A., C. Ozturk, A. N. Raval, V. K. Raman, A. J. Dick, R. DeSilva, P. Karmarkar, R. J. Lederman, and E. R. McVeigh, "Interventional cardiovascular procedures guided by realâtime mr imaging: An interactive interface using multiple slices, adaptive projection modes and live 3d renderings," *Journal of Magnetic Resonance Imaging: An Official Journal of the International Society for Magnetic Resonance in Medicine*, Vol. 26, no. 6, pp. 1429–1435, 2007.

26. Guttman, M. A., R. J. Lederman, J. M. Sorger, and E. R. McVeigh, "Real-time volume rendered mri for interventional guidance," *Journal of Cardiovascular Magnetic Resonance*, Vol. 4, no. 4, pp. 431–442, 2002.

27. Campbell-Washburn, A. E., M. A. Tavallaei, M. Pop, E. K. Grant, H. Chubb, K. Rhode, and G. A. Wright, "Realâtime mri guidance of cardiac interventions," *Journal of Magnetic Resonance Imaging*, Vol. 46, no. 4, pp. 935–950, 2017.

28. Weiss, C. R., S. G. Nour, and J. S. Lewin, "Mrguided biopsy: A review of current techniques and applications," *Journal of Magnetic Resonance Imaging: An Official Journal of the International Society for Magnetic Resonance in Medicine*, Vol. 27, no. 2, pp. 311–325, 2008.

29. Priessnitz, O., "Diagnostic value of biopsy in diseases of the muscles," *Zeitschrift fur Orthopadie und ihre Grenzgebiete*, Vol. 79, no. 4, pp. 726–731, 1950.

30. Reuben, A., "Just a second," *Hepatology*, Vol. 38, no. 5, pp. 1316–1320, 2003.

31. Brower, A. B., "Relationship of nodular goiter to thyroid carcinoma; brief review with a note on the diagnostic role of needle biopsy," *Annals of Western Medicine and Surgery*, Vol. 3, no. 11, pp. 395–397, 1949.

32. Telkka, A., "Bone marrow biopsy," *Duodecim; Laaketieteellinen Aikakauskirja*, Vol. 66, no. 10, pp. 789–792, 1950.

33. Ghobrial, F., and S. Guirguis, "The value of aspiration biopsy in the diagnosis of tumours," *The Journal of the Egyptian Medical Association*, Vol. 33, no. 10-11, pp. 890–900, 1950.

34. Menghini, G., "The needle biopsy of the liver, an effective technical progress," *Scientia Medica Italica. English ed*, Vol. 6, no. 2, pp. 212–229, 1957.

35. De-La-Pena, A., R. J. Cavanaugh, and L. G. Ballard, "Prostatic percutaneous biopsy," *Urologia Internationalis*, Vol. 12, no. 1, pp. 1–5, 1961.

36. Kark, R., and R. Muehrcke, "Biopsy of kidney in prone position," *The Lancet*, Vol. 263, no. 6821, pp. 1047–1049, 1954.

37. Stein, H. L., and J. A. Evans, "Percutaneous transthoracic lung biopsy utilizing image amplification," *Radiology*, Vol. 87, no. 2, pp. 350–350, 1966.

38. Rasmussen, S. N., H. H. Holm, J. K. Kristensen, and H. Barlebo, "Ultrasonically-guided liver biopsy," *Br Med J*, Vol. 2, no. 5812, pp. 500–502, 1972.

39. Hancke, S., H. H. Holm, and F. Koch, "Ultrasonically guided percutaneous fine needle biopsy of the pancreas," *Surgery, Gynecology & Obstetrics*, Vol. 140, no. 3, pp. 361–364, 1975.

40. Haaga, J. R., and R. J. Alfidi, "Precise biopsy localization by computed tomography," *Radiology*, Vol. 118, no. 3, pp. 603–607, 1976.

41. Haaga, J. R., R. J. Alfidi, T. R. Havrilla, A. M. Cooperman, F. E. Seidelmann, N. E. Reich, A. J. Weinstein, and T. F. Meaney, "Ct detection and aspiration of abdominal abscesses," *American Journal of Roentgenology*, Vol. 128, no. 3, pp. 465–474, 1977.

42. Lyu, Y., *Imaging-Guided Brain Biopsies*, pp. 15–24. Imaging of CNS Infections and Neuroimmunology, Singapore: Springer,, 2019.

43. Moche, M., S. Heinig, N. Garnov, J. Fuchs, T. O. Petersen, D. Seider, P. Brandmaier, T. Kahn, and H. Busse, "Navigated mri-guided liver biopsies in a closed-bore scanner: Experience in 52 patients," *European Radiology*, Vol. 26, no. 8, pp. 2462–2470, 2016.

44. Chen, X., C. D. Lehman, and K. E. Dee, "Mri-guided breast biopsy: Clinical experience with 14-gauge stainless steel core biopsy needle," *American Journal of Roentgenology*, Vol. 182, no. 4, pp. 1075–1080, 2004.

45. Orel, S. G., and M. D. Schnall, "Mr imaging of the breast for the detection, diagnosis, and staging of breast cancer," *Radiology*, Vol. 220, no. 1, pp. 13–30, 2001.

46. Spick, C., K. Pinker-Domenig, M. Rudas, T. H. Helbich, and P. A. Baltzer, "Mri-only lesions: Application of diffusion-weighted imaging obviates unnecessary mr-guided breast biopsies," *European Radiology*, Vol. 24, no. 6, pp. 1204–1210, 2014.

47. Mann, R. M., C. K. Kuhl, K. Kinkel, and C. Boetes, "Breast mri: Guidelines from the european society of breast imaging," *European Radiology*, Vol. 18, no. 7, pp. 1307–1318, 2008.

48. Sardanelli, F., C. Boetes, B. Borisch, T. Decker, M. Federico, F. J. Gilbert, T. Helbich, S. H. Heywang-Kobrunner, W. A. Kaiser, M. J. Kerin, and R. E. Mansel, "Magnetic resonance imaging of the breast: Recommendations from the eusoma working group," *European Journal of Cancer*, Vol. 46, no. 8, pp. 1296–1316, 2010.

49. Siegel, R. L., K. D. Miller, H. E. Fuchs, and A. Jemal, "Cancer statistics, 2022," *CA: A Cancer Journal For Clinicians*, 2022.

50. Loeb, S., A. Vellekoop, H. U. Ahmed, J. Catto, M. Emberton, R. Nam, D. J. Rosario, V. Scattoni, and Y. Lotan, "Systematic review of complications of prostate biopsy," *European Urology*, Vol. 64, no. 6, pp. 876–892, 2013.

51. Cary, K. C., and M. R. Cooperberg, "Biomarkers in prostate cancer surveillance and screening: Past, present, and future," *Therapeutic Advances In Urology*, Vol. 5, no. 6, pp. 319–329, 2013.

52. Catalona, W. J., J. P. Richie, F. R. Ahmann, A. H. MâLiss, P. T. Scardino, R. C. Flanigan, J. B. Dekernion, T. L. Ratliff, L. R. Kavoussi, B. L. Dalkin, and W. B. Waters, "Comparison of digital rectal examination and serum prostate specific antigen in the early detection of prostate cancer: results of a multicenter clinical trial of 6,630 men," *The Journal of Urology*, Vol. 151, no. 5, pp. 1283–1290, 1994.

53. Izawa, J. I., L. Klotz, D. R. Siemens, W. Kassouf, A. So, J. Jordan, M. Chetner, and A. E. Iansavichene, "Prostate cancer screening: Canadian guidelines 2011," *Canadian Urological Association Journal*, Vol. 5, no. 4, p. 235, 2011.

54. Eifler, J. B., Z. Feng, B. M. Lin, M. T. Partin, E. B. Humphreys, M. Han, J. I. Epstein, P. C. Walsh, B. J. Trock, and A. W. Partin, "An updated prostate cancer staging nomogram (partin tables) based on cases from 2006 to 2011," *BJU International*, Vol. 111, no. 1, 2013.

55. Patel, U., and D. Rickards, *Handbook of Transrectal Ultrasound and Biopsy of The Prostate*, CRC Press, 2002.

56. Serefoglu, E. C., S. Altinova, N. S. Ugras, E. Akincioglu, E. Asil, and M. D. Balbay, "How reliable is 12-core prostate biopsy procedure in the detection of prostate cancer?," *Canadian Urological Association Journal*, Vol. 7, no. 5-6, p. E293, 2013.

57. Campbell, A., "Prostate template biopsy with callout box," 2016. Available at: https://www.flickr.com/photos/dundeetilt/26820791462.

58. Francesco, G., and C. M. Moore, "A critical comparison of techniques for mri-targeted biopsy of the prostate," *Translational Andrology and Urology*, Vol. 6, no. 3, p. 432, 2017.

59. Haffner, J., L. Lemaitre, P. Puech, G. P. Haber, X. Leroy, J. S. Jones, and A. Villers, "Role of magnetic resonance imaging before initial biopsy: Comparison of magnetic resonance imagingâtargeted and systematic biopsy for significant prostate cancer detection," *BJU International*, Vol. 108, no. 8b, pp. E171–E178, 2011.

60. Park, B. K., J. W. Park, S. Y. Park, C. K. Kim, H. M. Lee, S. S. Jeon, S. I. Seo, B. C. Jeong, and H. Y. Choi, "Prospective evaluation of 3-t mri performed before initial transrectal ultrasound-guided prostate biopsy in patients with high prostate-specific antigen and no previous biopsy," *American Journal of Roentgenology*, Vol. 197, no. 5, pp. W876–W881, 2011.

61. Pinto, P. A., P. H. Chung, A. R. Rastinehad, A. A. Baccala, J. Kruecker, C. J. Benjamin, S. Xu, P. Yan, S. Kadoury, C. Chua, and J. K. Locklin, "Magnetic resonance imaging/ultrasound fusion guided prostate biopsy improves cancer detection following transrectal ultrasound biopsy and correlates with multiparametric magnetic resonance imaging," *The Journal of Urology*, Vol. 186, no. 4, pp. 1281–1285, 2011.

62. Kongnyuy, M., A. K. George, A. R. Rastinehad, and P. A. Pinto, "Magnetic resonance imaging-ultrasound fusion-guided prostate biopsy: Review of technology, techniques, and outcomes," *Current Urology Reports*, Vol. 17, pp. 1–9, 2016.

63. Futterer, J. J., and J. O. Barentsz, "Mri-guided and robotic-assisted prostate biopsy," *Current Opinion in Urology*, Vol. 22, no. 4, pp. 316–319, 2012.

64. Das, C. J., A. Netaji, A. Razik, and S. Verma, "Mri-targeted prostate biopsy: What radiologists should know," *Korean Journal of Radiology*, Vol. 21, no. 9, p. 1087, 2020.

65. Myers, K., "A history of injection treatments-1 the syringe.," *Phlebology*, Vol. 34, no. 5, pp. 294–302, 2019.

66. Sette, P., R. M. Dorizzi, and A. M. Azzini, "Vascular access: An historical perspective from sir william harvey to the 1956 nobel prize to andre f. cournand, werner forssmann, and dickinson w. richards," *The Journal of Vascular Access*, Vol. 13, no. 2, pp. 137–144, 2012.

67. Abolhassani, N., P. Rajni, and M. Mehrdad, "Needle insertion into soft tissue: A survey," *Medical Engineering & Physics*, Vol. 29, no. 4, pp. 413–431, 2007.

68. DiMaio, S. P., and E. S. Septimiu, "Interactive simulation of needle insertion models," *IEEE Transactions on Biomedical Engineering*, Vol. 52, no. 7, pp. 1167–1179, 2005.

69. Trejos, A. L., J. Jayender, M. T. Perri, M. D. Naish, R. V. Patel, and R. A. Malthaner, "Robot-assisted tactile sensing for minimally invasive tumor localization," *The International Journal of Robotics Research*, Vol. 28, no. 9, pp. 1118–1133, 2009.

70. Wee, J., M. Kang, P. Francis, R. Brooks, L. Masotti, D. Villavicencio, and J. T. Gerstle, "Novel force-sensing system for minimally invasive surgical instruments," in *39th Annual International Conference of the IEEE EMBC*, (Shanghai–China), pp. 4447–4450, IEEE for Engineering in Medicine and Biology Society, 1-4 Sept 2017.

71. Liang, Q., K. Zou, J. Long, J. Jin, D. Zhang, G. Coppola, W. Sun, Y. Wang, and Y. Ge, "Multi-component fbg-based force sensing systems by comparison with other sensing technologies: A review," *IEEE Sensors Journal*, Vol. 18, no. 18, pp. 7345–7357, 2018.

72. Du, L., Z. Xiaoliang, and Z. Jiang, "An inductive sensor for real-time measurement of plantar normal and shear forces distribution," *IEEE Transactions on Biomedical Engineering*, Vol. 62, no. 5, pp. 1316–1323, 2014.

73. Damjanovic, D., "Materials for high temperature piezoelectric transducers," *Current Opinion in Solid State and Materials Science*, Vol. 3, no. 5, pp. 469–473, 1998.

74. Flannigan, C., C. D. Tan, and J. F. Scott., "Electrical studies of barkhausen switching noise in ferroelectric lead zirconate titanate (pzt) and batio3: Critical exponents and temperature-dependence," *Journal of Physics: Condensed Matter*, Vol. 32, no. 5, 2019.

75. Kalimuldina, G., N. Turdakyn, I. Abay, A. Medeubayev, A. Nurpeissova, D. Adair, and Z. Bakenov, "A review of piezoelectric pvdf film by electrospinning and its applications," *Sensors*, Vol. 20, no. 18, p. 5214, 2020.

76. Majid, M. J., and M. F. Yu, "Nanoscale characterization of isolated individual type i collagen fibrils: Polarization and piezoelectricity," *Nanotechnology*, Vol. 20, no. 8, 2009.

77. Gil, B., B. Li, A. Gao, and G. Z. Yang, "Miniaturized piezo force sensor for a medical catheter and implantable device," *ACS Applied Electronic Materials*, Vol. 2, no. 8, pp. 2669–2677, 2020.

78. Martin, K. H., B. D. Lindsey, J. Ma, M. Lee, S. Li, F. S. Foster, X. Jiang, and P. A. Dayton, "Dual-frequency piezoelectric transducers for contrast enhanced ultrasound imaging," *Sensors*, Vol. 14, no. 11, pp. 20825–20842, 2014.

79. Keil, S., "On the strain gage's 50th jubilee-a review of its evolution and of 33 years strain gage production at darmstadt," *Reports in Applied Measurement*, Vol. 4, no. 2, pp. 39–48, 1988.

80. Polygerinos, P., D. Zbyszewski, T. Schaeffter, R. Razavi, L. D. Seneviratne, and K. Althoefer, "Mri-compatible fiber-optic force sensors for catheterization procedures," *IEEE Sensors Journal*, Vol. 10, no. 10, pp. 1598–1608, 2010.

81. Lee, B. H., Y. H. Kim, K. S. Park, J. B. Eom, M. J. Kim, B. S. Rho, and H. Y. Choi, "Interferometric fiber optic sensors," *Sensors*, Vol. 12, no. 3, pp. 2467–2486, 2012.

82. Prerana, P., R. K. Varshney, B. P. Pal, and B. Nagaraju, "High sensitive fiber optic temperature sensor based on a side-polished single-mode fiber coupled to a tapered multimode overlay waveguide," *Journal of The Optical Society of Korea*, Vol. 14, no. 4, pp. 337–341, 2010.

83. Kim, D. W., F. Shen, X. Chen, and A. Wang, "Simultaneous measurement of refractive index and temperature based on a reflection-mode long-period grating and an intrinsic fabry-perot interferometer sensor," *Optics Letters*, Vol. 30, no. 22, pp. 3000–3002, 2005.

84. Beard, P. C., F. Perennes, E. Draguioti, and T. N. Mills, "Optical fiber photoacoustic-photothermal probe," *Optics Letters*, Vol. 23, no. 15, pp. 1235–1237, 1998.

85. Wang, X., J. Xu, Y. Zhu, K. L. Cooper, and A. Wang, "All-fused-silica miniature optical fiber tip pressure sensor," *Optics Letters*, Vol. 31, no. 7, pp. 885–887, 2006.

86. Su, H., I. I. Iordachita, J. Tokuda, N. Hata, X. Liu, R. Seifabadi, S. Xu, B. Wood, and G. S. Fischer, "Fiber-optic force sensors for mri-guided interventions and rehabilitation: A review," *IEEE Sensors Journal*, Vol. 17, no. 7, pp. 1952–1963, 2017.

87. Lefere, H. C., "Fundamentals of the interferometric fiber-optic gyroscope," *Optical Review*, Vol. 4, no. 1A, pp. 20–27, 1997.

88. Zhu, T., D. Wu, M. Liu, and D. W. Duan, "In-line fiber optic interferometric sensors in single-mode fibers," *Sensors*, Vol. 12, no. 8, pp. 10430–10449, 2012.

89. Tsai, W. H., and C. J. Lin, "A novel structure for the intrinsic fabry-perot fiber-optic temperature sensor," *Journal of Lightwave Technology*, Vol. 19, no. 5, pp. 682–686, 2001.

90. Kim, S. H., J. J. Lee, D. C. Lee, and I. B. Kwon, "A study on the development of transmission-type extrinsic fabry-perot interferometric optical fiber sensor," *Journal of Lightwave Technology*, Vol. 17, no. 10, pp. 1869–1874, 1999.

91. Bremer, K., E. Lewis, G. Leen, B. Moss, S. Lochmann, I. Mueller, T. Reinsch, and J. Schrotter, "Fibre optic pressure and temperature sensor for geothermal wells," *Sensors, 2010 IEEE*, 2010.

92. Liu, L., P. Lu, S. Wang, X. Fu, Y. Sun, D. Liu, J. Zhang, H. Xu, and Q. Yao, "Uv adhesive diaphragm-based fpi sensor for very-low-frequency acoustic sensing," *IEEE Photonics Journal*, Vol. 8, no. 1, pp. 1–9, 2015.

93. Choi, H. S., H. F. Taylor, and C. E. Lee, "High-performance fiber-optic temperature sensor using low-coherence interferometry," *Optics Letters*, Vol. 22, no. 23, pp. 1814–1816, 1997.

94. Lee, C. E., and H. F. Taylor, "Interferometric sensors using internal fiber mirrors," *Optical Fiber Sensors. Optica Publishing Group*, 1988.

95. Tseng, S. M., and C. L. Chen, "Optical fiber fabry-perot sensors," *Applied Optics*, Vol. 27, no. 3, pp. 547–551, 1988.

96. Lee, C. E., R. A. Atkins, and H. F. Taylor, "Performance of a fiber-optic temperature sensor from -200 to 1050 ^{0}C," *Optics Letters*, Vol. 13, no. 11, pp. 1038–1040, 1988.

97. Zhang, Y., J. Huang, X. Lan, L. Yuan, and H. Xiao, "Simultaneous measurement of temperature and pressure with cascaded extrinsic fabry-perot interferometer and intrinsic fabry-perot interferometer sensors," *Optical Engineering*, Vol. 53, no. 6, pp. 067101–067101, 2014.

98. Sahota, J. K., N. Gupta, and D. Dhawan, "Fiber bragg grating sensors for monitoring of physical parameters: A comprehensive review.," *Optical Engineering*, Vol. 59, no. 6, pp. 060901–060901, 2020.

99. Hill, K. O., Y. Fujii, D. C. Johnson, and B. S. Kawasaki, "Photosensitivity in optical fiber waveguides: Application to reflection filter fabrication," *Applied Physics Letters*, Vol. 32, no. 10, pp. 647–649, 1978.

100. Kersey, A. D., M. A. Davis, H. J. Patrick, M. LeBlanc, K. P. Koo, C. G. Askins, M. A. Putnam, and E. J. Friebele, "Fiber grating sensors," *Journal of Lightwave Technology*, Vol. 15, no. 8, pp. 1442–1463, 1997.

101. Presti, D. L., C. Massaroni, C. S. J. Leitao, M. D. F. Domingues, M. Sypabekova, D. Barrera, I. Floris, L. Massari, C. M. Oddo, S. Sales, and I. I. Iordachita, "Fiber bragg gratings for medical applications and future challenges: A review," *IEEE Access*, Vol. 8, pp. 156863–156888, 2020.

102. Mohanty, L., and S. C. Tjin, "Pressure mapping at orthopaedic joint interfaces with fiber bragg gratings," *Applied Physics Letters*, Vol. 88, no. 8, p. 083901, 2006.

103. Koyama, S., H. Ishizawa, K. Fujimoto, S. Chino, and Y. Kobayashi, "Influence of individual differences on the calculation method for fbg-type blood pressure sensors," *Sensors*, Vol. 17, no. 1, p. 48, 2016.

104. Yu, Q., Y. Zhang, Y. Dong, Y. P. Li, C. Wang, and H. Chen, "Study on optical fiber bragg grating temperature sensors for human body temperature monitoring," in *2012 Symposium on Photonics and Optoelectronics*, pp. 1–4, IEEE, May 2012.

105. Lunwei, Z., Q. Jinwu, S. Linyong, and Z. Yanan, "Fbg sensor devices for spatial shape detection of intelligent colonoscope," in *IEEE International Conference on Robotics and Automation*, Vol. 1, pp. 834–840, IEEE, April 2004.

106. Zhang, T., B. Chen, and S. Zuo, "A novel 3-dof force sensing microneedle with integrated fiber bragg grating for microsurgery," *IEEE Transactions on Industrial Electronics*, Vol. 69, no. 1, pp. 940–949, 2021.

107. Settecase, F., A. J. Martin, P. Lillaney, A. Losey, and S. W. Hetts, "Magnetic resonance-guided passive catheter tracking for endovascular therapy," *Magnetic Resonance Imaging Clinics*, Vol. 23, no. 4, pp. 591–605, 2015.

108. Manke, C., W. R. Nitz, B. Djavidani, M. Strotzer, M. Lenhart, M. Volk, S. Feuerbach, and J. Link, "Mr imaging-guided stent placement in iliac arterial stenoses: A feasibility study," *Radiology*, Vol. 219, no. 2, pp. 527–534, 2001.

109. Basar, B., M. Sonmez, D. K. Yildirim, R. Paul, D. A. Herzka, O. Kocaturk, R. J. Lederman, and A. E. Campbell-Washburn, "Susceptibility artifacts from metallic markers and cardiac catheterization devices on a high-performance 0.55 T mri system," *Magnetic Resonance Imaging*, Vol. 77, pp. 14–20, 2021.

110. Omary, R. A., O. Unal, D. S. Koscielski, R. Frayne, F. R. Korosec, C. A. Mistretta, C. M. Strother, and T. M. Grist, "Real-time mr imaging-guided passive catheter tracking with use of gadolinium-filled catheters," *Journal of Vascular and Interventional Radiology*, Vol. 11, no. 8, pp. 1079–1085, 2000.

111. Yildirim, D. K., C. Bruce, D. Uzun, T. Rogers, K. O'Brien, R. Ramasawmy, A. E. Campbell-Washburn, D. A. Herzka, R. J. Lederman, and O. Kocaturk, "A 20-gauge active needle design with thin-film printed circuitry for interventional mri at 0.55 T," *Magnetic Resonance in Medicine*, Vol. 86, no. 3, pp. 1786–1801, 2021.

112. Yildirim, D. K., D. Uzun, C. G. Bruce, J. M. Khan, T. Rogers, W. H. Schenke, R. Ramasawmy, A. E. Campbell-Washburn, D. A. Herzka, R. J. Lederman, and O. Kocaturk, "An interventional mri guidewire combining profile and tip conspicuity for catheterization at 0.55 T," *Magnetic Resonance in Medicine*, Vol. 89, no. 2, pp. 845–858, 2023.

113. Burl, M., G. A. Coutts, and I. R. Young, "Tuned fiducial markers to identify body locations with minimal perturbation of tissue magnetization," *Magnetic Resonance in Medicine*, Vol. 36, no. 3, pp. 491–493, 1996.

114. Quick, H. H., M. O. Zenge, H. Kuehl, G. Kaiser, S. Aker, S. Massing, S. Bosk, and M. E. Ladd, "Interventional magnetic resonance angiography with no strings attached: Wireless active catheter visualization," *Magnetic Resonance in Medicine*, Vol. 53, no. 2, pp. 446–455, 2005.

115. Kaiser, M., M. Detert, M. A. Rube, A. El-Tahir, O. J. Elle, A. Melzer, B. Schmidt, and G. H. Rose, "Resonant marker design and fabrication techniques for device visualization during interventional magnetic resonance imaging," *Biomedical Engineering/Biomedizinische Technik*, Vol. 60, no. 2, pp. 89–103, 2015.

116. Quick, H. H., H. Kuehl, G. Kaiser, S. Bosk, J. F. Debatin, and M. E. Ladd, "Inductively coupled stent antennas in mri," *Magnetic Resonance in Medicine*, Vol. 48, no. 5, pp. 781–790, 2002.

117. Glowinski, A., G. Adam, A. Bucker, J. Neuerburg, J. J. V. Vaals, and R. W. Gunther, "Catheter visualization using locally induced, actively controlled field inhomogeneities," *Magnetic Resonance in Medicine*, Vol. 38, no. 2, pp. 253–258, 1997.

118. Eibofner, F., H. Wojtczyk, H. Graf, and S. Clasen, "Magnetic resonance visualization of conductive structures by sequence-triggered direct currents and spin-echo phase imaging," *Medical Physics*, Vol. 41, no. 6 part 1, p. 062301, 2014.

119. Eibofner, F., P. Martirosian, C. Wurslin, H. Graf, R. Syha, and S. Clasen, "Mr-visualization of interventional devices using transient field alterations and balanced steady-state free precession imaging," *Medical Physics*, Vol. 42, no. 11, pp. 6558–6563, 2015.

120. Carr, H. Y., "Steady-state free precession in nuclear magnetic resonance," *Physical Review*, Vol. 112, no. 5, p. 1693, 1958.

121. Hennig, J., H. G. Friedburg, and A. Frankenschmidt, "Rapid acquisition with relaxation enhancement mr urography: A fast non-tomographic imaging procedure for demonstrating the efferent urinary pathways using nuclear magnetic resonance," *Der Radiologe*, Vol. 27, no. 1, pp. 45–7, 1987.

122. *ASTM F2052-15 Standard Test Method For Measurement of Magnetically Induced Displacement Force on Medical Devices in The Magnetic Resonance Environment*, 2017. www.astm.org.

123. *ASTM F2182-19e2 Standard Test Method for Measurement of Radio Frequency Induced Heating on or Near Passive Implants During Magnetic Resonance Imaging*, 2019. www.astm.org.

124. *ASTM F2213-17 Standard Test Method for Measurement of Magnetically Induced Torque on Medical Devices in the Magnetic Resonance Environment*, 2017. www.astm.org.

125. Kim, U., D. H. Lee, W. J. Yoon, B. Hannaford, and H. R. Choi, "Force sensor integrated surgical forceps for minimally invasive robotic surgery," *IEEE Transactions on Robotics*, Vol. 31, no. 5, pp. 1214–1224, 2015.

126. Li, L., B. Yu, C. Yang, P. Vagdargi, R. A. Srivatsan, and H. Choset, "Development of an inexpensive tri-axial force sensor for minimally invasive surgery," in *IEEE/RSJ International Conference on Intelligent Robots and Systems (IROS)*, pp. 906–913, IEEE, September 2017.

127. Noebauer-Huhmann, I. M., M. A. Weber, R. K. Lalam, S. Trattnig, K. Bohndorf, F. Vanhoenacker, A. Tagliafico, C. van Rijswijk, J. C. Vilanova, P. D. Afonso, and M. Breitenseher, "Soft tissue tumors in adults: Essr-approved guidelines for diagnostic imaging," in *Seminars in Musculoskeletal Radiology*, Vol. 19 of *05*, pp. 475–482, Thieme Medical Publishers, December 2015.

128. Rothke, M., A. G. Anastasiadis, M. Lichy, M. Werner, P. Wagner, S. Kruck, C. D. Claussen, A. Stenzl, H. P. Schlemmer, and D. Schilling, "Mri-guided prostate biopsy detects clinically significant cancer: Analysis of a cohort of 100 patients after previous negative trus biopsy," *World Journal of Urology*, Vol. 30, pp. 213–218, 2012.

129. Lindenberg, L., M. Ahlman, B. Turkbey, E. Mena, and P. Choyke, "Evaluation of prostate cancer with pet/mri," *Journal of Nuclear Medicine*, Vol. 57, no. Suplement 3, pp. 111S–116S, 2016.

130. Beekmans, S., T. Lembrechts, J. V. den Dobbelsteen, and D. V. Gerwen, "Fiber-optic fabry-perot interferometers for axial force sensing on the tip of a needle," *Sensors*, Vol. 17, no. 1, p. 38, 2016.

131. Wee, J., M. Kang, P. Francis, R. Brooks, L. M. D. Villavicencio, T. Looi, G. Azzie, J. Drake, and J. T. Gerstle, "Novel force-sensing system for minimally invasive surgical instruments," in *39th Annual International Conference of the IEEE Engineering in Medicine and Biology Society (EMBC)*, pp. 4447–4450, IEEE, July 2017.

132. Woodrum, D. A., K. R. Gorny, B. Greenwood, and L. A. Mynderse, "Mri-guided prostate biopsy of native and recurrent prostate cancer," in *Seminars in Interventional Radiology*, Vol. 33 of *03*, pp. 196–205, Thieme Medical Publishers, September 2016.

133. Born, M., and E. Wolf, *Principles of Optics*, Oxford: Pergamon Press, 1964.

134. Ulgen, N. O., D. Uzun, and O. Kocaturk, "Phantom study of a fiber optic force sensor design for biopsy needles under mri," *Biomedical Optics Express*, Vol. 10, no. 1, pp. 242–251, 2019.

135. Evans, A., P. Whelehan, K. Thomson, K. Brauer, L. Jordan, C. Purdie, D. McLean, L. Baker, S. Vinnicombe, and A. Thompson, "Differentiating benign from malignant solid breast masses: Value of shear wave elastography according to lesion stiffness combined with greyscale ultrasound according to bi-rads classification," *British Journal of Cancer*, Vol. 107, no. 2, pp. 224–229, 2012.

136. Bayat, M., M. Denis, A. Gregory, M. Mehrmohammadi, V. Kumar, D. Meixner, R. T. Fazzio, M. Fatemi, and A. Alizad, "Diagnostic features of quantitative comb-push shear elastography for breast lesion differentiation," *PloS One*, Vol. 12, no. 3, p. e0172801, 2017.

137. Athanasiou, A., A. Tardivon, M. Tanter, B. Sigal-Zafrani, J. Bercoff, T. Deffieux, J. L. Gennisson, M. Fink, and S. Neuenschwander, "Breast lesions: Quantitative elastography with supersonic shear imaging-preliminary results," *Radiology*, Vol. 256, no. 1, pp. 297–303, 2010.

138. Krouskop, T. A., T. M. Wheeler, F. Kallel, B. S. Garra, and T. Hall, "Elastic moduli of breast and prostate tissues under compression," *Ultrasonic Imaging*, Vol. 20, no. 4, pp. 260–274, 1998.

139. Barr, R. G., R. Memo, and C. R. Schaub, "Shear wave ultrasound elastography of the prostate: Initial results," *Ultrasound Quarterly*, Vol. 28, no. 1, pp. 13–20, 2012.

140. Ahmad, S., R. Cao, T. Varghese, L. Bidaut, and G. Nabi, "Transrectal quantitative shear wave elastography in the detection and characterisation of prostate cancer," *Surgical Endoscopy*, Vol. 27, pp. 3280–3287, 2013.

141. Shyamala, K., H. C. Girish, and S. Murgod, "Risk of tumor cell seeding through biopsy and aspiration cytology," *Journal of International Society of Preventive & Community Dentistry*, Vol. 4, no. 1, p. 5, 2014.

142. Hansen, N. M., X. Ye, B. J. Grube, and A. E. Giuliano, "Manipulation of the primary breast tumor and the incidence of sentinel node metastases from invasive breast cancer," *Archives of Surgery*, Vol. 139, no. 6, pp. 634–640, 2004.

143. Weiss, C. R., S. G. Nour, and J. S. Lewin, "Mr-guided biopsy: A review of current techniques and applications," *Journal of Magnetic Resonance Imaging: An Official Journal of the International Society for Magnetic Resonance in Medicine*, Vol. 27, no. 2, pp. 311–325, 2008.

144. Pondman, K. M., J. J. Futterer, B. ten Haken, J. L. S. Kool, J. A. Witjes, T. Hambrock, K. J. Macura, and J. O. Barentsz, "Mr-guided biopsy of the prostate: An overview of techniques and a systematic review," *European Urology*, Vol. 54, no. 3, pp. 517–527, 2008.

145. Ricke, J., M. Thormann, M. Ludewig, K. Jungnickel, O. Grosser, C. Wybranski, N. Peters, P. Hass, J. Bunke, and F. Fischbach, "Mr-guided liver tumor ablation employing open high-field 1.0 T mri for image-guided brachytherapy," *European Radiology*, Vol. 20, pp. 1985–1993, 2010.

146. Lederman, R. J., M. A. Guttman, D. C. Peters, R. B. Thompson, J. M. Sorger, A. J. Dick, V. K. Raman, and E. R. McVeigh, "Catheter-based endomyocardial injection with real-time magnetic resonance imaging," *Circulation*, Vol. 105, no. 11, pp. 1282–1284, 2002.

147. Ratnayaka, K., A. Z. Faranesh, M. S. Hansen, A. M. Stine, M. Halabi, I. M. Barbash, W. H. Schenke, V. J. Wright, L. P. Grant, P. Kellman, and O. Kocaturk, "Real-time mri-guided right heart catheterization in adults using passive catheters," *European Heart Journal*, Vol. 34, no. 5, pp. 380–389, 2013.

148. Raval, A. N., J. D. Telep, M. A. Guttman, C. Ozturk, M. Jones, R. B. Thompson, V. J. Wright, W. H. Schenke, R. DeSilva, R. J. Aviles, and V. K. Raman, "Real-time magnetic resonance imaging-guided stenting of aortic coarctation with commercially available catheter devices in swine," *Circulation*, Vol. 112, no. 5, pp. 699–706, 2005.

149. Yeung, C. J., R. C. Susil, and E. Atalar, "Rf safety of wires in interventional mri: Using a safety index," *Magnetic Resonance in Medicine: An Official Journal of the International Society for Magnetic Resonance in Medicine*, Vol. 47, no. 1, pp. 187–193, 2002.

150. Kettenbach, J., D. F. Kacher, A. R. Kanan, B. Rostenberg, J. Fairhurst, A. Stadler, K. Kienreich, and F. A. Jolesz, "Intraoperative and interventional mri: Recommendations for a safe environment," *Minimally Invasive Therapy Allied Technologies*, Vol. 15, no. 2, pp. 53–64, 2006.

151. Shellock, F. G., "Metallic surgical instruments for interventional mri procedures: Evaluation of mr safety," *Journal of Magnetic Resonance Imaging*, Vol. 13, no. 1, pp. 152–157, 2001.

152. Atalar, E., "Radiofrequency safety for interventional mri procedures1," *Academic Radiology*, Vol. 12, no. 9, pp. 1149–1157, 2005.

153. Kaiser, M., K. Johannes, and G. Rose., "Interventional mri: Minimal-invasive surgery under mr guidance," in *2011 IEEE MTT-S International Microwave Symposium*, 2011.

154. Thompson, S. M., K. R. Gorny, E. M. K. Koepsel, B. T. Welch, L. Mynderse, A. Lu, C. P. Favazza, J. P. Felmlee, and D. A. Woodrum, "Body interventional mri for diagnostic and interventional radiologists: Current practice and future prospects," *Radiographics*, Vol. 41, no. 6, pp. 1785–1801, 2021.

155. Blanco, R. T., R. Ojala, J. Kariniemi, J. Perala, J. Niinimaki, and O. Tervonen, "Interventional and intraoperative mri at low field scanner - a review," *European Journal of Radiology*, Vol. 56, no. 2, pp. 130–142, 2005.

156. Campbell-Washburn, A. E., R. Ramasawmy, M. C. Restivo, I. Bhattacharya, B. Basar, D. A. Herzka, M. S. Hansen, T. Rogers, W. P. Bandettini, D. R. McGuirt, and C. Mancini, "Opportunities in interventional and diagnostic imaging by using high-performance low-field-strength mri," *Radiology*, Vol. 293, no. 2, pp. 384–393, 2019.

157. Arnold, T. C., C. W. Freeman, B. Litt, and J. M. Stein, "Low-field mri: Clinical promise and challenges," *Journal of Magnetic Resonance Imaging*, Vol. 57, no. 1, pp. 25–44, 2023.

158. Wang, W., "Magnetic resonance-guided active catheter tracking," *Magnetic Resonance Imaging Clinics*, Vol. 23, no. 4, pp. 579–589, 2015.

159. Saikus, C. E., K. Ratnayaka, I. M. Barbash, J. H. Colyer, O. Kocaturk, A. Z. Faranesh, and R. J. Lederman, "Mri-guided vascular access with an active visualization needle," *Journal of Magnetic Resonance Imaging*, Vol. 34, no. 5, pp. 1159–1166, 2011.

160. Baysoy, E., D. K. Yildirim, C. Ozsoy, S. Mutlu, and O. Kocaturk, "Thin film based semi-active resonant marker design for low profile interventional cardiovascular mri devices," *Magnetic Resonance Materials in Physics, Biology and Medicine*, Vol. 30, pp. 93–101, 2017.

161. Yutzy, S. R., and J. L. Duerk, "Pulse sequences and system interfaces for interventional and real-time mri," *Journal of Magnetic Resonance Imaging: An Official Journal of the International Society for Magnetic Resonance in Medicine*, Vol. 27, no. 2, pp. 262–275, 2008.

162. Duerk, J. L., K. Butts, K. P. Hwang, and J. S. Lewin, "Pulse sequences for interventional magnetic resonance imaging," *Topics in Magnetic Resonance Imaging*, Vol. 11, no. 3, pp. 147–162, 2000.

163. Henk, C. B., C. B. Higgins, and M. Saeed, "Endovascular interventional mri," *Journal of Magnetic Resonance Imaging: An Official Journal of the International Society for Magnetic Resonance in Medicine*, Vol. 22, no. 4, pp. 451–460, 2005.

164. Cleary, K., and T. M. Peters, "Image-guided interventions: technology review and clinical applications," *Annual Review of Biomedical Engineering*, Vol. 12, pp. 119–142, 2010.